

**MATERIALS AND METHODS FOR NANOLITHOGRAPHY USING
SCANNING THERMAL CANTILEVER PROBES**

A Dissertation
Presented to
The Academic Faculty

by

Yueming Hua

In Partial Fulfillment
of the Requirements for the Degree
of Doctor of Philosophy in the
School of Chemical & Biomolecular Engineering

Georgia Institute of Technology
May 2008

Copyright 2008 by Yueming Hua

**MATERIALS AND METHODS FOR NANOLITHOGRAPHY USING
SCANNING THERMAL CANTILEVER PROBES**

Approved by:

Dr. Clifford L. Henderson, Advisor
School of Chemical & Biomolecular
Engineering
Georgia Institute of Technology

Dr. William P. King
School of Mechanical Science and
Engineering
*University of Illinois at Urbana-
Champaign*

Dr. Laren M. Tolbert
School of Chemistry & Biochemistry
Georgia Institute of Technology

Dr. Dennis W. Hess
School of Chemical & Biomolecular
Engineering
Georgia Institute of Technology

Dr. Hang Lu
School of Chemical & Biomolecular
Engineering
Georgia Institute of Technology

Date Approved: 3/10/2008

ACKNOWLEDGEMENTS

First, I would like to thank my advisor, Dr. Clifford Henderson. Thanks him for taking me as his student, giving me the opportunity to work on this interesting project, and making my PhD study in Georgia Tech such a rich and wonderful experience. Thanks for his encouragement when I was frustrated and his inspiration when I was confused. Thanks for his understanding of the difficulties I was going through and his willingness to help me out when I was in trouble.

I would like to thank Dr. William King at University of Illinois at Urbana-Champaign. Thanks for his generous help on my thesis research. Dr. King's advising and suggestions on the project are always very helpful. Thanks him for giving us those wonderful and powerful thermal cantilevers. Without these thermal cantilevers, most of the results in this work can't be completed. I also want to thank Dr. Dennis Hess, Dr. Laren Tolbert and Dr. Hang Lu for serving on my committee and providing valuable suggestions during this work.

I can't forget the help from Dr. Kazuhiro Yamanaka. He introduced me into organic synthesis. Many thanks to Ashwini Sinha for his encouragement and help on my research, Cheng-Tsung Lee for his help on cleanroom works and many useful discussions with me, and Michael Romeo for training me on some of the equipments in our group. Thanks Jungchul Lee and Shubham Saxena for their help on cantilever calibrations and some of the thermal writing, Ingu Song and Shantanu Pathak for their help on XPS analysis. I also want to thank Hua-Wei Chu, Richard Lawson, Annapoorani Sundaramoorthi, Jassem Abdallah in Dr. Henderson's group for all the help they provided.

Finally, special thanks to my wife for being with me here in US, bring me happiness, and going through hard times with me. And my parents, they are always supporting me from the other side of the earth.

TABLE OF CONTENTS

	Page
ACKNOWLEDGEMENTS	iii
LIST OF TABLES	viii
LIST OF FIGURES	ix
SUMMARY	xiii
<u>CHAPTER</u>	
1. INTRODUCTION	1
1.1 Nanopatterning Methods	1
1.2 Scanning Probe Lithography Methods	4
1.3 Thermal AFM Probes	8
1.4 Organization of Thesis	10
1.5 References	12
2. INSTRUMENTS	16
2.1 AFM Systems	16
2.2 Thermal Cantilever Characterization	18
2.3 Thermal Writing AFM	26
2.4 Thermal Writing Operation	31
2.5 References	35
3. THERMAL WRITING ON POLYMERS USING DECOMPOSITION	38
3.1 Introduction and Background of Sacrificial Polymers	38
3.2 Material Synthesis and Characterization	40
3.3 Thermal Writing Experiments and Results: PPC, PC-V, CPC-IV	48
3.4 Effect of Crosslinking	58

3.5 References	69
4. 3D THERMAL WRITING	72
4.1 Introduction and Background of 3D Lithography	72
4.2 Experimental	73
4.3 Results and Discussion	74
4.4 Conclusion	83
4.5 References	83
5. SELECTIVE ALD	85
5.1 Introduction and Background	85
5.2 Experimental	86
5.3 Results and Discussion	87
5.4 Conclusions	96
5.5 References	96
6. THERMAL PROBE SURFACE MODIFICATION AND IMAGING	98
6.1 Introduction and Background	98
6.2 Material Synthesis and Characterization	100
6.3 ALD Top Surface Imaging of ThAFM Pattern	113
6.4 Conclusions	121
6.5 References	121
7. THERMAL WRITING IN SELF ASSEMBLY MONOLAYERS	123
7.1 Introduction and Background	123
7.2 Patterning APTES SAMs	1254
7.3 Thermal Writing on MP TES SAMs	127
7.4 Conclusions	140
7.5 References	141

8. SIMULATION AND MODELING	143
8.1 Introduction	143
8.2 Simulation of Cantilever Heating	144
8.3 Heat Transport and Reaction Kinetics in Thermal Decomposition	147
8.4 Modeling of Thermal Writing Process and Experimental Data Fitting	154
8.5 Conclusions	162
8.6 References	162
9. SUMMERY AND RECOMMENDATIONS FOR SUTURE WORKS	164
9.1 Summery	164
9.2 Recommendations for Future Works	166
9.3 References	171
APPENDIX A: AFM TOPOGRAPHY DATA ANALYSIS	172
APPENDIX B: TGA DATA ANALYSIS	174
APPENDIX C: TGA SIMULATION WITH SINGLE STEP DECOMPOSITION	179
APPENDIX D: TGA SIMULATION WITH TWO-STEP DECOMPOSITION	182

LIST OF TABLES

		Page
Table 1-1	Comparison of AFM lithography with other lithography methods	8
Table 6-1	Contact angle measurements	111
Table 6-2	Calculated atomic concentration from XPS spectrum	115
Table 7-1	Atomic concentration of different SAMs	136

LIST OF FIGURES

		Page
Figure 2-1	Different AFM modes	16
Figure 2-2	SEM image of a thermal cantilever	19
Figure 2-3	SEM images of thermal cantilever tip	20
Figure 2-4	Resistance vs. heating power of a typical thermal cantilever	22
Figure 2-5	Cantilever heater temperature vs. heating power of a typical thermal cantilever	23
Figure 2-6	Cantilever resistance vs. cantilever heater temperature	23
Figure 2-7	Measurement of spring constant of a thermal cantilever	25
Figure 2-8	Force-distance of curves of a thermal cantilever	26
Figure 2-9	Special designed cantilever holder for thermal cantilever	27
Figure 2-10	Diagram of heating circuit for thermal cantilever	28
Figure 2-11	Interface of the LabView controlling software	30
Figure 2-12	An optical microscope image of a sample substrate for AFM thermal writing experiment	32
Figure 2-13	AFM topography image of a Benzene structure thermally written in a PMMA film with PicoLith software	34
Figure 3-1	Synthetic route used to prepare cross-linkable co-polycarbonates	42
Figure 3-2	¹ H-NMR of copolycarbonate oligomer (CDCl ₃)	44
Figure 3-3	DSC curves of copolycarbonate oligomers, (N ₂ , 10 °C/min)	46
Figure 3-4	TGA data for uncured and cured end-capped co-polycarbonate oligomers	47
Figure 3-5	Process for using thermally sacrificial polymers for direct nanoscale thermal patterning using the AFM probe tip	48
Figure 3-7	Example of AFM images of poly(propylene carbonate) film patterned using a heated AFM tip.	50

Figure 3-7	Example of copolycarbonates that have been used as thermally sacrificial polymers in this work	52
Figure 3-8	AFM topographic scan of surface of Polymer V	52
Figure 3-9	A thermal written square in cross-linked PC-IV polymer thin film	55
Figure 3-10	Thermal written lines in cross-linked PC-IV polymer thin film	56
Figure 3-11	Synthetic route for make cross-linkable PHOST co-polymer	59
Figure 3-12	¹ H-NMR spectra of PHOST based polymer or co-polymers	60
Figure 3-13	AFM topography image (with lighting) of thermally written dot patterns in a PHOST co-polymers	62
Figure 3-14	Dot depth versus heating time for PHOST co-polymers containing different AOC: EOC monomer ratios	63
Figure 3-15	Ratio of indent volume to pile up volume (V_i/V_p) versus indent total volume (V_i) for the PHOST based co-polymers	64
Figure 3-16	Dot thermally written in crosslined PHOST co-polymer	67
Figure 3-17	5 micron squares patterned into the three AOC content PHOST-based polymers	68
Figure 4-1	Cartoon of 3D nano-sculpting using heated probe tip	73
Figure 4-2	Thermal written 10 μm lines at 663 °C with different scan speeds	75
Figure 4-3	Line depth vs. heating time of single line scan	78
Figure 4-4	AFM topography image of thermally patterned 3D feature in CPC-4	79
Figure 4-5	Cross section profiles of the 3D feature	80
Figure 4-6	AFM 3D images of 3D structures made by multiple scans	82
Figure 5-1	A thermal written square before and after a 130 sec O ₂ plasma descum	89
Figure 5-2	Selective ALD TiO ₂ pattern in thermal written area	92
Figure 6-1	Resolution limitation of thermal decomposition method	98
Figure 6-2	Cartoon shows thermal probe surface modification and imaging	99
Figure 6-3	Molecular structures of four different protected PHOST polymers and their TGA data	101

Figure 6-4	Iso-TGA of iPOC-PHOST	103
Figure 6-5	Isothermal TGA of AOC-PHOST	103
Figure 6-6	Illustration of syn-elimination	104
Figure 6-7	Pyrolysis of propylene	105
Figure 6-8	¹ HNMR of partial protected AOC-PHOST	105
Figure 6-9	Synthetic route of iPOC-AOC-PHOST copolymer and its ¹ HNMR spectrum	106
Figure 6-10	TGA trace of iPOC-AOC-PHOST copolymer	108
Figure 6-11	FT-IR of cured iPOC-AOC-PHOST copolymer under different conditions	110
Figure 6-12	Equipment setup for gas-phase HMDS silylation	111
Figure 6-13	FT-IR of PHOST before and after HMDS silylation	112
Figure 6-14	Contact angle measurement of PHOST under different conditions	113
Figure 6-15	XPS spectrums of iPOC-AOC-PHOST samples after ALD deposition of TiO ₂	114
Figure 6-16	AFM topography and phase image of a line pattern after ALD deposition of TiO ₂	117
Figure 6-17	Cross section profile before and after plasma etching	118
Figure 6-18	AFM topography and phase images on ALD sample	120
Figure 7-1	Thermal writing on APTES/Acetic acid SAM	124
Figure 7-2	AFM images of thermal written APTES/Acetic acid	126
Figure 7-3	Cartoon of thermal writing on THP-MPTES SAMs and deposition gold nano-particles	128
Figure 7-4	Synthetic route for make THP-MPTES	128
Figure 7-5	¹ H-NMR of synthesized PPTS	129
Figure 7-6	¹ H-NMR of the reaction mixture at different time	130
Figure 7-7	Deprotection of THP protected thiol compound	132

Figure 7-8	Reduction of disulfide compound by DTT	133
Figure 7-9	Contact angle measurements of THP-MPTES SAMs	134
Figure 7-10	XPS analysis of MPTES SAMs	136
Figure 7-11	AFM phase images of THP-MPTES SAMs after deposition of AuNPs	137
Figure 7-12	Deposited AuNPs on thermal written area of THP-MPTES SAMs	138
Figure 8-1	FemLab model for a thermal cantilever	145
Figure 8-2	FemLab model for a thermal cantilever in a room environment	145
Figure 8-3	Cantilever heat dissipation at different heater temperatures	146
Figure 8-4	Heat transport in AFM thermal writing	149
Figure 8-5	Temperature profile along the cantilever central axis	149
Figure 8-6	Experimental TGA data fitting to extract the kinetics parameters of thermal decomposition of PC-4 polymer	151
Figure 8-7	Experimental and simulated TGA curves for PC-4 polymer	152
Figure 8-8	A heated cantilever tip in contact with polymer material	154
Figure 8-9	Heater temperature vs. line depth for constant heating power	156
Figure 8-10	Sensitivity analysis of heating temperature and thermal conductivity of polymer	158
Figure 8-11	Tip temperature vs. line depth for different sample film thicknesses	159
Figure 8-12	Thickness of heated region versus tip temperature	160
Figure 8-13	Experimental results and modeling results for thermal writing lines	161
Figure 9-1	Synthetic routes for cyclic carbonate	167
Figure 9-2	Thermal writing in SAMs for selective ALD deposition	169
Figure 9-3	Thermal writing in PPV polymer	170

SUMMARY

This work presents the novel applications of heated AFM tip in nanolithography. Different strategies were investigated for patterning materials using heated AFM tip. New materials were developed specifically for these new nanolithography methods. Some simulation and modeling work was done to further understand the heat transfer and chemical reactions involved in the thermal writing process.

The selective thermal decomposition of polymer was the first thermal patterning method using heated AFM tip we've investigated. A couple of different sacrificial polymers were used as the writing materials. Among these materials, the cross-linked amorphous polycarbonate (CPC-IV) was the best material for this application. Cross-linking can improve the resistance to thermal flow during thermal writing, which is the most critical issue for this application. Also amorphous is very important for obtaining a uniform polymer thin film with smooth surface. The effect of cross-linking density on material performance was investigated. High cross-linking density is good for getting high resolution. But the material with high cross-linking density needs more energy to be decomposed, and this can slow down the writing speed. Another important advantage of cross-linked polymer versus linear polymer is that the decomposition depth of cross-linked polymer is much easy to be controlled. Base on this property, we've developed a novel 3D thermal writing technology using cross-linked polymer as the writing material. We've also developed a combined method that can utilize the heated cantilever probe to pattern a polymer masking layer that can serve as a template for area selective atomic layer deposition techniques. As a demonstration, TiO_2 was deposited on silicon surface

using thermal probe nanolithography patterned polymer as the masking layer. Detailed process conditions were investigated.

The resolution of selective decomposition method is limited by the film thickness. In order to overcome this limitation, we've also developed another thermal probe nanolithography method, which is thermal probe top surface imaging. In this method, the heated AFM tip was used to generate functional groups on the polymer surface, and ALD was used to selectively deposit TiO_2 on the surface where contains those functional groups. A new poly (hydroxyl styrene) based copolymer was developed for this method. By choosing the proper protecting group, this material has the right thermal stability for both the thermal writing and the ALD process. We've successfully demonstrated this technology. In this process, we noticed the tip can be contaminated, and the tip performance can degrade over time. So we presented a tip cleaning process to solve this problem.

We've also investigated using self assembly monolayers (SAMs) as the thermal writing material. SAMs are the ideal materials for thermal writing, because less material is used, and there is no deformation problem of the substrate. These two are the major advantages of thermal writing on SAMs. We investigated two different SAMs as the writing materials. One is the aminopropyltriethoxysilane (APTES) and the other one is tetrahydropyranyl (THP) protected 3-mercaptopropyltriethoxysilane (MPTES). We demonstrated that the APTES can be patterned using thermal AFM probe, and other materials can be selectively deposited on the patterned APTES SAMs. But our main focus of patterning SAMs is on THP-MPTES. We proposed to use thermal AFM probe to selectively generate thiol groups from THP-MPTES SAMs, and then use these thiol

groups to guide the deposition AuNPs. Detailed analysis was done to prove the chemistry behind this method. AuNPs were successfully deposited on pattern THP-MPTES SAMs.

We've developed a couple of nanolithography method using thermal AFM probes. Some simulation and modeling works were also done to help us further understand these processes. FemLab was used to analyze the heat transfer in the thermal cantilever and the between the heated tip and substrate. The simulated results have very good agreement with experimental data. We've also simulated the TGA curve with ultra high heating rate to understand the thermal decomposition using heated AFM tip. Base on kinetics of polymer thermal decomposition, we've built a simple model for the selective thermal decomposition nanolithography. And the experimental results can be very well fitted by this model.

CHAPTER 1

INTRODUCTION

1.1 Nanopatterning Methods: E-Beam Lithography, Photo Lithography, and Nanoimprinting

Demands for high performance, speed, and minimal device size in the area of electronics, and more recently even mechanical devices, has resulted in a need to develop tools and processes for fabricating structures at ever decreasing length scales. Currently, cutting edge microelectronic devices already incorporate structures that are patterned at length scales on the order of 100 nm while microelectromechanical devices (MEMS) are slightly behind but quickly pushing into that arena as well. Historically, the most critical technology for device microfabrication has been the tools and materials used to produce the patterned material structures which build up each functional device.[1] As device dimensions continue to shrink into the sub-100nm range, development of methods for producing patterned structures at these length scales represents a major technical and economic challenge to all of the industries that rely on such microfabrication technology.

The vast majority of current nanofabrication research is focused on one of three patterning technologies: optical lithography, electron beam lithography, or imprinting.

1.1.1 Photolithography

Optical lithography [2], which utilizes pattern-wise exposure of polymer photoresist films to ultraviolet radiation to produce patterned polymer relief structures, is still the most widely used technology in industry for fabricating microelectronic and MEMS devices. However, as device dimensions continue to shrink below 100 nm in

size, optical lithography is becoming increasingly more difficult and expensive. The next generation of immersion 193 nm optical exposure tools are likely to cost on the order of \$25M per tool. These costs limit the use of such technologies to production of only the highest volume devices such as memory chips and computer processors. Even at these extreme costs, the ultimate resolution of optical lithography systems is most likely limited to approximately 50 nm due to optical and material limitations.[3,4] Complimentary metal oxide semiconductor (CMOS) devices are expected to scale to at least devices containing feature sizes on the order of 25 nm, and post-CMOS technologies such as quantum computing devices will require even smaller features. Therefore, there is a long term need for patterning technologies which can surpass the limited feature size capabilities of optical lithography tools. Furthermore, even before this 50 nm size limit is reached, optical lithography tools require the use of photomasks which consist of patterned chromium coated quartz plates that contain the image of the pattern that is desired. Production of these photomasks must be accomplished with some other high resolution “maskless” lithography technique.

1.1.2 E-beam Lithography

The most widely used “maskless” lithography technique is electron beam lithography. In this method, a focused beam of electrons (i.e. spot sizes on the order of 2-3 nm have been demonstrated) is used to directly draw the pattern of interest into a radiation sensitive material such as a polymer photoresist. This technique has demonstrated extremely high resolution, with sub-20nm features being produced by e-beam lithography here at Georgia Tech.[5] In fact, electron beam lithography has once again displaced maskless optical lithography methods as the technique of choice for

producing the high resolution photomasks required for optical lithography. However, production worthy electron beam lithography tools capable of such high resolution are also extremely expensive (e.g. typical tools cost is in the range of \$10M to \$20M) and their writing speed and throughput is extremely low. This slow speed is due to the serial nature of e-beam writing techniques which traditionally utilize only a single beam to draw out the complete pattern.[2] While attempts have been made to make multi-beam [6,7] and projection electron [8,9,10] beam tools which would be capable of substantially higher throughputs and writing speeds, no commercially successful technology has been developed yet due to a variety of problems encountered with such methods. In addition, the projected tool cost for such methods are comparable or higher than even current optical lithography systems. In general, there is a substantial opportunity for methods which have resolutions comparable to direct write e-beam lithography but possess substantially higher throughputs and writing speeds.

1.1.3 Nanoimprinting

A recent and potentially disruptive class of nanopatterning technologies is so-called “nanoimprinting”. Nanoimprinting is commonly used to refer to both physical thermal embossing methods [11,12] and the more recent “step-and-flash” imprint photopolymerization techniques. [13] Both techniques have been demonstrated to possess resolutions below 25 nm. In addition, the tool costs for imprinting methods are projected to be up to an order of magnitude lower than other current lithography tool sets with comparable resolution. However, imprint methods also suffer from a number of issues which may limit their success and application. For example, imprint methods are a “1X” technology meaning that they require templates or masks with the exact feature sizes that

must be imprinted. Fabrication of these templates again requires the use of extremely high resolution “maskless” lithography techniques. Furthermore, imprinting sparse patterns or patterns which combine extremely small and large features on the same layer can be problematic. So while imprinting is promising, it is not a general solution for all sub-100nm lithography needs and does not address the need for higher throughput “maskless” lithography technologies at all.

1.2 Scanning Probe Lithography Methods: Mechanical Scratch, Field Emission, Oxidation, and Dip-Pen Nano-Lithography (DPN)

Recently, the use of atomic force microscope (AFM) cantilever probe methods for high resolution lithography has been explored. Since an AFM has the capability of manipulate material directly at the atomic level, it certainly shows the potential to reach the high resolution patterning demands of microelectronics and other applications which require fabrication of nanoscale structures. While many different mechanisms have been applied to make nanoscale structures using an AFM, no methodology for making robust three dimensional arbitrary relief structures with high throughputs has demonstrated. However, a particularly exciting development in this regard has been the development of large arrays of heated AFM cantilever probes. [14] Although these thermal cantilever arrays were originally developed for data storage applications by IBM, they provide a basic tool set with which to envision development of high throughput, high resolution thermal lithography techniques. The basic hypothesis of this work is that it is possible to develop materials and processes that produce patterned material structures using local thermally induced physiochemical changes to thin film materials and which can produce resolutions approaching the AFM probe tip radius of curvature (i.e. probe tips with radius

of curvature in the range of 5 to 50 nm can currently be manufactured [15]. In order to better understand the contribution and context of this work, a further discussion of alternative probe based lithography methods is required.

1.2.1 Mechanical Scratching

One of the simplest methods for AFM lithography is to use the probe tip to scratch a surface to obtain a pattern. By applying a sufficient force on the tip, the tip can be made to indent and scratch the surface as it scans. AFM tips have been successfully used to scratch a variety of both soft and hard surfaces. [16,17] One of the main problems with this method is the excessive wear of the tip which degrades the writing resolution and control of the process. Some success at increasing the lifetime of probe tips used for such methods was achieved by coating the tip with hard materials (e.g. diamond), but the scratching method has not received any serious attention as a true manufacturing technique.[18]

1.2.2 Field Emission

Majumdar and workers used a gold coated AFM tip to perform local electron exposure of a thin PMMA film coated on metallic substrate by applying a bias voltage between the tip and the substrate. When the bias voltage was applied, the gold coated AFM tip became an electron source used to expose the PMMA resist resulting in chain scission of the PMMA in much the same way as in conventional electron beam lithography using PMMA. By modulating the bias voltage, patterns could be exposed into the PMMA as the AFM tip scanned the surface. Following exposure, patterns were developed in the PMMA by washing the film in an appropriate solvent to remove the exposed lower molecular weight polymer. A line-space pattern consisting of

approximately 35 nm wide lines on a 68 nm pitch was produced using this technique. While this method is very similar to conventional e-beam lithography, it offers two possible advantages: (1) a substantially lower voltage is used for field emission from the AFM tip as compared to conventional electron beam columns thus reducing electron beam induced substrate damage and (2) the AFM exposure is performed in a room air ambient as compared to the expensive high vacuum environment required for conventional e-beam tools. Also, by controlling the probe height a non-contact exposure mode can be achieved which reduces any tip wearing problems. In addition to PMMA, a variety of other materials have also been successfully patterned using the field emission current from an AFM tip.[19,20,21] However, field emission methods using the AFM tip also have a variety of issues, such as difficulty writing on insulating substrates and the need for electron beam sensitivity in the imaging material, which have also proved to be somewhat limiting in terms of its application.

1.2.3 Oxidation

Although field emission electron beam exposure from the AFM tip has received a significant amount of attention, many other methods have also been investigated for using the AFM probe tip to modify and pattern material surfaces at the nanoscale. Sugimura and coworkers used conductive AFM tips to locally electrochemically degrade an organosilane monolayer.[22] A spatial resolution of 20 nm was obtained while scanning speeds as high as 5000 $\mu\text{m}/\text{sec}$ were achieved. Dai and coworkers [23] introduced single-walled carbon nanotube (SWNT) tipped AFM cantilevers into the AFM nano-oxidation process, and used these tips to locally oxidize a Ti metal film on an

atomically flat alpha-Al₂O₃ substrate. Using this method they were able to form ultra-narrow oxidized titania lines of 5 nm width.

1.2.4 DPN

More recently, a technique referred to as “Dip Pen Nanolithography” (DPN) has been reported. [24] This method coats the AFM tip with a thin film of a molecular “ink” which can be transferred to the substrate surface when the tip is in contact with the surface in the same manner as a quill pen. In this way, nanoscale monolayer patterns can be written onto the substrate surface using a directly additive process. Various materials, including inorganics, organics, biomolecules, and polymers have been deposited onto a variety of substrates using this method.[25,26,27] Feature sizes as small as 10-15 nm have been demonstrated using this technique.[28] While the direct additive nature of the process can be advantageous for some applications, DPN methods have a variety of limitations including: (1) writing is started and stopped by engaging or disengaging the probe tip from the surface which is a slow process, (2) only extremely thin (i.e. on the order of a single or few monolayers) can be written easily in each writing pass, and (3) the tip must be reinked if large areas are written which can also slow down the writing process substantially.

As can be seen from this short literature review, the AFM has already been used in a variety of ways to achieve nanoscale patterning. Table 1 provides a comparison of the common classes of lithographic methods. From this comparison, it can be seen that AFM lithography has at least a significant potential as a faster maskless patterning technique than e-beam direct write methods. However, there is still opportunity for development of more robust, faster, and more versatile AFM lithography methods. In

particular, methods that would be suited for practical nanomanufacturing applications and which are more compatible with current microfabrication processes and materials would be extremely useful. The development of such new methods is one of the overarching goals of this work. To this end, heated AFM cantilever probes will be explored as a platform for developing more versatile and higher throughput lithographic methods.

Table 1-1. Comparison of AFM lithography with other lithography methods

Lithography Method	AFM	Optical	E-beam	Imprinting
Feature size achieved (nm)	3	50	10	25
Speed	Low-Medium	High	Low	High
High vacuum	No	No	Yes	No
Maskless	Yes	No	Yes	No
Imaging simultaneous	Yes	No	No	No

1.3 Thermal AFM Probes

Heated AFM cantilevers were first used by Mamin [29] to make nanoindentations in a polymethyl methacrylate (PMMA) substrate. In this original work the cantilever was heated by a pulsed infrared laser to a temperature above the softening point of PMMA. Only the material in the vicinity of contact with the heated tip was softened, and this region of the polymer was indented only when sufficient force was applied to the tip. Using this method, pits as small as a few tens of nanometers in diameter were made in the PMMA substrate.

This patterning technology was deemed to show great potential for data storage applications at the time because a data storage density of $2-3 \times 10^{10}$ bits/in² was achieved with the AFM method which was well above the data storage density of 6×10^8 bits/in² of

magnetic recording products at that time. However, a major problem at that time was that the mechanical resonant frequency of the AFM cantilevers limited the data storage rates to a few Mb/sec for a single cantilever which was lower than that achievable with magnetic storage. The most obvious solution for this data rate problem was to perform parallel operation of a large array of cantilevers to simultaneously write many data streams at once. However, the method of using the laser to heat the cantilever requires an external light source and precise focus and alignment of the laser spot on the probe tip. Furthermore, deflection measurement of the cantilever required yet another external laser source with the same issues. These two factors made integration of more than a few cantilevers into an array difficult or impossible. The solution to these problems was to move away from external heating and measurement laser sources by integrating the heating and position sensing functionalities directly into each cantilever probe. This was achieved by fabricating a resistive heating element in the tip and using a piezoresistive cantilever.[30] The cantilever design was further improved to achieve heating times of less than 1 μ s and cooling times less than 10 μ s.[31] IBM has explored this technology for data storage applications and has now demonstrated the parallel operation of large arrays of heated cantilevers for such applications. IBM has named this technology “Millipede” and has for example used 32x32 heated cantilever arrays to demonstrate data storage densities of 400-500 Gbit/in². Initial nanomechanical experiments done at the IBM Almaden Research Center showed that individual tips could support data rates as high as 1 - 2 megabits per second.

The fact that such heated cantilever arrays can be scaled to large numbers of cantilevers easily, thus enabling massively parallel thermal patterning processes, has

inspired the work in this project. The fact that cantilevers have already been shown to be able to thermally indent a polymer surface with a pit size on the order of 10 to 20 nanometers at a high speed show that nanoscale patterning of materials using such tools is conceptually possible. Most of the temperature rise in the polymer or substrate film contacted by the heated cantilever tip is believed to occur directly in the contact area of the tip, with less than 5% of the overall temperature rise occurring in substrate away from the tip-substrate contact.[32] King and coworkers have predicted that the hot spot created by a heated cantilever can be as small as 2 nm and that the temperature of the substrate can be heated to over 500 °C at the tip-substrate contact using silicon cantilevers.[33] However, the use of indenting type processes is not well suited for producing nanopatterns other than data storage pits, i.e. such as continuous line patterns. There is a significant need to explore and develop new nanoscale thermal patterning materials and processes which could utilize the thermal cantilever arrays to produce arbitrary nanopatterned structures. Development of such materials and processes is the focus of this project.

1.4 Organization of Thesis

In thinking about the possible thermal patterning operations that could be achieved using a nanoscale thermal probe tip, the following ideas will be explored in this work:

1. Selectively thermally decompose material in contact with the probe tip.
2. Use thermal probe lithography patterned polymer as masking layer for deposition of other materials.

3. Thermally induce surface modification of polymer surface, and selectively deposit material on the modified polymer surface.
4. Thermally pattern Self Assembly Monolayers (SAMs), and use patterned SAMs for selectively deposition of other materials.

Since the thermal writing is not a standard operation mode for commercial AFM, the pre-request of this project is to setup a thermal probe nanolithography tool. Chapter 2 focuses on the instrument part of this work. A commercial AFM system was modified to make a thermal probe nanolithography tool. A special thermal cantilever holder was designed and manufactured. Detailed description of the thermal writing process is presented. Some background of AFM is also included. Chapter 3 presents the first idea we've worked on in this project, selectively decomposition of polymers using heated AFM probes. Some new materials were developed particularly for this application. Effect of material properties on thermal writing process was investigated. The thermal decomposition method was initially proposed for make two dimensional pattern. But during experiments, we found the decomposition depth can be very well controlled with a combination of scan speed and heating temperature. So we further explored this method, and developed a 3D thermal writing technology, which is reported in Chapter 4. Making polymer patterns is not the final purpose of nanolithography. Usually the polymer pattern made by lithography step is for patterning other materials. Chapter 5 reports a successful ALD deposition of materials using thermal probe lithography patterned polymer thin film as the masking layer. Because the resolution limitation of the film thickness for selectively decomposition method, we also tried to explore other alternative methods which have no such resolution limitation. In Chapter 6, we focus on one of the alternative

methods, top surface imaging (TSI). Some new materials were developed for this specific application, detailed investigation of the effects of material properties on the process was conducted. The other alternative method we explored is thermal patterning self assembly monolayer (SAMs), which is presented in Chapter 7. Some simulation and modeling work is presented in Chapter 8. FemLab was used to simulate the heating of a thermal cantilever, and analyze the heat transport in the thermal cantilever during thermal writing. A basic model for the selectively decomposition method is introduced.

1.5 References

- [1] <http://www.itrs.net/> (03/2008)
- [2] Larry F. Thompson, C. Grant Willson, Murrae J. Bowden, Introduction to Microlithography (2nd Edition), (ACS professional reference book) 1994
- [3] Hinsberg, William D.; Houle, Frances A.; Sanchez, Martha I.; Hoffnagle, John A.; Wallraff, Gregory M.; Medeiros, David R.; Gallatin, Gregg M.; Cobb, Jonathan L. Extendibility of chemically amplified resists: another brick wall? Proceedings of SPIE-The International Society for Optical Engineering (2003), 5039(Pt. 1, Advances in Resist Technology and Processing XX), 1-14
- [4] Schmid, Gerard M.; Stewart, Michael D.; Wang, Chia-Ying; Vogt, Bryan D.; Prabhu, Vivek M.; Lin, Eric K.; Willson, C. G. Resolution limitations in chemically amplified photoresist systems. Proceedings of SPIE-The International Society for Optical Engineering (2004), 5376(Pt. 1, Advances in Resist Technology and Processing XXI), 333-342
- [5] <http://grover.mirc.gatech.edu/> (03/2008)
- [6] Wiesner, John C. (Etec Systems, Inc., USA), Multi-beam array electron optics, WO 9848443
- [7] Hamaguchi, Shinichi; Haraguchi, Takeshi; Yasuda, Hiroshi. US 20010028042

- [8] Berger, S. D.; Gibson, J. M. New approach to projection-electron lithography with demonstrated 0.1 mm linewidth. *Applied Physics Letters* (1990), 57(2), 153-5
- [9] Pfeiffer, H. C.; Stickel, W. PREVAIL - An e-beam stepper with variable axis immersion lenses. *Microelectronic Engineering* (1995), 27(1-4), 143-6
- [10] Utsumi, Takao. Low energy electron-beam proximity projection lithography: Discovery of a missing link. *Journal of Vacuum Science & Technology, B: Microelectronics and Nanometer Structures* (1999), 17(6), 2897-2902.
- [11] Chou, Stephen Y.; Krauss, Peter R.; Renstrom, Preston J. Imprint lithography with 25-nanometer resolution. *Science (Washington, D. C.)* (1996), 272(5258), 85-7.
- [12] Chou, Stephen Y.; Krauss, Peter R. Imprint lithography with sub-10nm feature size and high throughput. *Microelectronic Engineering* (1997), 35(1-4, Micro- and Nano-Engineering 96), 237-240.
- [13] Colburn, Matthew; Johnson, Stephen; Stewart, Michael; Damle, S.; Bailey, Todd C.; Choi, Bernard; Wedlake, M.; Michaelson, Timothy; Sreenivasan, S. V.; Ekerdt, J.; Willson, C. G. Step and flash imprint lithography: a new approach to high-resolution patterning. *Proceedings of SPIE-The International Society for Optical Engineering* (1999), 3676(Pt. 1, Emerging Lithographic Technologies III), 379-389.
- [14] Vettiger, P.; Despont, M.; Drechsler, U.; Durig, U.; Haberle, W.; Lutwyche, M. I.; Rothuizen, H. E.; Stutz, R.; Widmer, R.; Binnig, G. K. The "Millipede"-more than one thousand tips for future AFM data storage. *IBM Journal of Research and Development* (2000), 44(3), 323-340
- [15] <http://www.nanosensors.com/> (03/2008)
- [16] Magno, R.; Bennett, B. R. Nanostructure patterns written in III-V semiconductors by an atomic force microscope. *Applied Physics Letters* (1997), 70(14), 1855-1857.
- [17] Sugihara, Hideki; Takahara, Atsushi; Kajiyama, Tisato. Mechanical nanofabrication of lignoceric acid monolayer with atomic force microscopy. *Journal of Vacuum Science & Technology, B: Microelectronics and Nanometer Structures* (2001), 19(2), 593-595.
- [18] Fonseca Filho, H. D.; Mauricio, M. H. P.; Ponciano, C. R.; Prioli, R.. Metal layer mask patterning by force microscopy lithography. *Materials Science &*

- Engineering, B: Solid-State Materials for Advanced Technology (2004), B112(2-3), 194-199.
- [19] K. Wilder, C. F. Quate, D. Adderton, R. Bernstein, and V. Elings, Noncontact nanolithography using the atomic force microscope. *Applied Physics Letters* (1998), 73(17), 2527-2529
- [20] Davidsson, P.; Lindell, A.; Makela, T.; Paalanen, M.; Pekola, J. Nanolithography by electron exposure using an Atomic Force Microscope. *Microelectronic Engineering* (1999), 45(1), 1-8
- [21] Christie R. K. Marrian *Technology of Proximal Probe Lithography*, SPIE Press, 1993
- [22] Sugimura, Hiroyuki; Nakagiri, Nobuyuki. AFM lithography in constant current mode. *Nanotechnology* (1997), 8(3A), A15-A18
- [23] Gotoh, Y.; Matsumoto, K.; Maeda, T.; Cooper, E. B.; Manalis, S. R.; Fang, H.; Minne, S. C.; Hunt, T.; Dai, H.; Harris, J.; Quate, C. F. Experimental and theoretical results of room-temperature single-electron transistor formed by the atomic force microscope nano-oxidation process. *Journal of Vacuum Science & Technology, A: Vacuum, Surfaces, and Films* (2000), 18(4, Pt. 1), 1321-1325
- [24] Piner, Richard D.; Zhu, Jin; Xu, Feng; Hong, Seunghun; Mirkin, Chad A. "Dip-pen" nanolithography. *Science (Washington, D. C.)* (1999), 283(5402), 661-663
- [25] Su, Ming; Dravid, Vinayak P.. Colored ink dip-pen nanolithography. *Applied Physics Letters* (2002), 80(23), 4434-4436.
- [26] Demers, L. M.; Ginger, D. S.; Park, S.-J.; Li, Z.; Chung, S.-W.; Mirkin, C. A. Direct patterning of modified oligonucleotides on metals and insulators by dip-pen nanolithography. *Science (Washington, DC, United States)* (2002), 296(5574), 1836-1838
- [27] Jung, Hyungil; Kulkarni, Rajan; Collier, C. Patrick. Dip-pen nanolithography of reactive alkoxysilanes on glass. *Journal of the American Chemical Society* (2003), 125(40), 12096-12097
- [28] Mirkin, Chad A.; Hong, Seunghun; Demers, Linette. Dip-pen nanolithography: controlling surface architecture on the sub-100 nanometer length scale. *ChemPhysChem* (2001), 2(1), 37-39.
- [29] Mamin, H. J.; Rugar, D.. Thermomechanical Writing with an Atomic Force

Microscope Tip. *Applied Physics Letters* (1992), 61(8), 1003-5

- [30] Mamin, H. J.. Thermal writing using a heated atomic force microscope tip. *Applied Physics Letters* (1996), 69(3), 433-435.
- [31] B. W. Chui, T. D. Stowe, Y. S. Ju, K. E. Goodson, T. W. Kenny, H. J. Mamin, B. D. Terris, and R. P. Ried, Low-stiffness silicon cantilevers with integrated heaters and piezoresistive sensors for high-density AFM thermomechanical data storage. *Journal of Microelectromechanical Systems* (1998) 7(1), 69–78.
- [32] King, W. P.; Goodson, K. E.. Thermomechanical formation and thermal detection of polymer nanostructures. *Developments in Heat Transfer* (2004), 13(Heat and Fluid Flow in Microscale and Nanoscale Structures), 131-171
- [33] King, William P.; Goodson, Kenneth E.. Resolution limits of nanoscale thermal processing with the atomic force microscope. *HTD (American Society of Mechanical Engineers)* (2002), 372-5(Proceedings of the ASME Heat Transfer Division--2002, Volume 5), 277-282

CHAPTER 2

INSTRUMENTS

2.1 AFM Systems

Atomic force microscopy (AFM) is a high-resolution surface imaging technique that can resolve features as small as an atomic lattice.[1] It has been a revelation in allowing researchers to directly observe molecular and atomic level features and events on surfaces.[2]

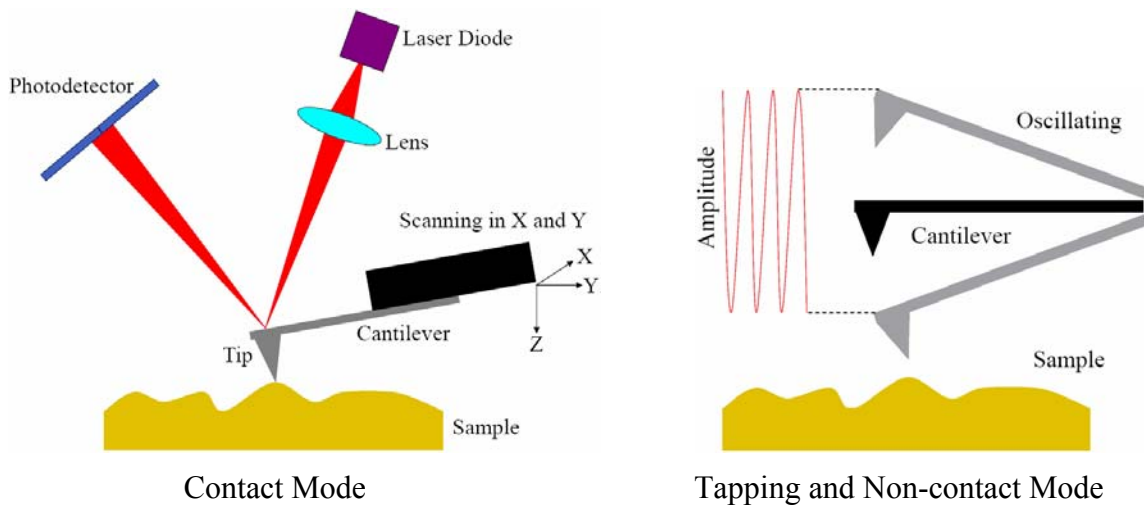


Figure 2-1. Different AFM modes

For imaging purposes, the AFM can generally work in three different modes: contact mode, intermittent contact mode (commonly referred to as “tapping mode” [3]), and non-contact mode (See Figure 2-1). [4] In contact mode, the AFM works by bringing a cantilever tip in contact with the surface to be imaged. A repulsive force from the surface applied to the tip bends the cantilever upwards. The amount of bending, measured by a laser spot reflected onto position sensitive photodiode (PSPD), can be used to calculate the force. By keeping the force constant while scanning the tip across

the surface, the vertical movement of the tip, which is usually driven by a Z piezo, follows the surface profile and is recorded as the surface topography by the AFM. Because the tip is physically in contact with substrate surface, there is some friction force applied to the tip while it is scanning on the surface. This friction force (or lateral force) also can be detected by the PSPD, and recorded to form an image. This image is usually called friction image, which contains surface property information of the substrate. This information is very useful for detecting different regions with different friction coefficient in a heterogeneous surface. In the tapping mode and non-contact mode, the AFM cantilever vibrates at a high frequency (close to the cantilever's resonance frequency). Because of the force interaction between the tip and the surface, the resonance frequency shifts down, then the amplitude of the vibration of the cantilever changes. By maintaining constant amplitude of the tip vibration, the tip again can be controlled to follow and record the topography of the surface. In tapping mode and non-contact mode, since the cantilever is vibrating, the lateral force between the tip and the substrate is minimized, and scratching can be prevented. This is very important for imaging of soft materials or sticky materials. Tapping mode and non-contact mode are both dynamic mode, but they are different. Tapping mode usually operated with high oscillation amplitude (20-100nm), and the tip strikes the surface. When the cantilever strikes the surface, the phase lag between the cantilever oscillation and the driven signal also depends on the surface properties, e.g. hardness, stickiness, etc. This information usually can be recorded in the phase image of the tapping mode. So tapping mode is also very useful for material science and polymer science [5]. The striking force in tapping mode can be even higher than that in most contact mode. And the tiny tip on the AFM

cantilever is very fragile. In tapping mode, there is the risk that the tip can be worn or broken very quickly, especially when imaging hard surface. But in non-contact mode, the cantilever can oscillate at lower oscillation amplitude, and the tip can stay in the attractive force region, and doesn't touch the surface. In order to operate, the Z piezo for non-contact mode must have much fast response time than that for other modes, to keep the tip stay in non-contact status. The biggest advantage of non-contact mode is the tip wearing is minimized. This is very important for imaging sub-10nm feature or high volume imaging tasks. But because the tip stays in non-contact with surface, there is less material property information can be obtained from normal non-contact mode.

The AFM system used in this research work is a PicoPlus AFM from Molecular Imaging. It is equipped with a large scale multi-purpose close-loop scanner. The AFM can be operated in both contact mode and tapping mode.

2.2 Thermal Cantilever Characterization: Radius of Curvature, Temperature Calibration, and Spring Constant Measurement

Thermal cantilevers used in this research work are obtained from Prof. King at University of Illinois at Urbana-Champaign. The cantilevers are made of doped single crystal silicon [6]. The fabrication, characterization, and use of these probes have been reported elsewhere.[7,8,9,10,11,12] An electrical resistance heater-thermometer integrated into the silicon cantilever allows for temperature-controlled heating. Figure 2-2 shows a SEM image of a typical thermal cantilever used in this work.

2.2.1 Radius of Curvature

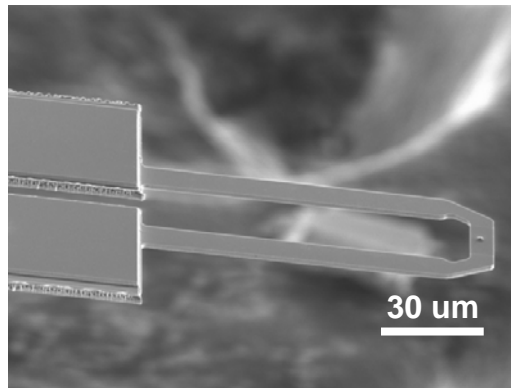


Figure 2-2. SEM image of a thermal cantilever

The dimension of the minimum feature can be made by this probe lithography method is directly related to the size of the cantilever. Radius of curvature of the tip is the most important parameter to characterize the sharpness of the tip. There are a couple of different ways to measure the radius of curvature. One of them is reverse imaging. In this method, the cantilever is used to image surfaces containing sharp features, e.g. sharp edges, sharp peaks. Because the features are so sharp, the geometry of the very end of the tip is convolved into the topography image obtained this tip. Then by using tip deconvolution, the tip shape can be calculated [13,14]. This method is very easy to operate, and relative lost cost. But the sharp features on the surface can't be very tall because they are so tiny. This method can only be used to obtain geometry of the very top the tip. Also because the accurate dimension of the sharp feature is usually unknown, and the radius of curvature of these features are not infinite small (usually $>5\text{nm}$), this method can't be used to obtain an accurate measurement of the radius of a very sharp tip.

Another very often used method to measure the radius of curvature of a cantilever tip is high resolution scanning electron microscope (SEM). SEM can be used to directly measure the accurate geometry of the entire cantilever tip, as well as the very top of the tip without any other process. But it is high cost, and takes more time. And it is only available to those who have access to high resolution SEM equipment. Fortunately, there is high resolution SEM (Leo-1530 SEM) available in Georgia Tech. Figure 2-3 shows SEM images of thermal cantilever tip. The estimated radius of the curvature of the cantilever tip is about 30 nm.

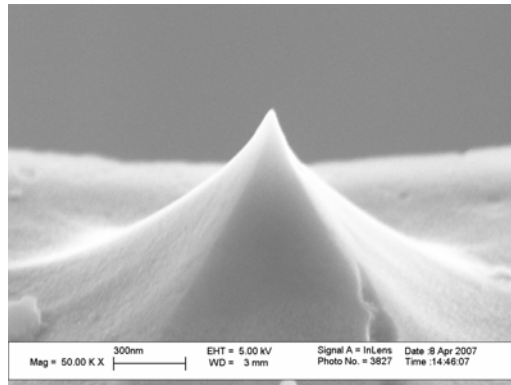


Figure 2-3. SEM images of thermal cantilever tip

2.2.2 Temperature Calibration

The thermal cantilever used in this work can reach temperature to above 1000 °C.[15] Cantilever heating power can be used to roughly estimate the heating temperature of a specific cantilever. But with the same heating power, the cantilever heating temperature can vary over +/- 50 degree depends on the distance of the cantilever to the substrate, which directly determines the heat dissipation through the gap between cantilever and substrate. So the cantilever resistance is also used to monitor the heating

temperature of the cantilever. Each thermal cantilever has slightly different relation between the resistance and heating temperature (R-T curve). Each thermal cantilever needs to be individually calibrated. During calibration, the cantilever heater temperature is measured by Ramen thermometry with accuracy with 5 °C.

For the temperature calibration, first a resistance versus heating power curve was obtained by increasing the heating voltage from 0 to a certain value, and measuring the heating power and cantilever resistance simultaneously. Figure 2-4 shows a resistance-heating power curve of a typical thermal cantilever. We can see there is a peak resistance of the cantilever. The resistance of the cantilever first increases, and then decreases above certain heating voltage. The increase of the resistance of the cantilever is due to the increase of heating temperature. In micro scale, as the temperature increases, the thermal vibration of the atoms in the cantilever increase, then the resistance to the movement of electrical carrier (electrons or holes) increase. In macro scale, the electrical resistance of the cantilever increase. The cantilever is made of doped silicon, which has smaller band gap than insulator. When the heating temperature increase to a certain point, the thermal energy can overcome the band gap energy of some electrons in the covalent band, and excite them into conducting band. Then there will be more electrical carrier in the material. And the electrical resistance of the cantilever decreases.

Because too high temperature may burn the cantilever, normally the cantilever is operated at a temperature below the point which has the peak resistance.

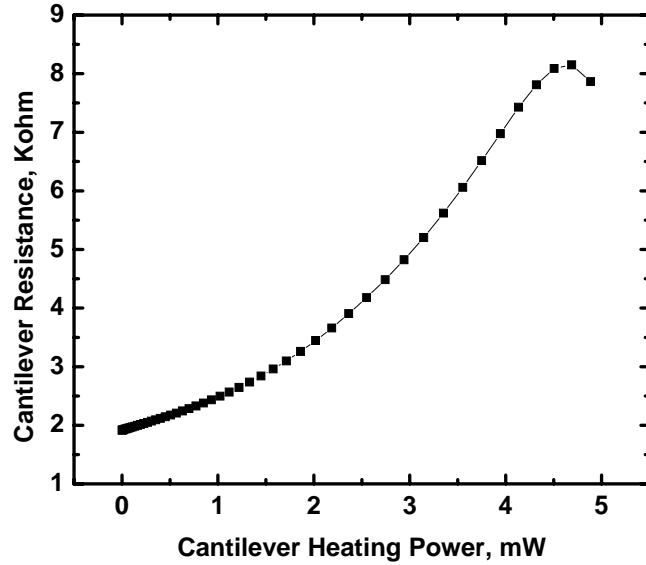


Figure 2-4, resistance vs. heating power of a typical thermal cantilever

Then ramen thermometry was used to measure the cantilever heater temperature at a couple of different heating power (see Figure 2-4). According to simulation results, the cantilever temperature-heating power relation follows the second order polynomial (see Chapter 8). So the experimental temperature-heating power data were then fitted by a second order polynomial, with an almost unit R^2 . This somewhat proves the simulation results, and that we can use this second order polynomial relation to extrapolate the experimental ramen thermometry calibration data to a range which is out the calibrated temperature range. By using the second order polynomial formulation obtained by fitting the calibration data, all cantilever heating power values in Figure 2-4 can be converted into temperature. Then plot it again versus the cantilever resistance value (see Figure 2-6).

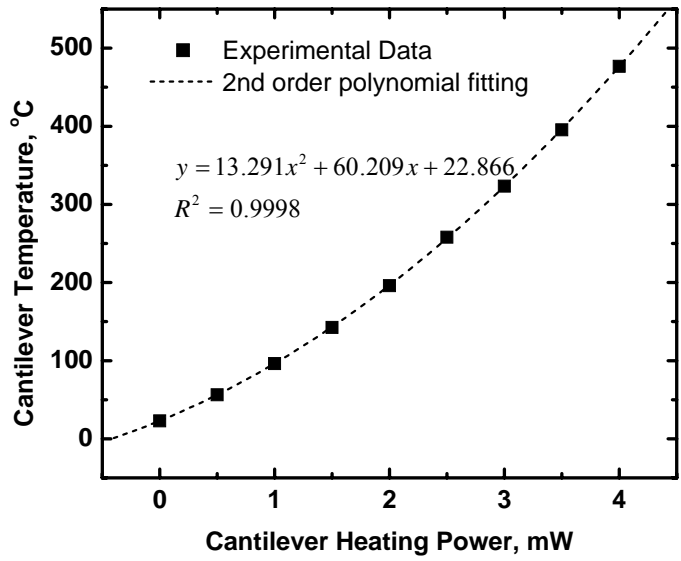


Figure 2-5, cantilever heater temperature vs. heating power of a typical thermal cantilever

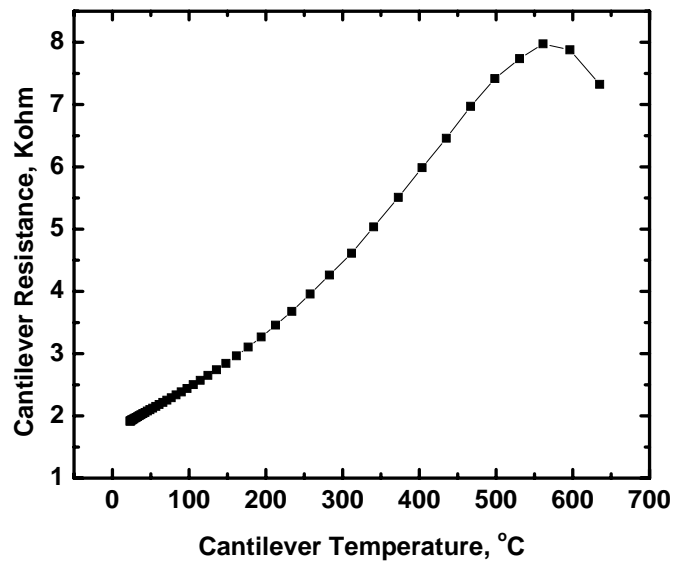


Figure 2-6, cantilever resistance vs. cantilever heater temperature

By using this plot, we can calculate the heating temperature at each cantilever resistance value. In practical, the combination of the heating power and cantilever resistance is used to determine the heating temperature.

2.2.3 Spring Constant Calibration

Spring constant is another important parameter of cantilever, especially for force measurements [16]. For thermal writing experiment, spring constant is not that important, but it is still good to know the coarse value. Spring constant determines the loading force applied to the cantilever when the cantilever is bended in a certain degree against the substrate. In thermal writing experiment, loading force affects the contact area between the tip and the substrate, and the heat transport through the contact area.

There are a couple of different strategy for measuring the spring constant of a cantilever [17,18]. In this work, the spring constant of a thermal cantilever was measured by a method which is close to the one described by Gibson and his coworkers [19]. The method used in this work is described in Figure 2-7. To determine the spring constant of a thermal cantilever, a commercial cantilever with known spring constant was used as reference. The reference cantilever was attached on a sample substrate with a double side tape. The tip of the reference cantilever faced down. A thermal cantilever was mounted on the piazo scanner. The first force-distance curve of the thermal cantilever was obtained on a hard surface, e.g. the chip area of the cantilever probe. Then by adjusting the sample stage in lateral direction, the thermal cantilever tip was aligned to the backside of head of the reference cantilever, and a second force-distance curve is obtained at this spot.



Figure 2-7, measurement of spring constant of a thermal cantilever

Those two force-distance curves are shown in Figure 2-8. In the first force-distance curve, because the surface is hard, the deformation of the surface is negligible compare to the deflection of the soft cantilever. Then the Z piezo displacement is equal to the deflection of the thermal cantilever. By this mean, the cantilever defection signal, which is in voltage, can be calibrated. From Figure 2-8, we can see that 1 voltage of deflection equals to 100 nm. In the second force-distance curve, because the reference cantilever is also soft, both the thermal cantilever and the reference cantilever are bended. The bending degrees for those two cantilevers are different, but the loading forces between them are the same. From Figure 2-8, we can see when the Z piezo moves down for 100 nm, the deflection signal from the thermal cantilever is only 0.27 voltages. According to the calibration, 0.27 voltages equals to 27 nm deflection for the thermal cantilever. So the other 73 nm deflection is from the bending of the reference cantilever.

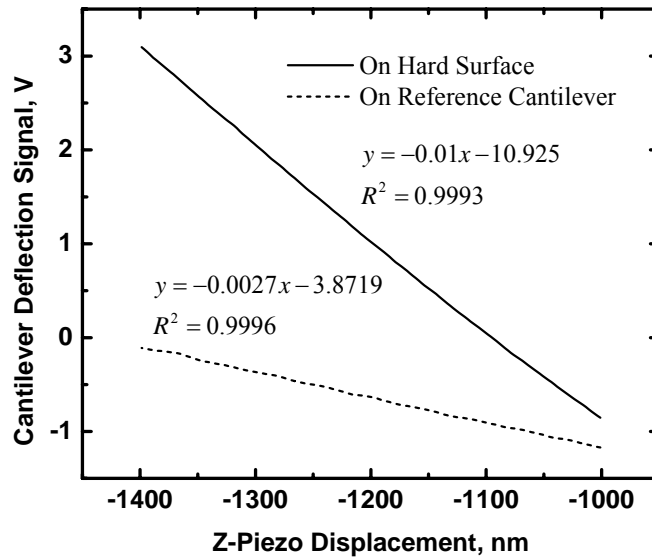


Figure 2-8, Force-distance of curves of a thermal cantilever

Spring constant of the reference cantilever is $K_r = 0.13$ N/m. The loading force on each cantilever is the same, then we should have following relation: $K_c \cdot 27\text{nm} = K_r \cdot 73\text{nm}$, then $K_c = 0.35$ N/m.

2.3 Thermal Writing AFM: Cantilever Holder, Heating Circuit, and Thermal Writing Controlling

2.3.1 Cantilever Holder

The thermal cantilever used in this research work could not fit in the cantilever holder came with the AFM system. A special cantilever holder was designed by the author, and fabricated in the machine shop at the School of Chemical & Biomolecular Engineering at Georgia Tech.

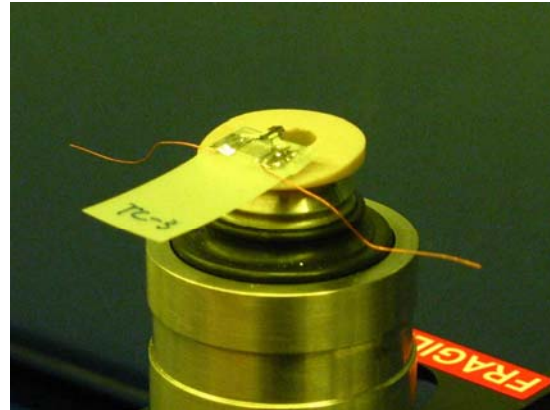


Figure 2-9. Special designed cantilever holder for thermal cantilever

Figure 2-9 shows an AutoCAD drawing of the special designed thermal cantilever holder, and an image of the assembly of the thermal cantilever, cantilever holder, and the AFM scanner. A magnet is attached to the holder permanently. And the thermal cantilever is glued onto another magnet with electrical connection of copper wires. Then this assembled thermal cantilever can be easily mounted onto the holder using magnetic force.

The advantages of this design are: 1) it is very easy to mount or take off the thermal cantilever from the cantilever holder, and it is not necessary to take out the scanner from the base; 2) the cantilever is self aligned, this is because those two magnets (one is on the holder, and one is in the cantilever assembly) try to maximum the overlap area.

2.3.2 Heating Circuit

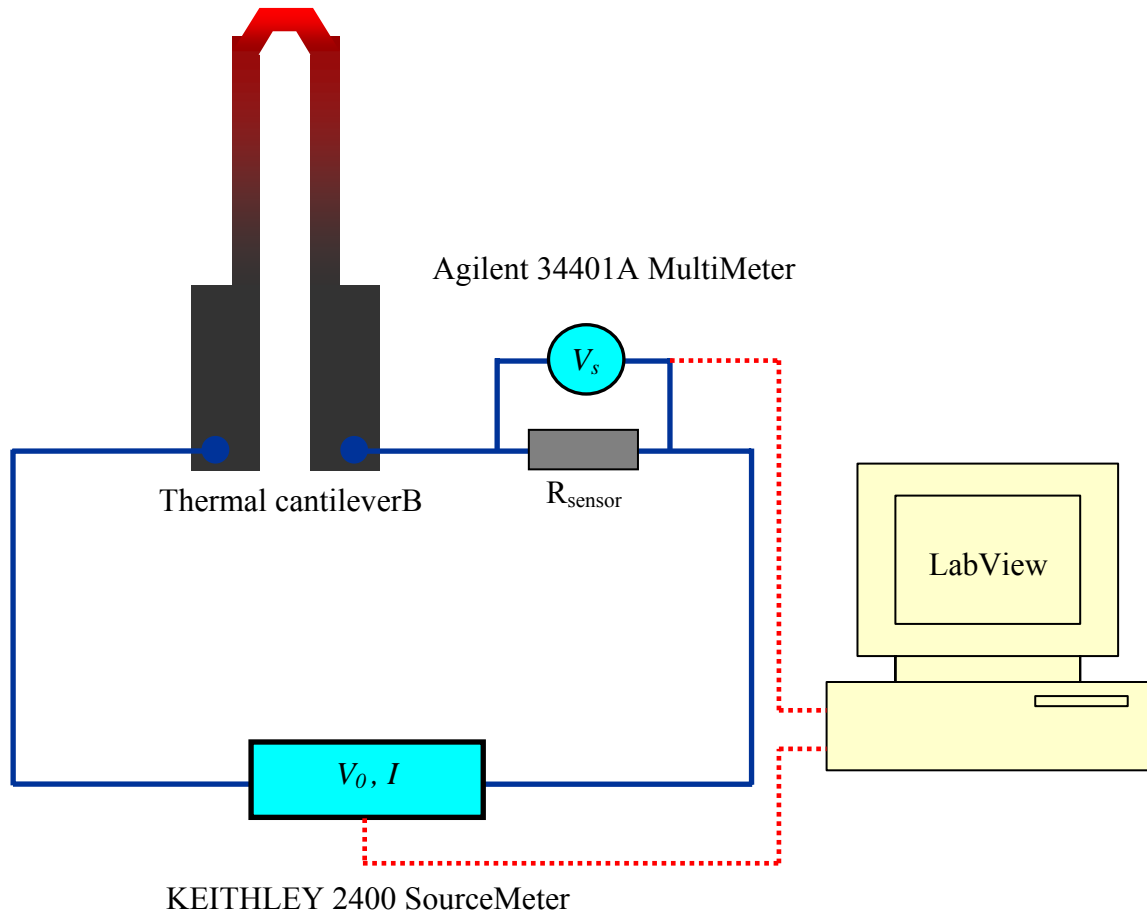


Figure 2-10. Diagram of heating circuit for thermal cantilever

A simple electrical heating circuit (see Figure 2-10) is used to heat the thermal cantilever [20]. In the circuit, a resistor, with resistance of R_s , is connected to the thermal cantilever in series as the sensor resistor for electrical measurement and protection of thermal cantilever. A Keithler 2400 sourcemeter is used to provide a constant voltage (V_0) power source and it also gives the electrical current value (I) in the circuit. An Agilent 34401A multimeter is used to measure the voltage applied to the sensor resistor (V_s). As mentioned previously, the cantilever heating power (P_c), and cantilever

resistance (R_c) are used to monitor the heating temperature. These two values can be easily calculated using following equations.

$$\begin{aligned}
 R_c &= \frac{(V_0 - V_s)}{I} \\
 V_c &= \left(\frac{R_c}{R_c + R_s} \right) \times V_0 \\
 P_c &= \frac{V_c^2}{R_c} = \frac{R_c}{(R_c + R_s)} \times V_0^2 \\
 \frac{dP_c}{dR_c} &= \frac{V_0^2}{(R_c + R_s)^2} - \frac{2R_c V_0^2}{(R_c + R_s)^3} = \left(1 - \frac{2R_c}{R_c + R_s} \right) \times \frac{V_0^2}{(R_c + R_s)^2}
 \end{aligned}
 \tag{2-1}$$

The resistance of a good thermal cantilever first increases as temperature increase because of the increase of the thermal impedance to electrical current. But when the temperature reaches certain point, usually around 600 °C, the resistance of the thermal cantilever starts to decrease because of the increase of electrical carrier. So for a good cantilever, there is a peak resistance value at a heating temperature around 600 °C. Usually it is safe to operate the cantilever under this temperature, and the cantilever performance is stable. And it is not good to operate the cantilever at temperature too high above the peak resistance temperature, because there is some risk to burn the cantilever. Even if a temperature above the peak resistance temperature is need, we want the cantilever have a steady heating temperature, and prevent it from over heated to too high temperature.

According to Equation 2-1, when $R_s > R_c$, $dP/dR_c > 0$. So in this case, when we operate the cantilever at a temperature over the peak resistance temperature, if the cantilever resistance decreases a little bit, the cantilever heating power will also decrease a little bit. Subsequently, cantilever temperature will decrease too. This gives a negative

feed back to the cantilever resistance change, and tries to keep the cantilever resistance and temperature steady.

Usually, a good thermal cantilever has a peak resistance around 8 kohm. So 10 kohm will be a good resistance value for a sensor resistor to keep the thermal cantilever operating with steady performance even when a temperature above the peak resistance temperature is need, and prevent the cantilever from being burned off.

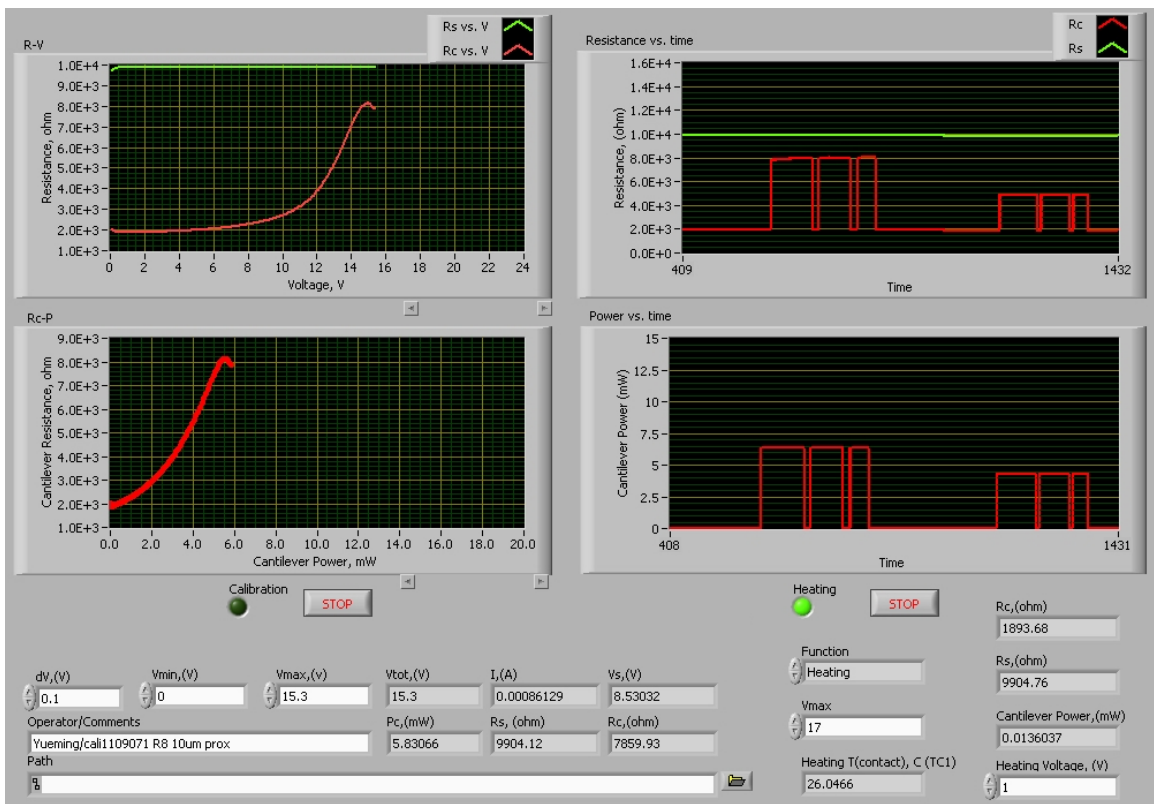


Figure 2-11. Interface of the LabView controlling software

2.3.3 Controlling Software

The heating circuit is controlled with a LabView VI developed by the author. Figure 2-11 shows a screen snapshot of the interface of the control VI. The control VI

consists of two main parts. The first part, which is located in the left side, is the calibration sections. This section is designed to obtain a resistance-heating voltage (R-V) curve and heating power-heating voltage (P-V) curve of the cantilever. To do this, the heating voltage applied to the cantilever is increased with a constant rate (e.g. 0.1V/sec) to a certain value. At the same time, the cantilever resistance and cantilever heating power are calculated and recorded. The data are plotted on the screen simultaneously. Also each data point is displayed in the numeric window underneath the plots.

The second section is the heating section. This section is designed for cantilever heating and monitoring during thermal writing. A constant heating voltage can be set in this section. The cantilever resistance, cantilever heating power, and sensor resistance are displayed in the numeric window simultaneously. Also, the plots of these data versus time are plotted in two graphic windows to give the operator a real-time view of the cantilever heating conditions.

Also the heating section has a burning protecting function. The maximum heating voltage can be set by the operator in the heating section. If the user type in a heating voltage higher than the maximum heating voltage accidentally, the output voltage will be the maximum heating voltage, instead of the value typed in by user. During experiment, the author found it is possible that some unexpected high heating voltage value can be accidentally typed in by mistake. This protecting function prevents the accidental burning off the cantilever by this kind of mistake.

2.4 Thermal Writing Operation

In this work, most thermal written pattern is less than 10 μm in the long dimension. Some of the pattern may have the long dimension up to 20 μm . Even for a 20

um feature, it is very hard to find it on a centimeter scale large sample without any reference under an optical microscope. For many of the pattern, the smallest dimension is less than 500 nm, which is over the resolution limit of the optical microscope on the AFM system. So it will be very difficult to re-identify the thermal writing area after taking out the thermally written sample to do some post thermal writing processes, and then put it back into the AFM again to image the same area. In order to help to re-find these small thermal written patterns after some processes, a specially designed substrate was used for sample preparation. A grid pattern with numbers on each direction was etched into the substrate.

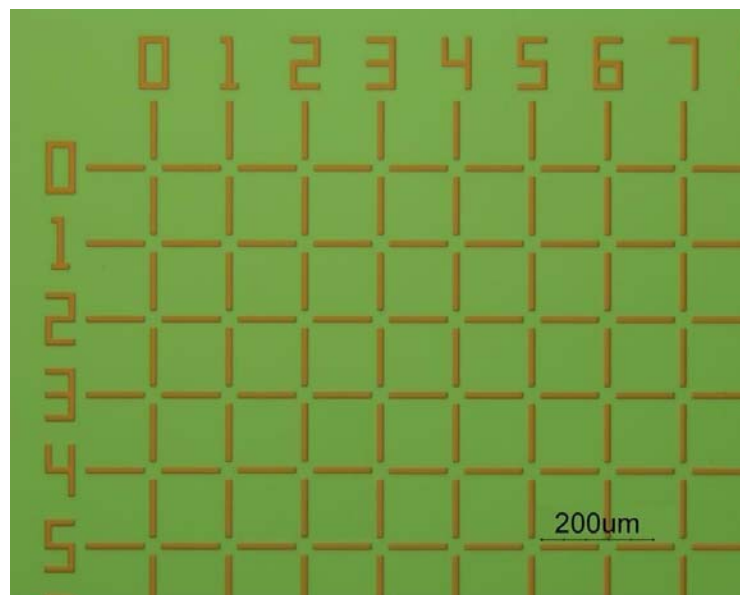


Figure 2-12. An optical microscope image of a sample substrate for AFM thermal writing experiment

Figure 2-12 show an optical microscope image of a sample grid. This grid contains two different sizes of areas for thermal writing. One is a 30um square area at the center of the cursor, and the other one is a 120 um square between the lines. After some

practice, a cantilever can be easily aligned to a thermal written area with an accuracy of ± 5 μm under the optical microscope on the AFM system. With a single large range coarse scan, the thermal written pattern can be easily identified. This grid can not only help to precisely locate the thermal written area, it also helps to intensely pack the thermal writing areas together. Hundreds of thermal writing experiments can be done on a single 5 mm square sample substrate. This is very useful especially when the amount of material is very limited.

After mounting a thermal cantilever on to the AFM scanner, and before thermal writing experiment, R-V and P-V curve of the thermal cantilever are first obtained using the calibration section of the controlling LabView VI. The purpose to do this is to check if the electrical connections are good, and if the cantilever is working properly. To make the measure consistent, normally the R-V and P-V curve are obtained when the cantilever is 10 μm above the substrate. To do this, the cantilever is first brought to engage with the substrate using automatic approach in the software. Then withdraw the cantilever 10 μm from the substrate. After this, run the calibration VI to obtain the R-V and P-V curves. If necessary, the R-V and PV curves when the cantilever is engaged with the substrate can also be easily obtained by the similar method.

If the cantilever performance and the electrical connection are both good, the next step is to run the thermal writing experiments. Most of the thermal writing experiments were done in a semi-automatic way. The AFM control software and the cantilever heating controlling LabView VI are installed on two different computers, and the only connection between these two computers is the operator. So the operator is the key for coordinating AFM scanning and the cantilever heating to make patterns. By this semi-automatic

method, usually only very simple patterns, like dots, lines, and squares, can be made in a single scan. In order to make more complex structures, multiple scans may need.

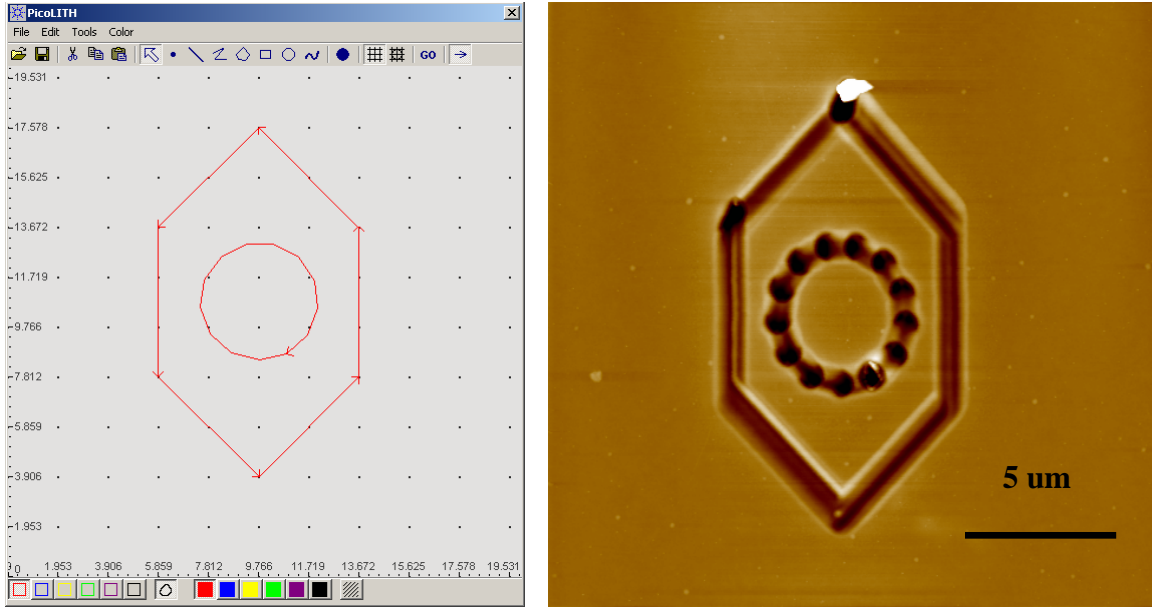


Figure 2-13. AFM topography image of a Benzene structure thermally written in a PMMA film with PicoLith software.

Lately, we upgraded the AFM controlling software with a lithographic function, PicoLith; and integrated the cantilever heating function into the software. Bias voltage (+/- 10V) from AFM controller can be used as the power source for cantilever heating. Six different colors can be used for designing the pattern in PicoLith. Each color represents a set of ThAFM parameters, including loading force, heating voltage, tip speed, and pause time. The PicoLith software is capable of drawing any arbitrary structures in a vector scan. Figure 2-13 shows a benzene structure designed in PicoLith software and the correspondent benzene structure thermally written in PMMA thin film with close loop enabled. We can see that the PicoLith can precisely draw a benzene ring structure according to the design in PicoLith. But we do see some limitations. For

example, even though a constant scan speed and a constant heating voltage was used for thermal writing a circle, which actually is a polygon in PicoLith; we observed that there is a deep dot between each line of the polygon. It seems that the tip dwelled for a while between each line of the polygon.

In spite of the minor limitation mentioned above, now the thermal writing tool is capable of thermal writing much more complex structures.

2.5 References

- [1] G. Binnig and C. Quate, Atomic force microscope, *Physical Review Letters*, 56 (1986) 930-933
- [2] Werner A. Hofer, Adam S. Foster, Alexander L. Shluger, Theories of scanning probe microscopes at the atomic scale, *REVIEWS OF MODERN PHYSICS*, (2003) 75 (4): 1287-1331
- [3] Martin, Y.; Williams, C. C.; Wickramasinghe, H. K. T. J. Watson, Atomic force microscope-force mapping and profiling on a sub 100-Å scale, *Journal of Applied Physics* (1987), 61(10), 4723-9
- [4] S. Morita, R. Wiesendanger, E. Meyer, *Noncontact Atomic Force Microscopy*, Springer (2002)
- [5] Magonov, S. N.; Elings, V.; Whangbo, M.-H., Phase imaging and stiffness in tapping-mode atomic force microscopy, *Surface Science* (1997), 375(2/3), L385-L391
- [6] Tanya L. Wright, PhD thesis, "Fabrication and Testing of Heated Atomic Force Microscope Cantilevers", Georgia Institute of Technology, 2005
- [7] P. Vettiger, G. Cross, M. Despont, U. Drechsler, U. Durig, B. Gotsman, W. Haberle, M. Lantz, H. Rothuizen, R. Stutz and G. Binnig, The "millipede" - nanotechnology entering data storage, *IEEE Transactions on Nanotechnology*, 1 (2002) 39-55.
- [8] Nelson, B. A.; King, W. P.; Laracuente, A. R.; Sheehan, P. E.; Whitman, L. J. Direct deposition of continuous metal nanostructures by thermal dip-pen

- nanolithography. *Applied Physics Letters* (2006), 88(3), 033104/1-033104/3
- [9] King, W. P.; Saxena, S.; Nelson, B. A.; Pitchimani, R.; Weeks, B. L., Nanoscale thermal analysis of an energetic material, *Nano Letters* (2006), 6(9), 2145-2149
- [10] G. Binnig, M. Despont, U. Drechsler, W. Haberle, M. Lutwyche, P. Vettiger, H. J. Mamin, B. W. Chui and T. W. Kenny, Ultrahigh-density atomic force microscopy data storage with erase capability, *Applied Physics Letters*, 74 (1999) 1329-1331.
- [11] Chui, B. W.; Stowe, T. D.; Ju, Y. S.; Goodson, K. E.; Kenny, T. W.; Mamin, H. J.; Terris, B. D.; Ried, R. P. Low-stiffness silicon cantilevers with integrated heaters and piezoresistive sensors for high-density AFM thermomechanical data storage, *Journal of Microelectromechanical Systems* 1998, 7, 69-78.
- [12] King, W. P.; Kenny, T. W.; Goodson, K. E.; Cross, G. L. W.; Despont, M.; Durig, U.; Rothuizen, H.; Binnig, G.; Vettiger, P., Atomic force microscope cantilevers for combined thermomechanical data writing and reading,. *Applied Physics Letters* 2001, 78, (9), 1300-1302.
- [13] Markiewicz, Peter; Goh, M. Cynthia, Atomic force microscopy probe tip visualization and improvement of images using a simple deconvolution procedure, *Langmuir* (1994), 10(1), 5-7
- [14] Markiewicz, Peter; Goh, M. Cynthia, Atomic force microscope tip deconvolution using calibration arrays, *Review of Scientific Instruments* (1995), 66(5), 3186-90
- [15] Sunden, E. O.; Wright, T. L.; Lee, J.; Graham, S. A.; King, W. P., Roomtemperature chemical vapor deposition and mass detection on a heated atomic force microscope cantilever. *Applied Physics Letters* 2006, 88, 033107.
- [16] Cappella, B.; Dietler, G. Institut de Physique de la Matiere Condersee, Universite de Lausanne, Lausanne, Switz., Force-distance curves by atomic force microscopy, *Surface Science Reports* (1999), 34(1-3), 1-104
- [17] Cleveland, J. P.; Manne, S.; Bocek, D.; Hansma, P. K. A nondestructive method for determining the spring constant of cantilevers for scanning force microscopy. *Review of Scientific Instruments* (1993), 64(2), 403-5
- [18] Hutter, Jeffrey L.; Bechhoefer, John. Calibration of atomic-force microscope tips. *Review of Scientific Instruments* (1993), 64(7), 1868-73
- [19] Christopher T Gibson, Gregory S Watson and Sverre Myhra, Determination of the spring constants of probes for force microscopy/spectroscopy, *Nanotechnology* 7

(1996) 259–262.

- [20] William P. King, Thomas W. Kenny, Member, Graham L. W. Cross, Michel Despont, Urs T. Dürig, Hugo Rothuizen, Gerd Binnig, and Peter Vettiger, Design of Atomic Force Microscope Cantilevers for Combined Thermomechanical Writing and Thermal Reading in Array Operation, *Journal of Microelectromechanical Systems*, (2002) 11(6):765-773

CHAPTER 3

THERMAL WRITING ON POLYMERS USING DECOMPOSITION

3.1 Introduction and Background of Sacrificial Polymers

One of the possible ways to thermally pattern a material is to locally decompose a thin polymer film using the heated cantilever tip. It has been shown by Wilson and coworkers,[1,2] Kohl and coworkers,[3] and Henderson and coworkers,[4,5] that clean micro-patterned structures can be formed using polymers which can be cleanly decomposed thermally using a variety of methods. This previous work has demonstrated that both the polynorbornene (PNB) and polycarbonate (PC) families of polymers can be utilized to produce polymers which cleanly thermally decompose at moderate temperatures. Polynorbornenes have relatively high decomposition temperatures in the range of 425 °C which can make their use in sacrificial microstructure fabrication processes advantageous. However, for the purposes of thermal AFM patterning, this high decomposition temperature requires the probe to be operated at very high temperatures. Temperatures in excess of 700 °C would be required to decompose the material by a heated AFM probe with an acceptable writing speed. This shortens the lifetime of the cantilevers and makes continuous or fast thermal writing more challenging. Furthermore, early writing experiments with polynorbornenes showed that the polymers were extremely soft and tacky when heated which presented problems with adhesion of the cantilever to the PNB surface and deformation of the polymer surface in areas surrounding the written patterns. Therefore, the focus of this research work on thermally sacrificial polymers is on the use of polycarbonates as thermally imageable films.

Linear tertiary copolycarbonates were originally investigated as thermally depolymerizable polymers by Wilson and coworkers and were utilized as the basis for developing “dry developing” photoresists.[1] For example, the copolycarbonate of 2,5-dimethyl-2,5-hexanediol and p-benzenedimethanol is stable up to 200 °C, and then undergoes rapid thermolysis with formation of carbon dioxide, p-benzenedimethanol, and dienes corresponding to the dehydration products of 2,5-dimethyl-2,5-hexanediol. Other polycarbonates containing allylic or benzylic group have also been investigated as thermally depolymerizable polymers and the acid catalyzed decomposition of such systems was reported as a means to produce photodefinable materials. The thermal degradation temperature of the copolycarbonate depends strongly on the structures of the diols used in the synthesis of the polymers. Yves and coworkers [6] reported that the degradation temperature of copolycarbonates of p-benzenedimethanol with 2,5-dimethyl-2,5-hexanediol, 2,5-hexanediol, and 1,4-butanediol are 200 °C, 300 °C and 340 °C, respectively. More recently, White and coworkers [7,8] have reported additional copolycarbonates that display improved imaging performance using acidolysis mechanisms. Due to their relatively low decomposition temperatures and extremely clean decomposition, these polycarbonate structures developed by White and coworkers were utilized for the experiments on thermally sacrificial polymer imaging using heated AFM cantilever probes. The polycarbonate IV polymer used in this work is slightly different from the one developed by White and coworker. The polymer structure is modified by adding vinyl groups to both end of the polymer chain to make it cross-linkable. Besides polycarbonate IV, polycarbonate V developed by White and coworkers, and a

commercial available polycarbonate, poly (propylene carbonate) (PPC) were used in this work.

3.2 Material Synthesis and Characterization

3.2.1 Material Synthesis

Copolycarbonate oligomers were synthesized by using a solid-liquid phase-transfer-catalyzed polycondensation of the bis (carbonylimidazolid) of 2, 5-hexanediol with 5-norborene-2-exo, 3-exo-dimethanol. Figure 3-1 shows the synthesis procedures used for making these materials. By controlling the ratio of monomers, the molecular weight can be controlled. The oligomer was then end capped with methacryloyl chloride to make it cross-linkable.

3.2.1.1 Synthesis of the bis (imidazole carboxylate) of 2,5-hexanediol

To a solution of 8.863 g (75 mmol) of 2, 5-hexane diol (Sigma-Aldrich) in 85 ml dry THF, 0.28 g (7.16 mmol) of potassium metal was added under N₂ atmosphere. After refluxing this solution until all of the potassium had dissolved, the solution was transferred to a solution of 26.775 g (165 mmol) carbonyl diimidazole in 85 ml dry THF. The stirred reaction was refluxed for 90 minutes. After cooling to room temperature, the reaction mixture was concentrated to approximately 80 ml using a rotary evaporator. 150 ml of ethyl acetate was added and the organic solution was washed twice with 40 ml 5% HCl solution and three times with distilled water (50 ml for each wash). The organic layer was dried over magnesium sulfate, filtered, and the solvent was removed using a rotary evaporator. The white solid product was then recrystallized using ethyl acetate and

hexane (1:1 volume mixture). The purified product was obtained in a 26.7% yield (6.14 g) and confirmed as the desired product by $^1\text{H-NMR}$.

3.2.1.2 Synthesis of copolycarbonate oligomer

A mixture of 5-norborene-2-exo, 3-exo-dimethanol (0.988 g, 6.4 mmol) (Sigma-Aldrich), the bis(imidazole carboxylate) of 2,5-hexanediol (1.839 g, 6.0 mmol), a catalytic amount of 18-crown-6 (0.15 g), 20 ml of dry dichloromethane, and an excess of K_2CO_3 (3.4 g) was prepared under N_2 atmosphere. The reaction was stirred and refluxed at 40°C for 18 hours. Solids were filtered away. The filtrate was diluted with 50 ml CH_2Cl_2 . The solution was washed twice with 50 ml 5% HCl solution and three times with distilled water (50 ml for each wash). The organic layer was dried with magnesium sulfate, filtered; solvent is removed on a rotary evaporator followed by vacuum dry at 0.5 mtorr for 6 hours. And get 1.52 g solid (78% yield).

3.2.1.3 Synthesis of end capped copolycarbonate oligomer

0.327g (3.15 mmol) methacryloyl chloride (Alfa Aesar) was slowly added to a solution of 1.20 g copolycarbonate oligomer and 0.390 g (3.86 mmol) triethylamine (Sigma-Aldrich) in 25 ml methylene chloride at 0°C . The solution was stirred at this temperature for 15 minutes and then allowed to rise slowly to room temperature, at which it was stirred for an additional 3 hours. 100 ml of methylene chloride was then added and the solution was washed twice with 50 ml 5% HCl followed by two DI water wash. The organic layer was dried with magnesium sulfate and then the solvent was removed using

a rotary evaporator followed by vacuum drying at 0.5 mtorr for 6 hours. The final product was 0.66 g of the end-capped copolycarbonate oligomer.

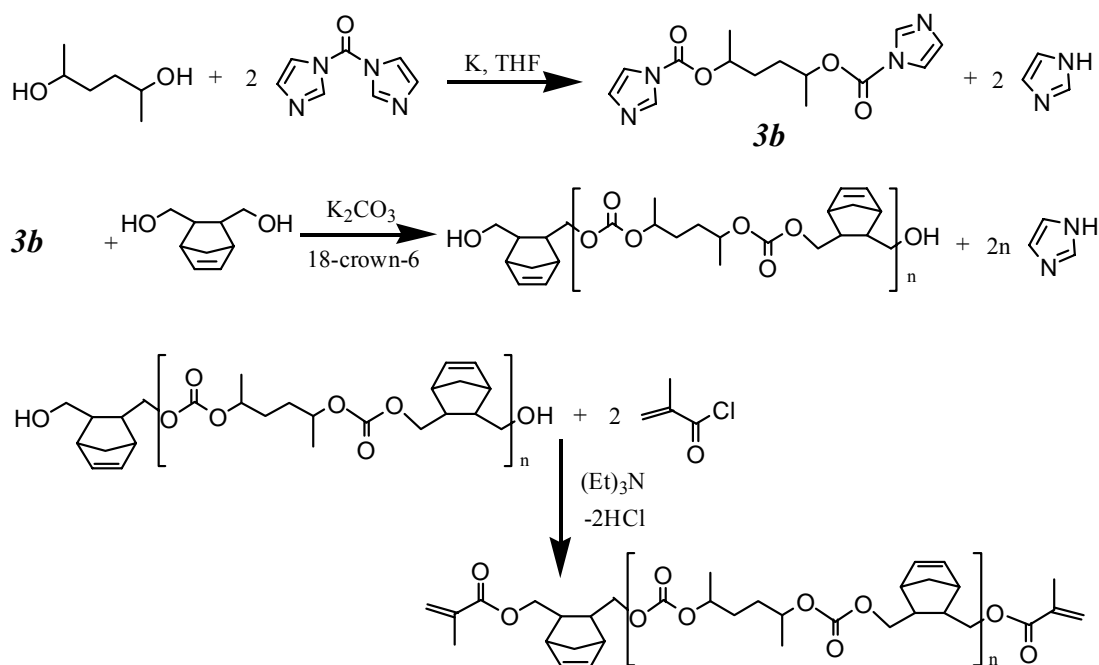


Figure 3-1. Synthetic route used to prepare cross-linkable co-polycarbonates.

3.2.2 Material Characterization

3.2.2.1 H-NMR Characterization

The polymer structures were checked by proton nuclear magnetic resonance (1H -NMR) using a Varian Mercury VX 400 instrument. Figure 3-2 shows an example of the proton NMR spectra for one of the cross-linkable polycarbonates. The assignments of the 1H -NMR spectrum are almost the same as those described in literature, except for some small peaks which appear in the spectra ($\delta = 3.785$ and 3.562 ppm in spectrum A, and $\delta = 6.118$, 6.070 , 5.574 , 5.528 ppm in spectrum B). These peaks belong to the end groups of the oligomers, and the changes in these peaks are evidence of successful end-capping reaction.

The spectra show that there are measurable peaks for the end groups. Because the integrations of the peaks in $^1\text{H-NMR}$ are proportional to the number of proton, we can use the $^1\text{H-NMR}$ to determine the number average molecular weight of the oligomers by end group analysis. [9]

In spectrum A, peak #10 and #11 belong to the different end groups of the oligomer before end-capping. There are two possible types of end groups for the original oligomer: (1) a norbornene alcohol group or (2) a hexane alcohol group. It is further assumed that the protons represented by peaks #10 and #11 can be assigned to the 2 methylene hydrogens of the $-\text{CH}_2\text{-OH}$ group in the norbornene alcohol for peak #10 and the one methylene hydrogen of the $-\text{CH}(\text{CH}_3)\text{-OH}$ group in the hexane alcohol functional group for peak #11. The integrated area of peak #10 should thus be proportional to two times the number of norbornene alcohol end groups in solution while the integrated area of peak #11 should be proportional to the number of hexyl alcohol end groups in the polymer. Since peak #1 is reasonably well isolated, its integrated area should be proportional to two times the total number of norbornene groups in the polymer. Likewise, peak #7 is reasonably well isolated and its integrated area should be proportional to four times the total number of hexane diol derived repeat units in the polymer.

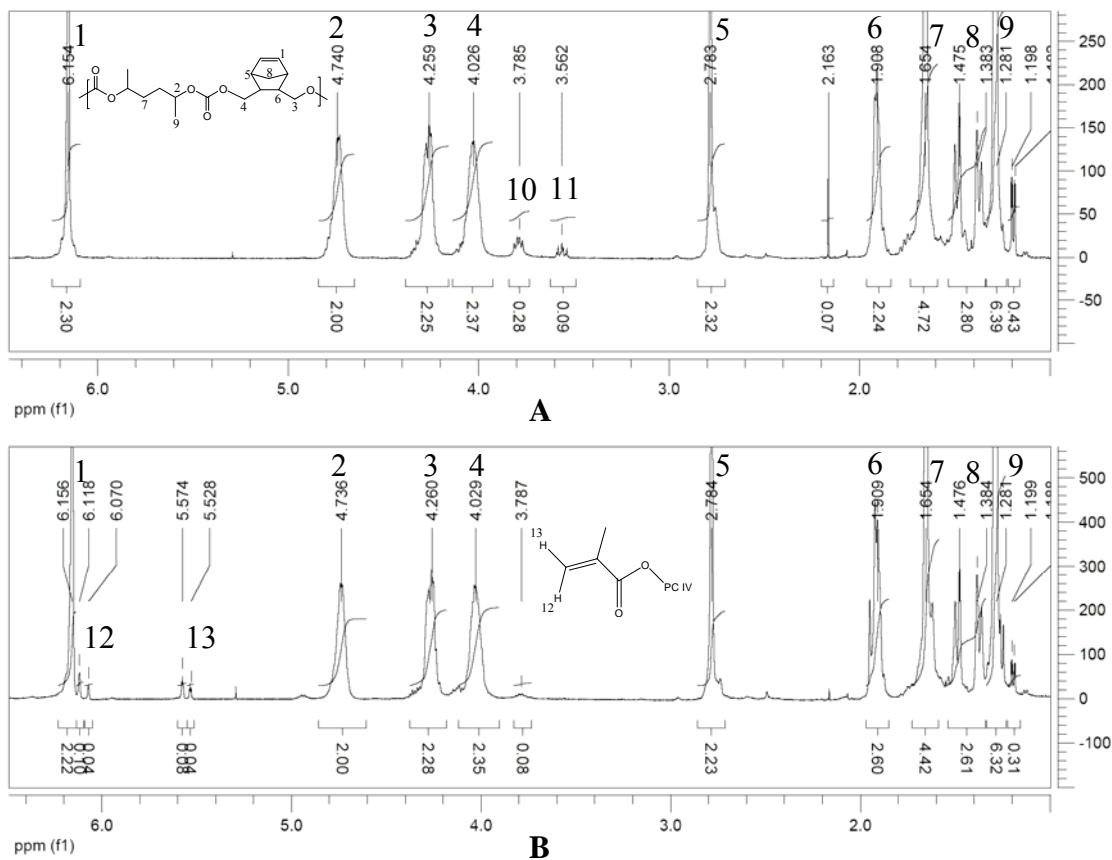


Figure 3-2. $^1\text{H-NMR}$ of copolycarbonate oligomer (CDCl_3): A, before end capping; B, after end-capping with methacryloyl chloride.

Since each molecule has two end groups, the average number of monomers (regardless of whether they are derived from the norbornene diol or hexane diol) in the oligomers can be calculated as:

$$\text{Average number of monomer units in oligomer} = \frac{(\text{area of peak \#7})/4 + (\text{area of peak \#1})/2}{((\text{area of peak \#10})/2 + (\text{area of peak \#11}))/2}$$

In the polycarbonate copolymer, which is by definition strictly alternating using the synthesis method used in this work, one can treat the polymer repeat unit as a combined norbornene and hexyl functional group as shown in Figure 3-1. Therefore, one can also simply calculate the average degree of polymerization in these terms by dividing the number of monomer units in the oligomers by 2.

$$x_n = \left(\frac{(\text{area of peak \#7})/4 + (\text{area of peak \#1})/2}{((\text{area of peak \#10})/2 + (\text{area of peak \#11})/2)} \right) / 2 \quad (3-1)$$

In the case of the spectra shown in Figure 3-2, the average degree of polymerization can be calculated as $x_n = \{(4.72/4+2.30/2)/[(0.28/2+0.09)/2]\}/2 = 10$. Therefore, the number average molecular weight of the oligomer should be approximately $M_n = 3,200$ g/mol.

3.2.2.2 Thermal Analysis of End-Capped Polymers

The end-capped copolycarbonate oligomers can be cross-linked thermally by using 2, 2'-Azobisisobutyronitrile (AIBN) as a free radical initiator. The typical amount of AIBN used in the preliminary work is approximately 5 wt% initiator with respect to oligomer mass. The oligomers containing AIBN were cured at 80 °C for 12 hour in a nitrogen environment. The thermal properties of the resulting cross-linked oligomers were measured by DSC and TGA.

DSC scans of three different samples were collected using a Seiko DSC 220C instrument with a heating/cooling rate of 10 °C/min with N₂ purge. The DSC data showing heat flow versus temperature for these samples are shown in Figure 3-3.

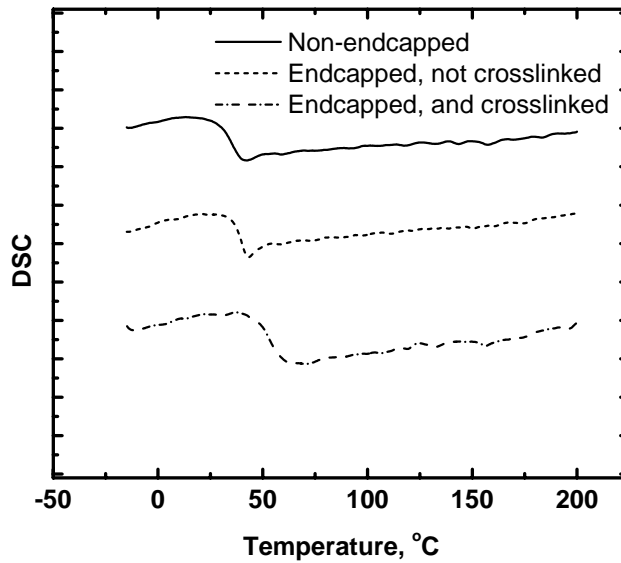


Figure 3-3. DSC curves of copolycarbonate oligomers, (N₂, 10 C/min)

The glass transition temperature (T_g) of each sample was determined from the second heating cycle. The T_g of the oligomer before end-capping, uncured but endcapped oligomer, and cured endcapped oligomer are 35.2 °C, 39.7 °C, and 53.3 °C, respectively. This clearly shows that crosslinked the polymer does indeed slightly increase the T_g of the polycarbonate.

Bicerano [10] has presented an equation correlating the dependence of glass transition temperature on crosslink density of randomly crosslinked polymers.

$$T_g(n) \approx T_g(\infty) \cdot \left[1 + \frac{c}{(n \cdot N_{rot})} \right] \quad (3-2)$$

Here $T_g(n)$ is the glass transition temperature of crosslinked polymer (units in K), $T_g(\infty)$ is the glass transition temperature before crosslinking (units in K), n is average number of repeat units between two crosslinks, N_{rot} is the average number of rotational

degrees of freedom per repeat unit, and c is a constant. Bicerano reported that $c \approx 5 \pm 2$. The T_g of polycarbonate IV was measured as 35.2°C . The calculated N_{rot} for polycarbonate IV is 15. Choosing $c = 5$, the calculated glass transition temperature for $n = 11$ results in a calculated glass transition temperature after crosslinking of $T_g(10) = 46^\circ\text{C}$. This is in reasonable agreement with the measured value of 53.3°C . While such a small increase in T_g may not appear to be significant enough to improve the thermal deformation performance of the polymer, the T_g is only one indicator of polymer thermal properties. If the polymer is crosslinked to form a complete network, it should be extremely resistant to thermal flow even with such a low glass transition temperature.

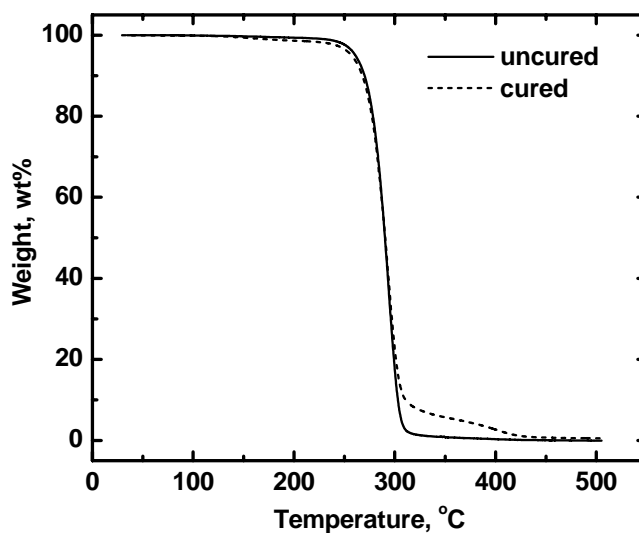


Figure 3-4. TGA data for uncured and cured end-capped co-polycarbonate oligomers.

Figure 3-4 shows a thermogravimetric analysis (TGA) data for the polycarbonate IV both with and without addition of the radical initiator and subsequent cross-linked at 80°C . TGA analysis was performed using a TA Instruments Q500 TGA using a $10^\circ\text{C}/\text{min}$ heating rate. The decomposition temperature of the pure polymer without cross-

linking is observed to be 290 °C (50% weight loss) and the polymer is observed to undergo clean single-step decomposition with no observable residue. After cross-linking, the onset of thermal decomposition of the cross-linked polymer is observed to be essentially the same as the polymer before cross-linking. However, decomposition of the cross-linked polymer exhibits a low residual weight tail (beginning at approximately 8.0 wt %) that does not completely disappear until a temperature of approximately 430 °C. This residual mass that remains at higher temperatures is a result of the methacrylate polymer cross-links, which are formed in the polycarbonate, but even this material can be decomposed cleanly at slightly higher temperatures than the uncross-linked material.

3.3 Thermal Writing Experiments and Results: PPC, PC-V, CPC-IV

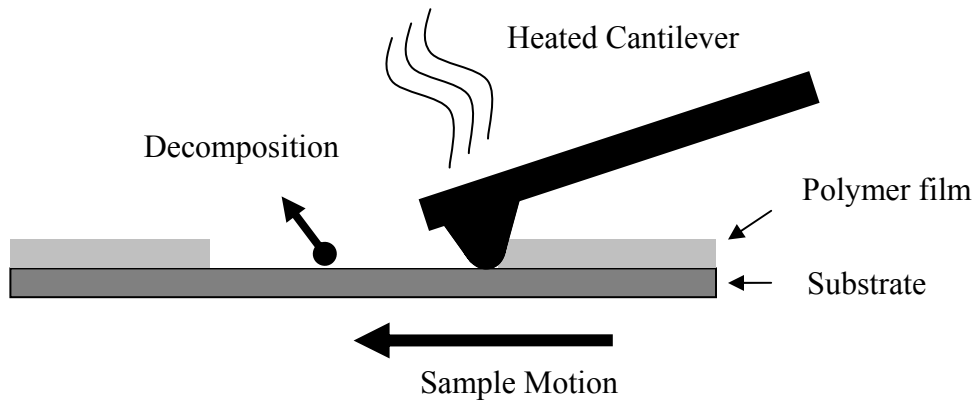


Figure 3-5. Process for using thermally sacrificial polymers for direct nanoscale thermal patterning using the AFM probe tip.

Figure 3-5 shows the main principle of the how the probe nanolithography method works. A heated AFM probe scans across a polymer thin film surface. In the heated area by the cantilever, polymer is decomposed and the decomposition products are evaporated, and leave the pattern behind.

The thermal writing experiments reported here were performed using heated AFM cantilevers obtained from Dr. King in University of Illinois at Urbana-Champaign (UIUC). The cantilevers were made of doped single-crystal silicon, with high doping in the cantilever legs and low doping near the cantilever tip. When electrical current passes through the cantilever, resistive heating occurs in the low-doped highly resistive region near the cantilever tip. The cantilevers have a very high temperature coefficient of electrical resistance that can be used to calibrate the cantilever temperature. The cantilever spring constant was 0.35 N/m and the tip radius of curvature was estimated to be 30 nm. When the unheated tip was scanned in hard contact with the polymer film, no deformation of the polymer was observed. For the writing experiments, the tip-substrate load force was approximately 10 nN. Based on the cantilever load force, the tip sharpness, the estimated tip radius of curvature, and previous thermal simulations, the temperature at the tip-substrate interface was estimated to be 100 degree below the heater temperature [11,12]. Basic lithographic patterns of arrays of lines and squares were fabricated as a demonstration of the technique. When writing was complete, the thermal cantilever was disengaged from the sample and the power was turned off. After waiting approximately one minute, the lithographic site was imaged using the same thermal cantilever operated at room temperature.

3.3.1 Patterning of Polycarbonate Films Using a Heated Cantilever Probe Tip

The first attempts at using a heated AFM cantilever probe tip to pattern polymer films focused on using poly (propylene carbonate). Figure 3-6 shows an example of an AFM topographic image of a PPC film after patterning using a heated probe tip. It is

observed that although some decomposition has taken place and patterns have been formed, significant polymer deformation and flow have occurred. The polymer was observed to “stick” to the tip and make tip removal from the surface difficult and result in displacement and deposition of polymer in undesired areas during tip scanning. Therefore, one of the motivations of the work proposed here is to create thermally sacrificial polymers which can overcome these difficulties. These problems with PPC are a result of the low T_g and low molecular weight of the PPC polymer which allows the polymer to melt and flow when heated by the tip. Thus, several strategies for overcoming this problem are being explored in this work.

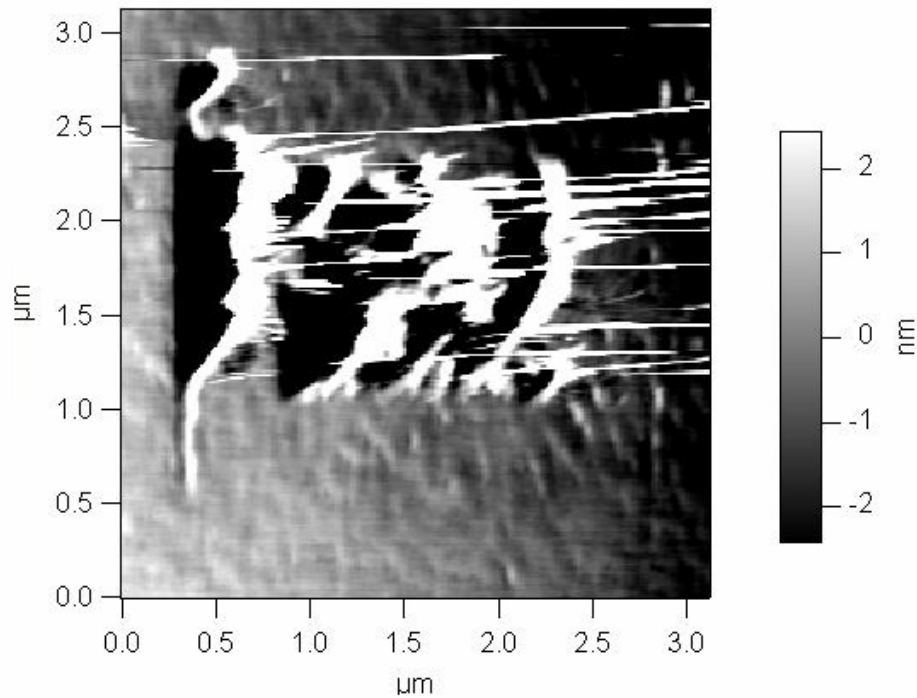


Figure 3-7: Example of AFM images of poly(propylene carbonate) film patterned using a heated AFM tip. It is clear that significant polymer deformation and flow occurred. The polymer also appeared to be “sticky” and made movement and removal of the AFM tip difficult.

3.3.2 Patterning of Polycarbonate Films with Improved Resistance to Thermal Flow Using a Heated Cantilever Probe Tip

A series of thermally sacrificial polymers with improved resistance to thermal flow as compared to PPC were previously developed and characterized by White and coworkers. Examples of the structures of two of these polymers are shown in Figure 3-7. Due to earlier optical patterning results which showed minimal thermal flow of these materials during thermal processing, these materials were synthesized and characterized for use in the AFM heated probe writing experiments.

Overall, use of these copolycarbonates demonstrated improved patterning results using the heated AFM probe tip as compared to experiments using PPC (see Figure 3-8). However, Polymer V is a semi-crystalline material due to its linear nature and reasonably symmetric structure. This semi-crystalline nature of Polymer V results in a high softening temperature for the polymer but also results in large scale surface roughness in thin films induced by the size of the large rigid crystalline domains. Polymer V showed very good AFM writing with respect to thermal deformation by the tip of the resulting pattern, but the large film surface topography and small domain size of the crystalline regions of this material severely limit the overall writing process. Polymer IV which possesses a higher T_g than PPC showed some improvement in writing performance but still demonstrated slow writing and a limited temperature processing window which resulted in patterning without thermal deformation. Therefore, it was decided to investigate cross-linked polycarbonates as a writing media which could show improved thermal performance.

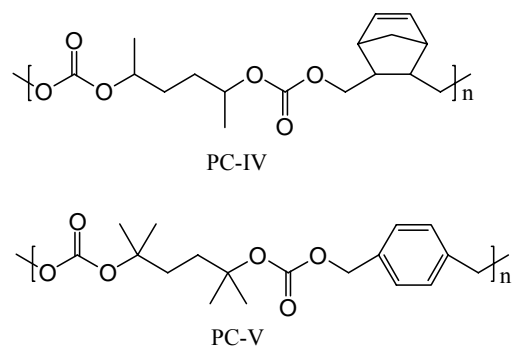


Figure 3-7. Example of copolycarbonates that have been used as thermally sacrificial polymers in this work.

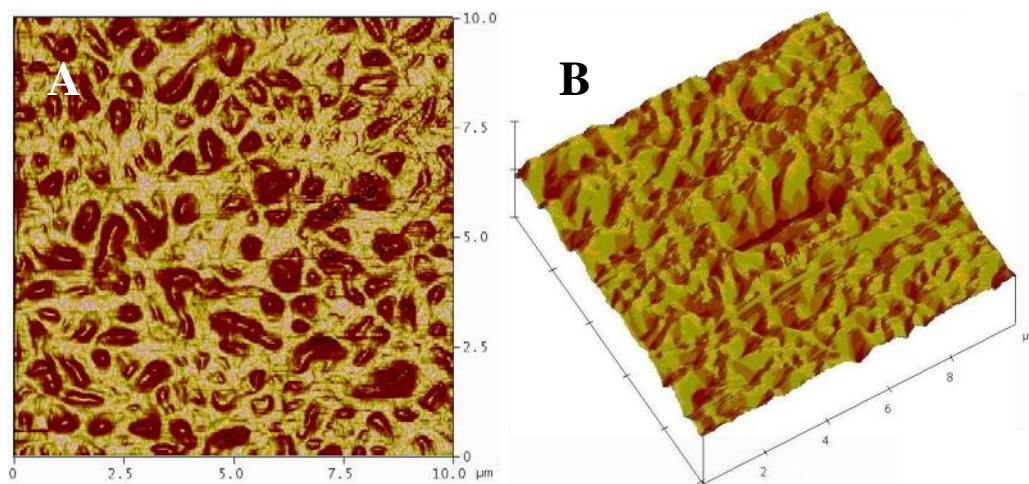


Figure 3-8. (A) AFM topographic scan of surface of Polymer V which shows relatively large topography due to the semi-crystalline nature of the polymer. (B) Example of AFM image of pattern formed in Polymer V.

3.3.3 Thermal AFM Writing Experiments With the End-Capped Polycarbonates [13]

According to the previous results, we know we need some material that should have improved resistance to thermal flowing to get better resolution. But also we need the material to be amorphous to prepare a uniform polymer thin film with smooth surface. The best way achieve these two goals at the same time is using cross-linked amorphous

sacrificial polymers. For this purpose, the cross-linked polycarbonate IV (CPC-IV) was synthesized.

In this work, polymer thin films were prepared using solutions containing 5.0 wt % cross-linkable PC-IV, 0.2 wt % AIBN radical initiator, and 94.8 wt % PGMEA solvent. Films were spin cast at 2000 rpm for 30 s using a CEE Model 100CB spin coat and a bake tool. After spin casting, the polymer thin film was put into a convection oven, the oven was purged with N₂ for 30 min the oven and the film were heated to 80 °C under N₂, and the film was maintained at 80 °C for 12 h to promote the extensive crosslinking of the polymer film. Exclusion of ambient oxygen is important in these radically cross-linked thin films, since the presence of oxygen results in fast quenching of the thermally generated radicals and therefore prevents the significant cross-linking of the polymer chains. Polymer film thicknesses were measured using an M-2000 Variable Angle Spectroscopic Ellipsometer (VASE, J.A. Woollam). Film thicknesses in the range of 100 nm to 150 nm were used for thermal writing experiments.

The thermal properties of the film and the substrate are important in determining how the tip scanning motion at a particular tip temperature and speed are translated into the decomposition pattern in the polymer film. In other words, it is the temperature profile setup in the polymer film and the substrate as the tip scans over the surface that determine the size and shape of the decomposed region in the polymer film. Previous publications have provided a detailed analysis of the heat transfer mechanisms within the silicon heater cantilever [14] and in the polymer near the heated tip. [15] In general, there are a set of thermal properties of the substrate and film that should give the highest patterning resolution at the fastest possible speed for a given power input to the cantilever

tip. First, the substrate ideally would be sufficiently thermally conducting; such that the temperatures at the tip-polymer interface is significantly higher than the polymer directly beneath the cantilever beam but away from the tip. It is also, however, advantageous if the substrate is sufficiently thermally insulating, such that the polymer in contact with the tip is heated rapidly to a sufficiently high temperature that exceeds the decomposition temperature of the polymer. In the case of the film writing media (e.g., in this case the polymer), lower film thermal conductivities will result in steeper thermal gradients in the film, which should translate into finer lateral resolutions. However, as the film thermal conductivity is decreased, the temperature gradient into the depth of the film also increases, which translates into lower writing speeds or higher required powers for a given scanning speed. Therefore, for the experiments presented in this work, the polymer film was prepared on a silicon wafer that had been coated with a 600-nm-thick layer of silicon dioxide to provide a uniform surface of constant thermal properties. Heat transfer models previously developed by the authors indicate that in this configuration, the temperature difference between the cantilever tip and the cantilever heater platform (i.e., where the heat is generated) is approximately 100 °C. [16]

Figures 3-9 and 3-10 show the results of thermal AFM writing experiments. Figure 3-9 shows a 3 μm square formed in a 125-nm-thick cross-linked polycarbonate-IV film using multiple adjacent scans of the heated cantilever, where the cantilever heater temperature was maintained at 580 °C and the tip was scanned at 1.0 Hz. Figure 3-10 shows an array of lines formed in a 125-nm-thick cross-linked polycarbonate film that were written with isolated single line scans of the heated cantilever tip that were 6 μm

long and separated laterally by 1 μm using a cantilever heater temperature of 720 $^{\circ}\text{C}$ and tip scanning speed of 0.5 Hz.

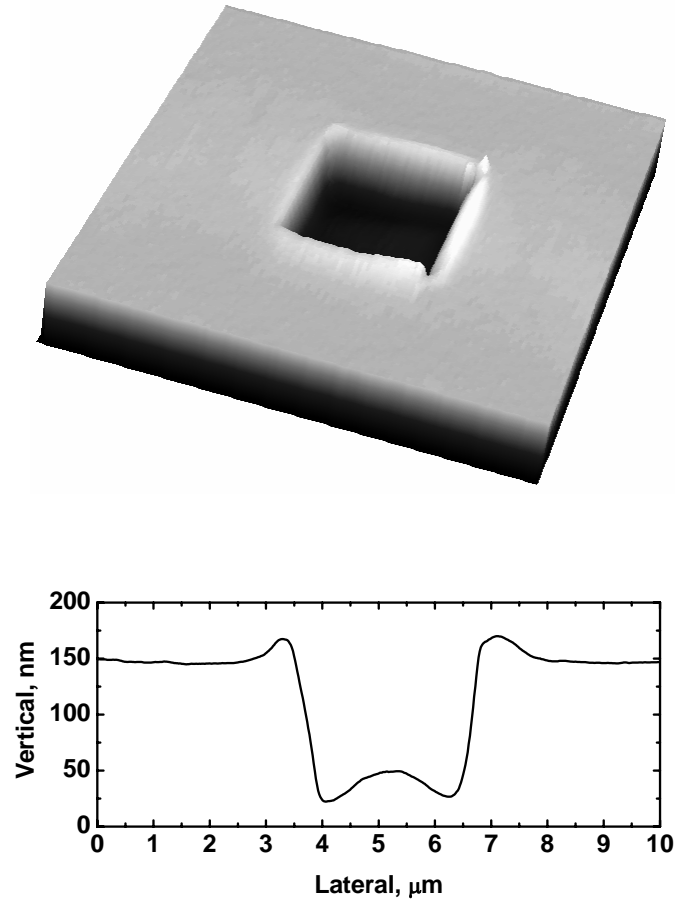


Figure 3-9. A thermal written square in cross-linked PC-IV polymer thin film

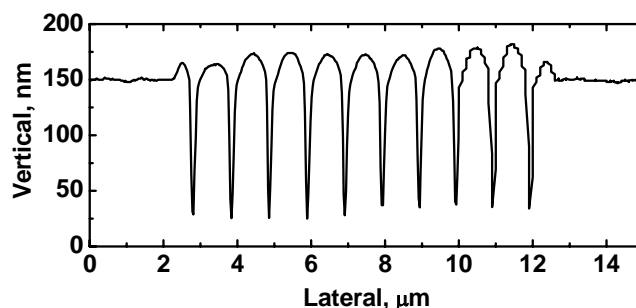
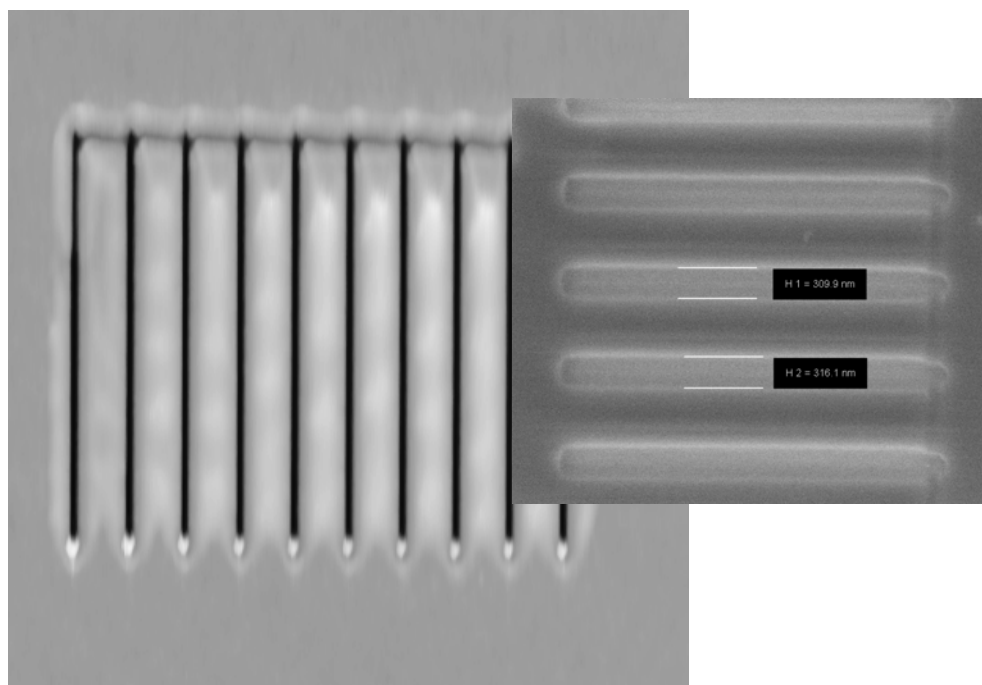


Figure 3-10. Thermal written lines in cross-linked PC-IV polymer thin film

Overall, the polymer appears to be almost completely removed in the regions where the tip has scanned. While a small amount of residue can be seen in the written square, the height of the decomposed region is equal to the original polymer thickness, and there is the little pileup characteristic of plastic or thermoplastic deformation.[17] In contrast, attempts at writing on polycarbonate thin films that were not cross-linked, such as polypropylene carbonate (PPC), showed the significant deformation of the polymer film in the vicinity of the written area due to the low glass transition temperatures of the

polymers relative to their decomposition temperatures. The polymer in the region near the tip would be essentially melted and be displaced by the tip movement, resulting in patterning by the thermal flow of the material without significant decomposition. These polycarbonates that were not cross-linked also presented problems with the tip sticking to the surface if it was cooled while in contact with the surface. The use of cross-linked materials such as the polycarbonates presented in this work can alleviate these issues.

Because of its ability to cleanly decompose to volatile products, there may become concern about the utility of thermally sacrificial polymers, such as the polycarbonate presented in this work, for use in other traditional microfabrication processes such as plasma etching. In general, in most cases lithographic patterning is followed by plasma etching to transfer the pattern formed in the imaging layer to some underlying substrate films. Therefore, to demonstrate the usefulness of such patterned thermally sacrificial polymers, the etch behavior of the polycarbonate used in this work was compared to several other standard lithographic polymers. The three materials compared in this work were: 1. novolac _Alnovol SPN400, Clariant_, which is a representative model of the basic resin polymer used for I-line and G-line photoresists; 2. oly_hydroxystyrene__PHOST, Mw=11,800, TriQuest, which is a model resin for 248-nm photoresist materials, and 3. the crosslinked polycarbonate. The polymer thin films were prepared by spin coating from polymer solutions on silicon wafers using a CEE 100 spinner. The novolac and PHOST samples were softbaked at 110 °C for 5 min after casting to remove residual casting solvent. The polycarbonate sample was cured with the procedures mentioned previously. These three samples were etched in halogenated plasma that is typical of the conditions used to etch silicon dioxide. The three polymer

samples were loaded into the plasma chamber (Plasma-Therm ICP) along with an SiO₂ film sample (made via wet thermal oxidation) and etched using a gas mixture of CF₄ (flow rate of 20.0 sccm) and H₂ (flow rate of 2.0 sccm) at a total RF power of 100 W. The film thicknesses before and after the plasma etching were measured via profilometry (KLA P15 profilometer). The resulting etching rates were measured to be: 131 nm/min for SiO₂, 60 nm/min for novolac, 236 nm/min for PHOST, and 180 nm/min for the cross-linked polycarbonate. Therefore, it is clear that the etch performance can be comparable to that of other current generations of lithographic polymers. This should not be surprising, since the thermal decomposition temperature of the pure polycarbonate is still quite high and is in a range similar to that of many of the other polymers currently used for lithography. The critical difference is that the polycarbonate materials undergo a very clean thermal decomposition without leaving significant residues, unlike other polymers such as novolac or PHOST.

The nanoscale decomposition of thin polymer films represents advancement for scanning-probe-based lithography. While previous experiments with heated AFM cantilevers showed that nanoscale writing could be turned on and off with the heating of the cantilever, the writing was additive only. This work presents subtractive nanoscale lithography. This technique is highly scalable. Heated AFM cantilevers can operate into the MHz range [18] and can be made and operated in large arrays having more than 4000 cantilevers. It should be possible to write 10-nm pixels into a 300-mm wafer in 2 to 4 h.

3.4 Effect of Crosslinking

The experiment results in previous section show that cross-linking can improve the performance of the polymer for thermal probe lithography. But TGA data also show

that cross-linking may also introduce decomposition residue, which is not desired for the thermal probe lithography. In this section, the author will investigate the effect of cross-linking on the performance of the polymer for thermal probe lithography in detail.

3.4.1 Material synthesis and characterization

Poly (hydroxyl styrene) (PHOST) based polymer and co-polymers were used as the writing materials. The PHOST based co-polymer was synthesized by protecting the phenol group of PHOST with allyloxycarbonyl (AOC) and ethyloxycarbonyl (EOC) groups using allyl chloroformate (Aldrich) and ethyl chloroformate (Alfa Aesar), respectively.

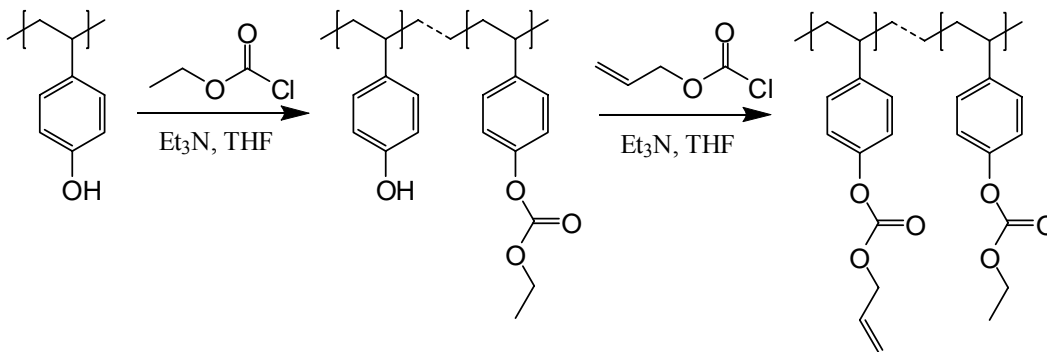


Figure 3-11. Synthetic route for make cross-linkable PHOST co-polymer

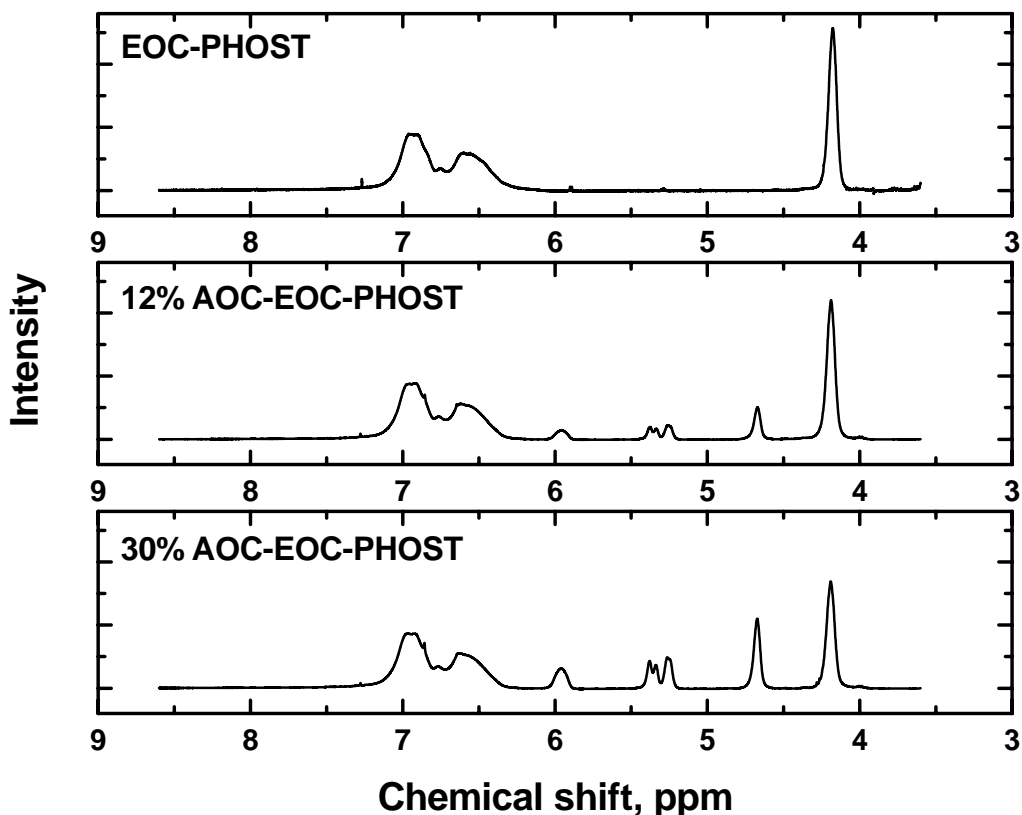


Figure 3-12. ^1H -NMR spectra of PHOST based polymer or co-polymers

Figure 3-11 shows the synthetic route used for making this type of cross-linkable PHOST co-polymer. The percentage of the AOC group, the cross-linkable group, in the copolymer was controlled by controlling the degree of protection accomplished in the first reaction step which substituted EOC groups onto the polymer. All copolymer compositions were measured by proton nuclear magnetic resonance (NMR) (Varian Mercury Vx 400 instrument). Figure 3-12 shows the NMR spectrum of the PHOST based polymer and co-polymers with different percentages of the AOC group.

3.4.2 Thermal Writing Experiments

The polymer thin film samples used for thermal writing were prepared by spin coating 5wt% polymer solutions in Propylene Glycol Methyl Ether Acetate (PGMEA) using a CEE-100CB spin coat and bake system onto a silicon wafer covered with a 340 nm thermal SiO₂ layer. Irgacure 651 (Ciba) (5wt% with respect to polymer solids) was added to the polymer solutions to serve as a free radical generator for cross-linking the PHOST co-polymers after spin coating. The materials were cured by exposing the samples to 248nm UV light with an intensity of 1 mW/cm² for 90 minutes. During exposure, the sample was heated to 100 °C in a N₂ environment to ensure extensive curing of the material.

The AFM thermal writing experiments were performed with the same commercial AFM system (PicoPlus, Molecular Imaging) operated in contact mode with a closed loop 3-axis scanner. Following thermal writing, the thermally generated patterns were imaged in tapping mode using commercial AFM cantilevers (Applied NanoStructures) on the same PicoPlus AFM system. The topography imaging scan speed was controlled at 0.5 Hz for a scan range of 10 micron square with 512 pixels scan resolution. At this scan speed, with proper scanning control parameters, the line scan profiles of right scan and left scan overlapped with each other extremely well, indicating that there were no significant artifacts due to the scanning parameters.

3.4.3 Results and Discussions

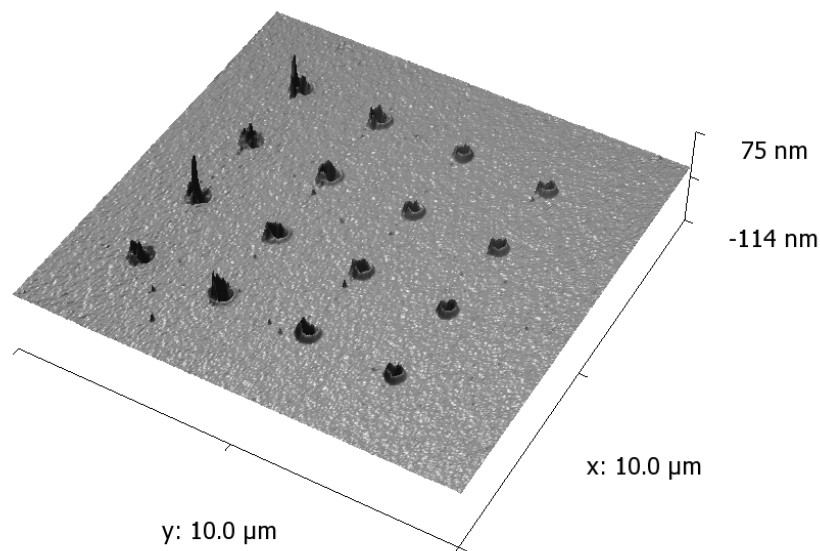


Figure 3-13. AFM topography image (with lighting) of thermally written dot patterns in a PHOST co-polymer containing 12 mole% AOC groups using different heating times, ranging from 5 milliseconds to 20 seconds, and a cantilever temperature of 655 °C.

Figure 3-13 shows an AFM topography image (with lighting) of thermally written dot patterns in a PHOST co-polymer (containing 88 mole% EOC and 12 mole% AOC functionalized HOST monomers) using different heating times, ranging from 5 milliseconds to 20 seconds, at a cantilever temperature of 655 °C. The high temperature required to initiate patterning is due to the thermal resistance at the tip-polymer interface, which is on the order of 10^6 - 10^7 K/W. [18] To generate these patterns the tip was brought to a location, electrical energy was applied to heat the cantilever and its position was maintained at that location for a prescribed amount of time. Once the desired amount of time had elapsed, the tip was cooled and the tip was moved.

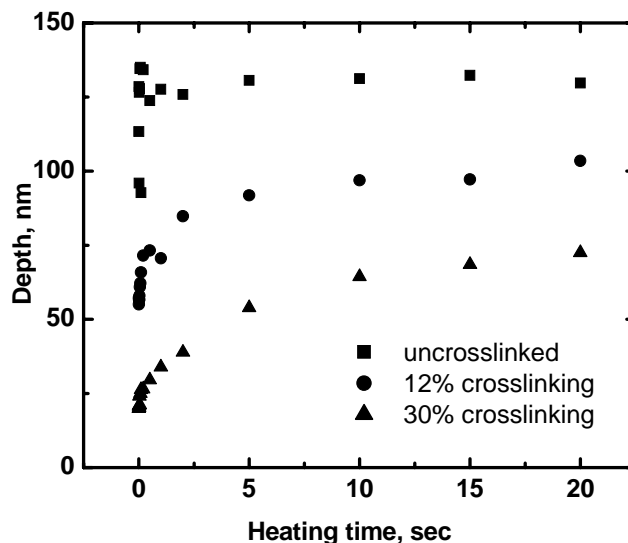


Figure 3-14. Dot depth versus heating time for PHOST co-polymers containing different AOC: EOC monomer ratios

Figure 3-14 shows the dot depth versus heating time for PHOST co-polymers containing different AOC: EOC monomer ratios. The final cross-link density in the polymer should be correlated with the AOC monomer content in the polymer since it is the group that forms cross-links upon exposure to the free radicals. From the data, it is clear that the heated AFM cantilever can penetrate through the entire non-cross-linked polymer film almost instantly. This is because the non-cross-linked polymer turns into viscous liquid when in contact with high temperature AFM cantilever tip. This viscous liquid presents little resistance to penetration of the sharp AFM tip even at relatively low loading forces (~ 5 nN). So in the case of the polymer that is not cross-linked, it is expected that the heated tip can quickly sink into the polymer film by displacing polymer without necessarily accomplishing significant decomposition and removal of polymer. In the case of the cross-linked polymers, the dot depth gradually increases as the heating time increases. This is because at the elevated temperature of the tip, the cross-linked

polymer maintains a reasonable Young's modulus as determined by the crosslink density which provides sufficient strength in the material to resist deformation by the tip [19]. As the heating time increases, the polymer backbone and the crosslink unit can decompose locally in the high temperature vicinity of the heated tip. Thus, the cross-linked polymer network in the vicinity of the heated tip decomposes into low molecular weight products. These low molecular weight products can be easily removed by the heated tip by thermal flow or evaporation, resulting in increases in the hole depth with heating time. For the polymer with the higher crosslink density, more bonds need to be broken per unit volume of material to generate the same low molecular weight product types as in the lower crosslink density material. This means that more time is needed to make a hole in the higher crosslink density polymer with same depth as one in the polymer with a lower crosslink density. This explains why the dot depth for the higher crosslink density polymer increases more slowly with heating time than for the lower crosslink density polymer.

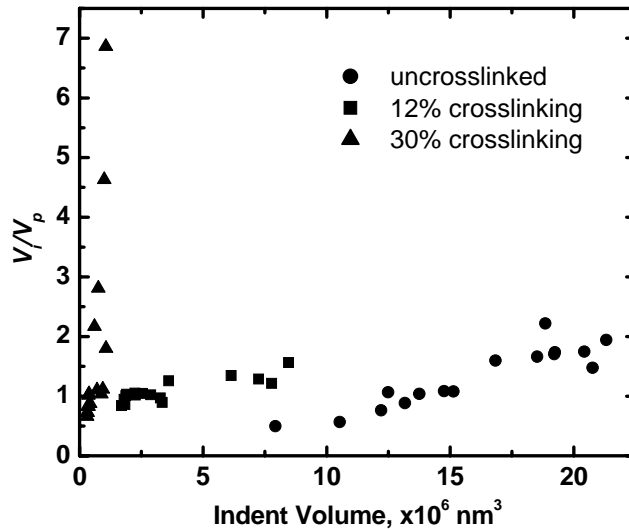


Figure 3-15. Ratio of indent volume to pile up volume (V_i/V_p) versus indent total volume (V_i) for the PHOST based co-polymers with different crosslink densities

When thermal writing was performed on a non-cross-linked polymer, the polymer can turn into a viscous liquid and flow before significant decomposition occurs. This viscous liquid polymer can be easily pushed around by the heated tip, and pile up around the feature. In the case of the cross-linked polymers, the polymer still has enough mechanical strength even when in contact with the heated tip to resist significant thermal flow. This increased resistance to thermal deformation and flow should translate into less pile up material around the written feature. The indent volume (V_i) and pile up volume (V_p) of each thermally written dot are automatically calculated using a MatLab code (see Appendix A) according to the AFM topography image. Figure 3-14 shows the ratio of indent volume to pile up volume (V_i/V_p) versus indent total volume (V_i) for the PHOST based co-polymers with different crosslink densities. A high V_i/V_p ratio indicates there is less pile up of material during thermal writing and that most of the material has been removed by decomposition and vaporization. It might be expected that V_i/V_p should always be larger than one. However, the experimental data suggest that the V_i/V_p can in fact be less than one. There are two possible causes for this phenomenon. One possible explanation is that the material piled up around the feature has a smaller density than the bulk polymer due to the extremely fast heating and cooling time scales during thermal writing which may trap expanded molten polymer in a low density state when it is rapidly cooled. The other possible cause for this result is due to the AFM topography imaging process itself. The AFM tip has a certain size and a certain half angle, which in this case are on the order of the features being written into the polymer film. Thus, the geometry of the AFM tip can be convolved into the topography image, which could make the

measured pile up volume larger than actual pile up volume and the indent volume less than the actual indent volume. It is likely that both mechanisms contribute somewhat to the observed result.

Figure 3-14 shows that for all of the different polymers, the V_i/V_p ratio increases as V_i increases. At the very beginning when the heating power was turned on, the thermally activated mechanical indentation of the film surface reaches an equilibrium state very quickly that contributes a certain initial indentation volume. But in the thermomechanical indentation, no significant amount of material is decomposed, so the material removed from the feature will pile up around the hole. Consequently, the V_i/V_p is small will be small for short heating times. As heating time increases, the polymer film material in the vicinity of the tip decomposes. As material decomposes, the V_i increases as material is removed from the hole. Some of the decomposition products are small molecules which are evaporated by the thermal energy supplied by the heated tip, and thus that material makes no contribution to the pile up volume (V_p) which results in an increase in the V_i/V_p ratio. For the non-crosslinked polymer, during the thermomechanical indentation step the tip can easily reach bottom of the film, and thus a large amount of material is piled up around the hole area. This gives a small V_i/V_p even though the V_i is relatively large. In the case of the crosslinked polymers, they have better resistance to thermal deformation by the heated tip which produces less pile up of material during the initial thermomechanical indentation as the tip is heated.

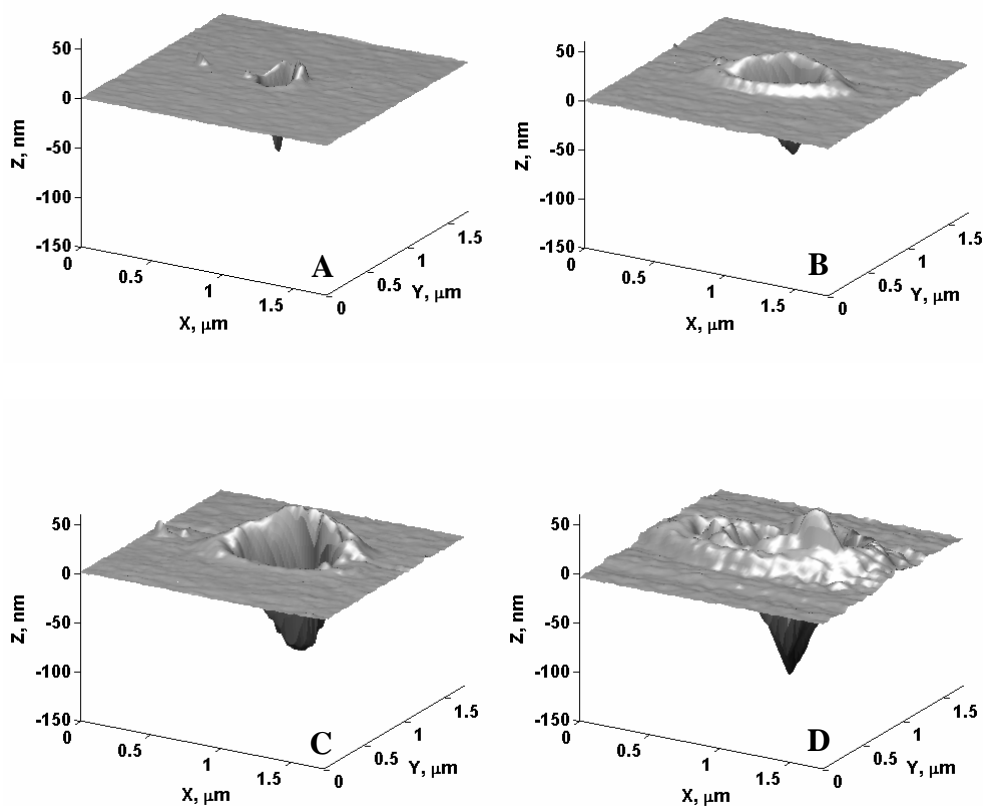


Figure 3-16. Dot thermally written in the 30 mole% crosslink unit PHOST co-polymer; (B) & (C): two dots thermally written in the 12 mole% crosslink unit PHOST co-polymer at two different depths; (D): dot thermally written in the non-crosslinked EOC-PHOST polymer. The heater temperature was 655 °C.

From Figure 3-16, it is obvious that the polymer containing 12 mole% AOC units (i.e. the cross-linking units) exhibits a larger V_i/V_p ratio than the non-crosslinked polymer for similar indent depths (e.g. see the data at an indent volume of $8 \times 10^6 \text{ nm}^3$). When the AOC content in the polymer increases to 30 mole%, the polymer has even higher V_i/V_p ratios at similar feature depths as compared to the 12 mole% AOC polymer. However, as can be seen, the reduced pile up in the higher crosslink density material comes at the cost of lower feature depths at a constant writing time as indicated in Figure 3-14.

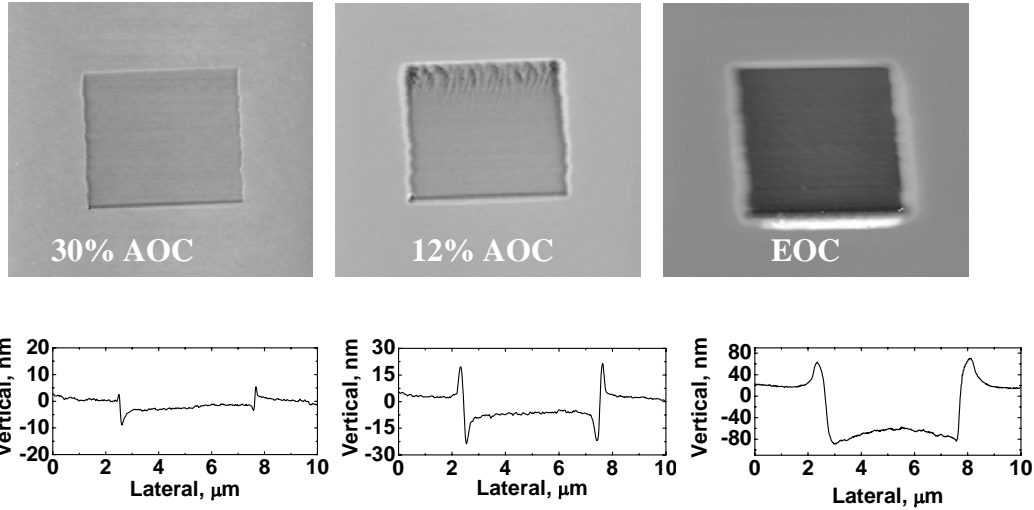


Figure 3-17. 5 micron squares patterned into the three AOC content PHOST-based polymers using identical cantilever temperatures (655 °C), scan speeds (1 Hz), and scan resolutions (512x512 pixels).

In order to produce sharp features using this thermal probe nanolithography process without the requirement of feature post-processing, a large V_i/V_p ratio is desirable and important. A large V_i/V_p ratio indicates less material pile up around the written feature, which translates into a higher fidelity feature and in general a higher resolution process. A high V_i/V_p ratio is also preferred for writing larger areas composed of multiple scans of the AFM tip since material pile up in a single writing pass can accumulate as the tip is repeatedly raster scanned over an area. Figure 17 shows a series of 5 μm squares patterned in the three different polymer compositions studied in this paper using the same heating temperature and scan parameters for all three patterns. It is clear that there is no significant pile up of material around the square feature edges in the polymer containing the 30 mole% AOC units (i.e. highest crosslink density), while in contrast there is some pile up of material at one edge of the 12 mole% AOC polymer

feature and even larger pile up of material pile up around the square patterns formed in the non-crosslinked polymer.

3.4.4 Conclusions

The effect of crosslinking group content in a polymer film writing media, which will correlate with crosslink density in the final polymer film, on the thermal AFM writing performance of the material has been investigated. A PHOST polymer and crosslinkable co-polymer variants of this material were used as the writing media for these experiments. Experimental results show that high crosslink densities are desirable for making fine features without significant thermal material deformation and pile-up of polymer around the written features. However, as the crosslink density of the material is increased it becomes increasingly difficult to write into the material. Higher crosslink densities require longer writing times to generate feature depths equivalent to lower crosslink densities.

3.5 References

- [1] Houlihan, F. M.; Bouchard, F.; Frechet, J. M. J.; Willson, C. G. Thermally depolymerizable polycarbonates. 2. Synthesis of novel linear tertiary copolycarbonates by phase-transfer catalysis. *Macromolecules* (1986), 19(1), 13-19
- [2] Frechet, Jean M. J.; Bouchard, Francine; Eichler, Eva; Houlihan, Francis M.; Iizawa, Takashi; Kryczka, Boguslaw; Willson, C. Grant. Thermally depolymerizable polycarbonates. V. Acid catalyzed thermolysis of allylic and benzylic polycarbonates: a new route to resist imaging. *Polymer Journal* (Tokyo, Japan) (1987), 19(1), 31-49
- [3] Reed, Hollie A.; White, Celesta E.; Rao, Vikram; Bidstrup Allen, Sue Ann;

- Henderson, Clifford L.; Kohl, Paul A. Fabrication of microchannels using polycarbonates as sacrificial materials. *Journal of Micromechanics and Microengineering* (2001), 11(6), 733-737
- [4] White, Celesta E.; Henderson, Clifford L.. Development of improved photosensitive polycarbonate systems for the fabrication of microfluidic devices. *Journal of Vacuum Science & Technology, B: Microelectronics and Nanometer Structures--Processing, Measurement, and Phenomena* (2003), 21(6), 2926-2930.
- [5] White, Celesta E.; Henderson, Clifford L.. Synthesis and characterization of photodefinable polycarbonates for use as sacrificial materials in the fabrication of microfluidic devices. *Proceedings of SPIE-The International Society for Optical Engineering* (2002), 4690(Pt. 1, Advances in Resist Technology and Processing XIX), 242-253
- [6] Yves Martele, Veronique Van speybroeck, Michel Waroquier, Etienne Schacht, Thermo-degradable polycarbonates: Effect of substituents on the degradation temperature. *e-polymers* 2002, no. 049 pp. 1-14
- [7] White, Celesta E.; Henderson, Clifford L.. Photosensitive co-polycarbonates for use as sacrificial materials in the fabrication of microfluidic and microelectromechanical devices. *Proceedings of SPIE-The International Society for Optical Engineering* (2004), 5376(Pt. 2, Advances in Resist Technology and Processing XXI), 850-860
- [8] White, Celesta E. "Advanced methods, materials, and devices for microfluidics" Ph. D Thesis Georgia Institute of Technology 2003
- [9] Devaux, J.; Daoust, D.; Legras, R.; Dereppe, J. M.; Nield, E., Fluorine-19 NMR end-group analysis of a poly(aryl ether ether ketone) (PEEK), *Polymer* (1989), 30(1), 161-4.
- [10] Bicerano, Jozef; Sammler, Robert L.; Carriere, Craig J.; Seitz, Jerry T. Correlation between glass transition temperature and chain structure for randomly crosslinked high polymers. *Journal of Polymer Science, Part B: Polymer Physics* (1996), 34(13), 2247-2259
- [11] W. P. King and K. E. Goodson, "Thermomechanical formation and thermal detection of polymer nanostructures," in *Heat Transfer and Fluid Flow in Microscale and Nanoscale Structures*, M. Faghri and B. Sunden, Eds., pp. 131–171, WIT Press, Southamton (2002).
- [12] W. P. King and K. E. Goodson, "Thermal writing and nanoimaging with a heated

atomic force microscope cantilever,” ASME Trans. J. Heat Transfer 124, 597–597 (2002).

- [13] Hua, Yueming; Saxena, Shubham; Henderson, Clifford L.; King, William P., Nanoscale thermal lithography by local polymer decomposition using a heated atomic force microscope cantilever tip, *Journal of Micro/Nanolithography, MEMS, and MOEMS* (2007), 6(2), 023012/1-023012/6
- [14] W. P. King, T. W. Kenny, K. E. Goodson, G. L. W. Cross, M. Despont, U. Durig, H. Rothuizen, G. Binnig, and P. Vettiger, “Atomic force microscope cantilevers for combined thermomechanical data writing and reading,” *Appl. Phys. Lett.* 78, 1300–1302 (2001).
- [15] D. S. Fryer, P. F. Nealey, and J. J. de Pablo, “Thermal probe measurements of the glass transition temperature for ultrathin polymer films as a function of thickness,” *Macromolecules* 33, 6439–6447 (2000).
- [16] W. P. King, T. W. Kenny, K. E. Goodson, G. L. W. Cross, M. Despont, U. Durig, H. Rothuizen, G. Binnig, and P. Vettiger, “Design of atomic force microscope cantilevers for combined thermomechanical writing and thermal reading in array operation,” *J. Microelectromech. Syst.* 11, 765–774 [2002] .
- [17] P. Vettiger, G. Cross, M. Despont, U. Drechsler, U. Doring, B. Gotsmann, W. Haberle, M. A. Lantz, H. E. Rothuizen, R. Stutz, and G. K. Binning, “The Millipede—Nanotechnology entering data storage,” *IEEE Trans. Nanotechnol.* 1, 39–55 (2002).
- [18] J. Lee, T. L. Wright, T. W. Beecham, S. Graham, and W. P. King, “Electrical, thermal, and mechanical characterization of heated microcantilevers,” *J. Microelectromech. Syst.* 15, 1644–1655 (2006)
- [19] Ferdinand Rodriguez, *Principles of Polymer Systems* (4th Edition), (Taylor & Francis) 1996 p.317

CHAPTER 4

3D THERMAL WRITING

4.1 Introduction and Background of 3D Lithography

The atomic force microscope (AFM) offers significant opportunities to probe and manipulate material at the nanometer scale. [1] The scaling of these probing and manipulating techniques to large arrays of AFM probes may become the technology that enables the practical implementation of nanotechnologies for widespread use. [2,3,4] While there exist a number of nanometer-scale manufacturing techniques that exploit the AFM, there remain several unmet needs. While sub-100 nm resolution is possible with a number of techniques, the writing speed is a significant challenge, with typical tip speeds in the range 0.1-1 nm/sec. Furthermore, AFM writing techniques offer little three-dimensionality, with most writing being very thin marks or at best digging [5,6,7] or building [8,9] that offers little control in the z-direction. Finally, the most successful nanowriting technique would be able to control writing at the single-tip level. [10,11,12] This section presents an AFM nanowriting technique for high-speed and three-dimensional nanowriting that can be controlled at the single-tip level.

Figure 4-1 shows a schematic of the nanowriting approach, in which heat from a local probe to decompose an organic material into vapor reactants. The decomposition leaves no pileup or residue that is characteristic of other subtractive AFM nanowriting approaches. The rate of material decomposition can be modulated with the tip temperature and speed, and therefore it is possible to write true three-dimensional structures. The overall writing speed is up to 10^5 times faster than competing probe-based writing technologies.

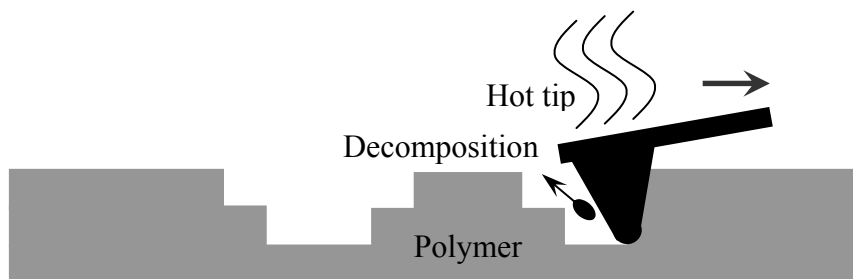


Figure 4-1. Cartoon of 3D nano-sculpting using heated probe tip

4.2 Experimental

The experiments use the same thermal AFM cantilever described in previous Chapters. The AFM thermal writing experiments were performed with a commercial AFM system (PicoPlus from Molecular Imaging) operated in contact mode with a closed loop 3-axis scanner. Cross-linkable polycarbonate IV (CPC-4) was used as the writing material. Polymer thin film samples preparation followed the exact same procedures described in previously Chapter 3.

In the thermal writing experiments, before applying the heating voltage, the cantilever was first brought to the polymer surface, and then start to scan over the surface. The heating voltage was turned on and the tip was heated to a high temperature when it approached the place where the material needs to be removed. The polymer in contact with the heated probe tip can be removed by thermal decomposition. The scan speed can be changed during scanning. The scan speed can vary from 0.4 to 60 $\mu\text{m}/\text{sec}$. The decomposition depth of polymer can be controlled by controlling the heating temperature and the scan speed. By varying the heating temperature and/or the scan speed

when the tip is scanning across an area, a 3D structure can be produced. The versatility of this technique can be further improved by using multiple scans at the same area.

Without applying heating voltage, the cantilever just works in a normal contact mode to imaging the surface. When the heating voltage is turned on, the cantilever can reach thermal equilibrium within 10 microseconds. Since the probe tip physically contacts polymer surface, the polymer in a very small region around the tip will be heated up instantly. When the polymer is heated above its decomposition temperature, the polymer chain is broken down into small molecules. Most of these small molecules are evaporated by the hot probe tip. At the same time, the tip sinks into the polymer film. The depth the tip can sink into the polymer film is determined by how much polymer is decomposed under the hot tip. And this is determined by heating temperature and scan speed. For the un-decomposed polymer, because it is cross linked, it will not be melted and can keep the original shape to construct a 3D structure. Some minor residue might leave behind, and pile up around the thermal written area. But this residue can be removed by washing with isopropyl alcohol (IPA).

4.3 Results and Discussions

4.3.1 Effect of Heating Temperature and Scan Speed on Thermal Writing

Figure 4-2 shows an AFM topograph of a set of lines made by thermal writing with a hot probe tip at a constant temperature of 663 °C, but different scan speeds. The line width at the top is around 100-200nm, which depends on the depth of the line. The cross section profiles of the lines show that at a constant heating temperature, the line depth decrease as the increasing of the scan speed. This is because at higher scan speed,

less time is used to scan a single line. Then less amount of polymer can be decomposed, which results in less deep are the lines.

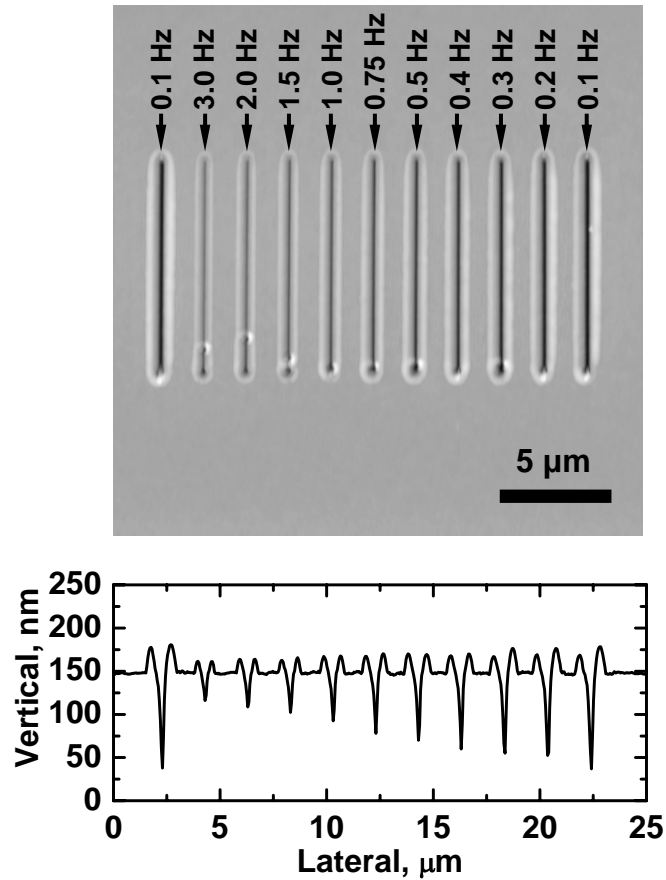


Figure 4-2. Thermal written 10 μm lines at 663 °C with different scan speeds

The numerical data presented in Figure 4-3 give more detailed information about the line depth vs. heating temperature and heating time. The heating time is calculated by dividing the line length by the total time used to thermal write a single line.

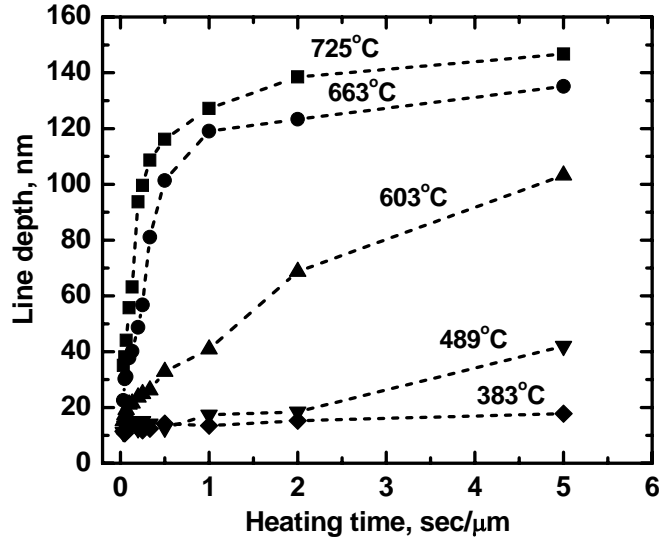


Figure 4-3. Line depth vs. heating time of single line scan

We can see, when the heating temperature is 383 °C, the line did not go deeper when increase the heating time. This indicates that although the temperature of the heater on the cantilever was above the decomposition temperature of the polymer observed in standard TGA (see Figure 3-4); the polymer contacting the probe tip was not hot enough to be decomposed in this case. One reason for this is there is a temperature drop along the height of the tip. Also there is a temperature drop at the interface between the tip the polymer because of the interface thermal impedance. And the other reason is nano scale thermal writing need much higher temperature than standard TGA does to decompose polymers. These will be discussed in detail in Chapter-8.

We believe that about 15 nm line depth at this heating temperature is only from the thermal indentation by the hot tip. For the temperatures of 489 °C and above, the line depth increase as the increasing of heating time. The higher is the heating temperature,

the larger is the slopes of the plots at the beginning, which indicates a high decomposition rate. This is because the decomposition rate increases exponentially with regards to the temperature. But as the line depth goes above 100 nm, the line depth increasing slows down. One main factor leads to this is that the temperature at the tip drops when it is buried into the polymer film. When the line goes deeper, there is more contact area between the tip and polymer. Heat transported from the heater to tip can be easily dissipated. This can cause the temperature drop of the tip. Because the tip has an angle, the amount of polymer need to be decomposed is proportional to the square of the line depth. When the line goes deeper, much more polymer needs to be decomposed in order to keep the tip at the same depth. At this time, the heat conduction rate through the tip can be a limit factor for the polymer decomposition. Also, the film thickness is about 145 nm. The line can not go deeper than this value.

By modulating the combination of the heating temperature and the heating time, we can control the decomposition depth when a heated tip scans on the polymer surface. So in a single scan, we can remove different amount of polymer at different positions by changing the scan speed and/or heating temperature. This means we can make a 3D structure in a single pass. Or we can keep constant heating temperature and scan speed in one single pass. And use multiple scans to selective remove different amount of material at different position to make a 3D structure.

4.3.2 Residue Removal

The writing material used for 3D thermal writing was cross-linked copolycarbonate (CPC-4). As discussed before, the polycarbonate chain can be decomposed into small molecules. These small molecules are volatile at elevated temperature, and can

be vaporized instantly when in contact with heated cantilever tip. However, decomposition of this CPC-4 material exhibits a low residual weight tail beginning at approximately 8.0 wt % that does not completely disappear until a temperature of approximately 430 °C. This residual mass that remains at higher temperatures is a result of the methacrylate polymer cross-links, which are formed in the polycarbonate. Because this residual mass needs higher temperature to be cleanly decomposed than the carbonate main chain, during thermal writing, methacrylate cross-linking network may not be decomposed and vaporized, and leaves residue in the thermal written area. This residue will not form significant pile-up when a small area is thermally patterned. But this residue is considerable when a large area is patterned. Image (1) in Figure 4-4 shows a 3D feature thermally patterned using AFM thermal writing. From the image we can see there is considerable material pile-up around the feature. The cross section of this 3D feature is supposed to have a T-shaped profile if there is no residue. And the AFM cross section (Plot (1) in Figure 4-5) also clearly shows that there is considerable residue in the patterned area. It is very hard to tell from the normal AFM topography image whether the residue is the same material as the bulk polymer or not. There are four possible decomposition products for the cross-linked polymer: hexane diene, noborene diol, carbonate oligomer, and methyl methacrylate oligomer. These decomposition products should have less mechanical properties than the bulk cross-linked polymer. One easy way to tell whether this residue is cross-linked polymer or decomposition product is imaging the patterned area with a hot AFM tip with a temperature right below the decomposition temperature of the cross-linked polymer. Then during contact mode topography imaging, the medium hot tip can penetrate the decomposition residue, but it can't penetrate the

cross-linked polymer. Image (2) in Figure 4-4 shows an AFM topography image of the same feature imaged by a heated AFM tip with a heater temperature of 292 °C. This image shows a very well defined feature with T-shaped cross section profile. No residue can be observed from the image. When the same patterned area was imaged with the same tip again without heating, the residue appears again in the AFM topography image. The only difference is the residue was spread out a little, and the cross section profile became smoother.

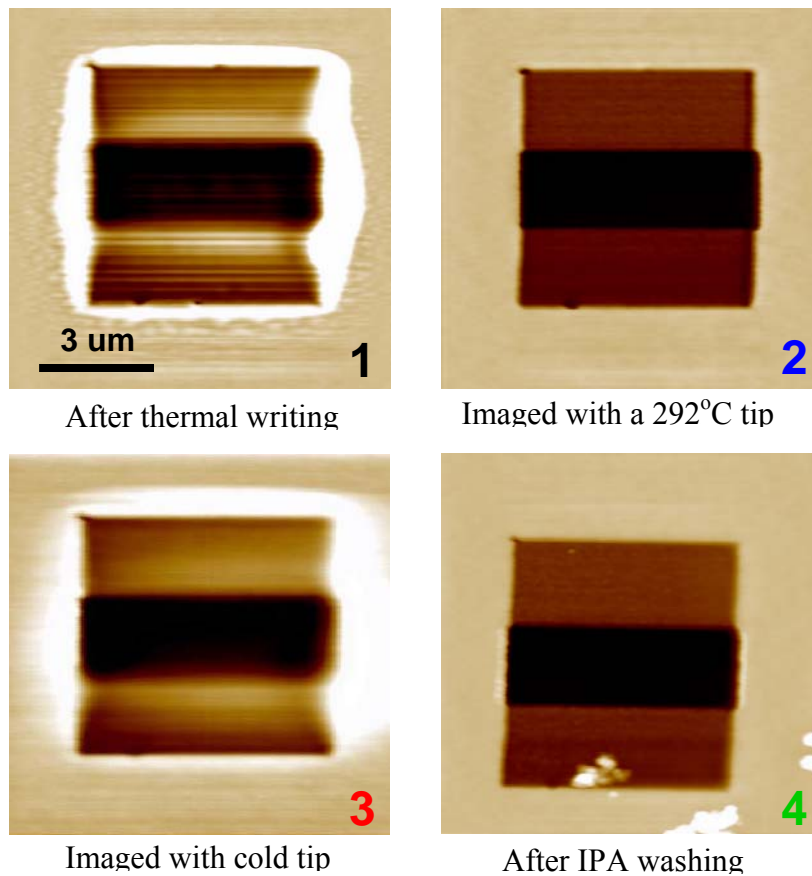


Figure 4-4, AFM topography image of thermally patterned 3D feature in CPC-4

By comparing the image (3) and image (2) in Figure 4-4, we know that the residue in the patterned area are not cross-linked bulk polymer, they are decomposition product. The hexane diene and noborene diol are volatile material, they should be evaporated when they are heated. But after scanned with a heated tip, no residue seems to be removed. This indicates the residue is carbonate oligomer, methyl methacrylate oligomer, or the mixture of these two.

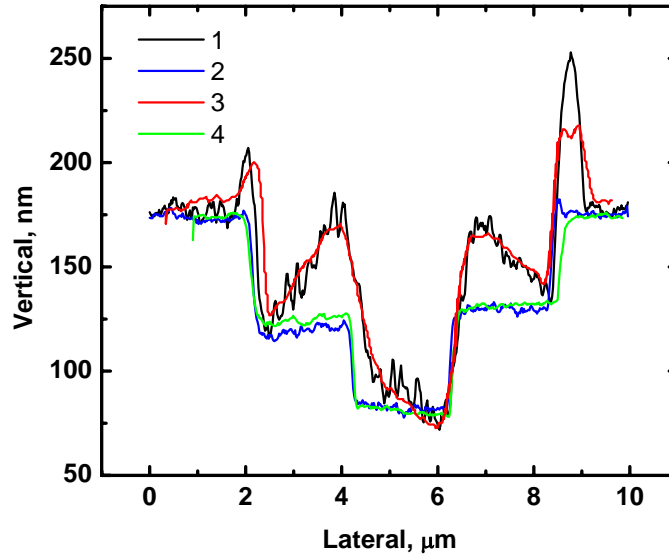


Figure 4-5. Cross section profiles of the 3D feature

The sample was washed with isopropyl alcohol (IPA) and de-ionized water (DI water), and then dried with N₂ gun blowing. The pattern was imaged again with the same cantilever without heating. Image (4) of Figure 4-4 shows the AFM topography image of the feature after washing. The image shows that most of the residue was removed. There are a few particles around the feature. They are probably from the environment, because the washing processes were conducted in regular room environment. This indicates that

the residue is soluble in IPA or water. This result is expected, this above discussion shows that the residue are oligomers, which may contains hydroxyl group or carboxylic group. Materials containing these groups are very likely soluble in solvents like IPA or water.

4.3.3 Direct 3D Patterning

Figure 4-6 shows two different 3D structures made by different heating temperature, and scan speeds combined with multiple scans. These two structures are imaged after IPA washing to remove the residue, followed by baking at 100 °C for 5 minutes to remove the solvent. For the two adjacent inversed pyramid shaped slots, the middle level is made by thermal writing at 663 °C with a scan speed of 28 μm/sec, and the bottom level is made by thermal writing at 725 °C with a scan speed of 7 μm/sec. The height of the first step from the bottom is about 50 nm, and the height of the second step is about 100 nm. The RMS roughness of the middle level surface is only 2.2 nm. The two slots have almost identical cross section profile. This shows that this 3D nano scale sculpting technique is very repeatable. For the pyramid shaped 3D structure, the middle level is made by thermal writing at 643 °C with a scan speed of 10μm/sec, and the bottom level is made by thermal writing at 725 °C with a scan speed of 10μm/sec. In order to make the isolated top square and middle square, both middle level and bottom level were made by two separated scans.

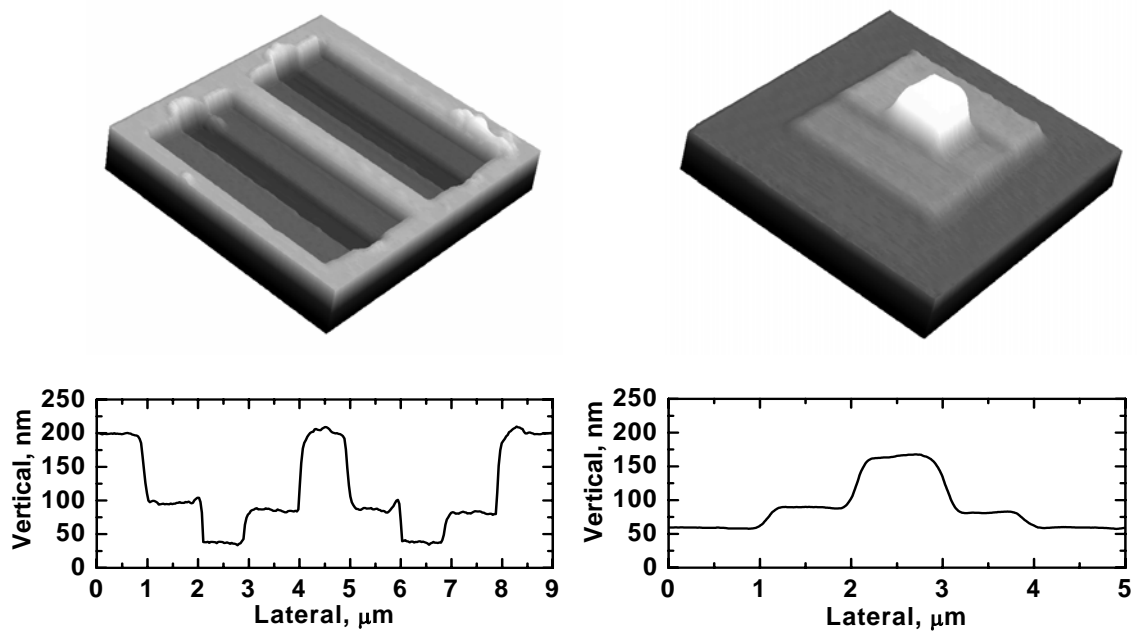


Figure 4-6. AFM 3D images of 3D structures made by multiple scans.

The RMS roughness of the middle level surface is only 1.7 nm. From the 3D image of the pyramid we can see two separated scans were not stitched together perfectly. The height difference between the two separate scans is about 7 nm, which is about 10% of the depth of that level. There are two factors may lead to this. One is the thermal decomposition was operated in an open loop fashion; there was no feed back to dynamically adjust the decomposition depth. Another one is that in our current AFM system, there is no such a controller to automatically stitch different scans accurately. We believe, with some more advanced controllers, the accuracy of the decomposition depth and the stitching can be improved significantly.

These nano scale 3D structures have the potential to be used as molds to make nano scale 3D objects, like 3D masters for imprinting. Also the patterned 3D structures

have the potential to serve as a supporting layer in fabrication of some nano scale devices. If necessary, the polymer can be thermally decomposed to make buried 3D voids. The throughput of this 3D nano-sculpting technology can be linearly scaled up by using a cantilever array.

4.4 Conclusion

We reported a novel high speed nano scale 3D sculpting technology using a heated probe tip. A cross linked polycarbonate was used as the material. We found the amount of material thermally decomposed by a heated probe tip can be very well controlled by choosing different heating temperatures and scan speeds. The undecomposed material can keep the shape and give a 3D structure. Some nano scale 3D structures are demonstrated. The RMS roughness of the sculpted surface can be as low as 1.7 nm.

4.5 References

- [1] Binnig, G.; Quate, C. F.; Gerber, C., Atomic force microscope, *Physical Review Letters* 1986, 56, 930-933.
- [2] Hong, S.; Zhu, J.; Mirkin, C. A., Multiple ink nanolithography: Toward a multiple-pen nano-plotter, *Science* 1999, 286, 523-525.
- [3] Vettiger, P.; Cross, G.; Despont, M.; Drechsler, U.; Duerig, U.; Gotsmann, B.; Haberle, W.; Lantz, M.; Rothuizen, H.; Stutz, R.; Binnig, G., The "millipede" - nanotechnology entering data storage, *IEEE Transactions on Nanotechnology* 2002, 1, 39-64.
- [4] King, W. P.; Kenny, T. W.; Goodson, K. E.; Cross, G. L. W.; Despont, M.; Duerig, U. T.; Rothuizen, H.; Binnig, G.; Vettiger, P., Design of atomic force microscope cantilevers for combined thermomechanical writing and thermal reading in array

- operation, *Journal of Microelectromechanical Systems* 2002, 11, (6), 765-774.
- [5] Schumacher, H. W.; Kracke, B.; Damaschke, B. Modification of thin gold films with a scanning force microscope. *Thin Solid Films* (1995), 264(2), 268-72.
- [6] Sohn, L. L.; Willett, R. L. Fabrication of nanostructures using atomic-force-microscope-based lithography. *Applied Physics Letters* (1995), 67(11), 1552-4.
- [7] Jin, X.; Unertl, W. N. Submicrometer modification of polymer surfaces with a surface force microscope. *Applied Physics Letters* 1992, 61, (6), 657-659.
- [8] Nelson, B. A.; King, W. P.; Laracuente, A. R.; Sheehan, P. E.; Whitman, L. J. Direct deposition of continuous metal nanostructures by thermal dip-pen nanolithography. *Applied Physics Letters* (2006), 88(3), 033104/1-033104/3
- [9] Li Y; Maynor B W; Liu J Electrochemical AFM "dip-pen" nanolithography. *Journal of the American Chemical Society* (2001), 123(9), 2105-6.
- [10] Sheehan, P. E.; Whitman, L. J.; King, William P.; Nelson, Brent A. Nanoscale deposition of solid inks via thermal dip pen nanolithography. *Applied Physics Letters* (2004), 85(9), 1589-1591
- [11] Su, M.; Pan, Z. X.; Dravid, V. P.; Thundat, T. Locally Enhanced Relative Humidity for Scanning Probe Nanolithography *Langmuir* 2005, 21, (24), 10902-10906.
- [12] King, W. P.; Saxena, S.; Nelson, B. A.; Pitchimani, R.; Weeks, B. L. Nanoscale thermal analysis of an energetic material, *Nano Letters* (2006), 6(9), 2145-2149

CHAPTER 5

SELECTIVE ALD

5.1 Introduction and Background

In previous chapters, we have already showed that the thermal probe lithography method described in this work is a high resolution and high speed probe lithography method. And it can use various types of polymer as the writing material [1]. These advantages offer this method promising potential applications in device fabrication.

Fabrication of high quality nanoscale material patterns is a critical and enabling technology for modern micro- and nanoscale device manufacturing (e.g. integrated circuit fabrication), and the previously reported polymer patterning method utilizing a heated cantilever can produce protective masking layers analogous to photoresist structures that can be used for traditional subtractive microfabrication processes. However, in addition to developing the maskless lithography methods utilizing the heated cantilever process, we have an interest in developing additive manufacturing techniques that can simplify microfabrication processes by reducing the number of process steps and help avoid damage to devices due to harsh subtractive material removal processes such as plasma etching. [2] In this section, the development of a combined method that can utilize the heated cantilever probe to pattern a polymer masking layer that can serve as a template for area selective atomic layer deposition techniques (ASALDT [3,4]) is reported. In this way, virtually any material that can be deposited by atomic layer deposition (ALD) can be deposited in a directly patterned manner.[5,6] In particular, this section demonstrates the successful patterned deposition of TiO_2 features using a heated cantilever probe generated patterned polymer masking layer.

5.2 Experimental

The AFM thermal writing experiments were performed with a commercial AFM system (PicoPlus, Molecular Imaging) operated in contact mode with a closed loop 3-axis scanner. The AFM topography and phase imaging were operated in tapping mode using commercial AFM cantilevers (Applied NanoStructures) on the same PicoPlus AFM system.

The heated AFM cantilevers used in this section is the same type of thermal cantilever used in previous chapter. The cantilevers are made of doped single crystal silicon. An electrical resistance heater-thermometer integrated into the silicon cantilever allows for temperature-controlled heating of the cantilever tip. The cantilever used for the experiments reported in this paper had a base electrical resistance of 1.89 Kohm at room temperature, a spring constant of 0.15 N/m, a tip radius of curvature estimated at 30 nm, and a tip half angle of 15°. The cantilever temperature was calibrated to within 5 °C using Raman thermometry. A typical thermal writing area was a 5um square. Scan speed was 1.0 Hz, and the scan resolution was 512 line/square.

Polymethyl methacrylate (PMMA) (Aldrich, Mw = 15,000) was used as the protective polymer masking layer that was patterned using the heated cantilever probe tip and subsequently used to direct area selective atomic layer deposition. PMMA was chosen as the polymer masking layer for this study due to the fact PMMA was the masking layer first used in earlier reported area selective atomic layer deposition work. Thin film PMMA samples were prepared by spin coating a 3wt% PMMA solution in toluene onto silicon wafers covered with an approximately 300 nm thick thermally grown silicon oxide. The PMMA film thickness was measured using an M-2000 Variable Angle

Spectroscopic Ellipsometer (VASE, J.A. Woollam). PMMA thin films with a nominal thickness of 110 nm were used in this work. After thermal writing, a plasma descum etch was performed on the patterned polymer films in some cases using a Harrick PDC-32G plasma cleaner/sterilizer with air as the source gas and a base pressure of 0.4 torr.

ALD deposition of titania was performed using a home built ALD system. Titanium-isopropoxide (TiIP) and deionized (DI) water were used as precursors for deposition of TiO_2 , and N_2 was used as both carry gas and purge gas. A typical ALD cycle consisted of: (1) a 5 sec TiIP pulse, (2) a 30 sec N_2 purge, (3) a 5 sec DI water pulse, and (4) a 30 sec N_2 purge.

5.3 Results and Discussion

During the thermal writing experiments, a cold AFM cantilever tip was brought in contact with the polymer surface, the heating power to the cantilever was turned on, and the heater temperature of the heated cantilever was maintained at approximately 615°C by control of the heating power. At the time the tip power was turned on, scanning of the tip over the polymer surface was simultaneously started. The goal in the thermal polymer patterning using the heated probe tip is to have the polymer in contact with the heated tip decomposed cleanly and quickly, with the decomposition products being evaporated virtually instantly as the tip scans. Ideally, no residue is left behind and no significant thermal deformation of the remaining parts of the polymer film occurs during the writing process. In this case, for the PMMA films a variety of cantilever temperatures and tip scan rates were studied to determine an optimum writing process for the PMMA. In terms of highest feature resolution without significant thermal deformation while also attempting to obtain the maximum writing speed for single pass writing, a cantilever

temperature of 615 °C combined with a tip scanning rate of approximately 1 $\mu\text{m}/\text{sec}$ appeared to be optimal for the PMMA thin films.

Figure 5-1 shows AFM images of a square feature thermally written into the PMMA polymer thin films using these conditions. As can be seen, the height difference between the thermally written area and the non-written field is approximately 105nm. Given that the original film thickness was 110nm, this means that a residual layer of less than 5nm is left in the patterned area for the PMMA films under these conditions. This small amount of the residue in the thermally written areas can be identified to some degree in the AFM topography images as the slightly raised area in the central portions of the bottom of the written feature. The residue is more clearly identified in the AFM phase imaging.[7] From the phase image (A_2) in Figure 5-1, one observes that the material at the bottom of the thermally written area and the non-written areas have the same phase lag, indicative of both regions being the same type of material. While this pattern definition and low residue is quite good and would be sufficient for many applications, leaving behind a 5 nm thick residual layer is not desirable for an area selective atomic layer deposition technique that relies on the exposure of reactive sites in the unmasked areas to promote ALD film growth on the substrate. While the amount of residue in the bottom of the feature can be further reduced by either using higher cantilever temperatures or slower tip scanning speeds, the degraded resolution due to the higher temperatures or the dramatic increases in writing time due to slower tip scanning speeds are not desirable. Therefore, a plasma descum etch was implemented following the heated cantilever writing process to remove the final small amount of residue.

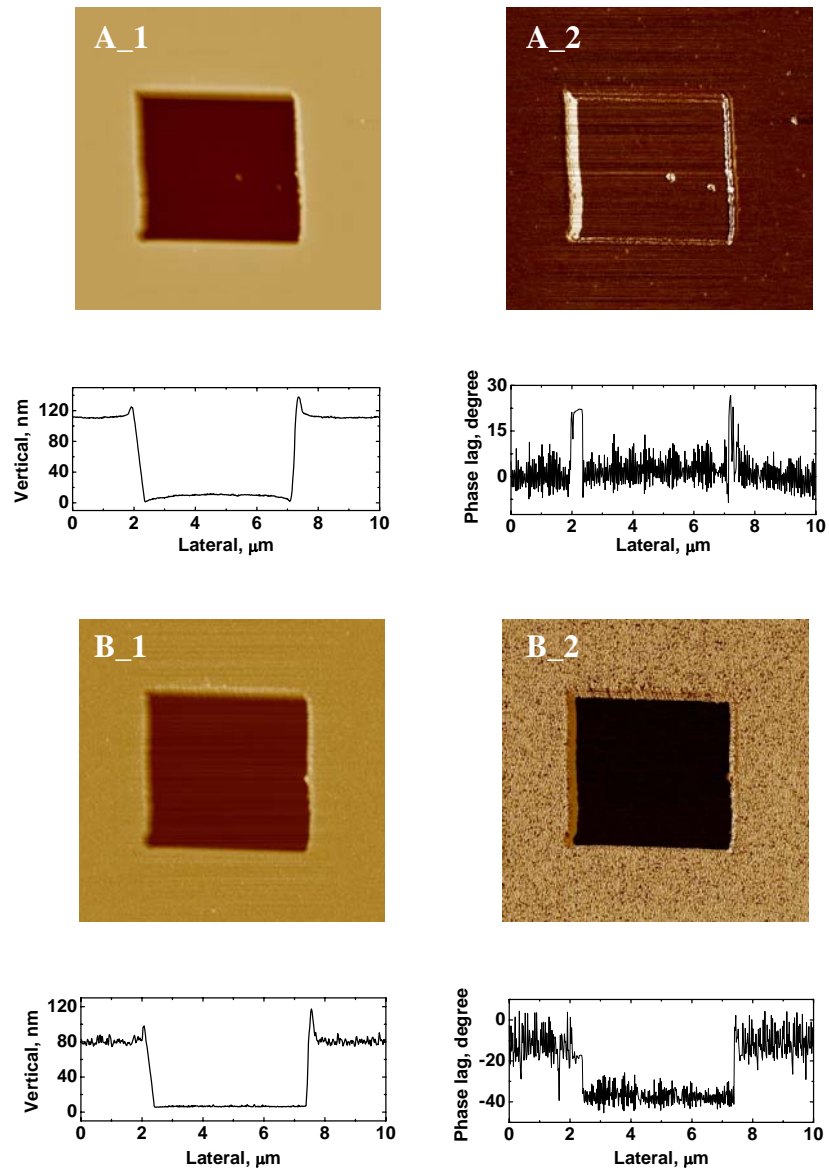


Figure 5-1. A thermal written square before and after a 130 sec O₂ plasma descum. A_1 and A_2 are topography and phase image of thermal written square before O₂ plasma descum, respectively; B_1 and B_2 are topography and phase image of thermal written square after O₂ plasma descum.

The film residue can be very easily removed by an O₂ plasma etching which cleanly removes the organic polymer residue. From comparing the phase images (A_2 and B_2) in Figure 5-1, we can see after a 60 second O₂ plasma descum process; the phase image shows that there is a clear phase difference between the thermally written area and the non-written area. The topography scan of the thermally written area after the O₂ descum etch also shows that the bottom of the feature is extremely smooth and flat, exactly what one would expect from a high quality thermal oxide coated silicon substrate. These results clearly indicate that the material in the thermally written areas is different from the material in the unwritten areas, indicative of the excellent organic removal ability of the O₂ etch. However, in these initial tests, it was clear that the lengthy O₂ etch removed a significant amount of polymer from the unwritten areas (i.e. the PMMA film thickness after the 60 s etch was only 80 nm as compared to the initial 110 nm film thickness before plasma processing) and that such an etch time was most likely a significant over estimate of the time required to clean the residue. A series of etch studies were performed in which the O₂ etch time was varied and the thickness of unwritten polymer film regions was measured before and after etch along with AFM probing of the bottom of the written features before and after the O₂ etch. It was observed that no discernable residue was left in the bottom of the thermally written areas for etch times longer than approximately 15 seconds (i.e. suggesting that the residue etch rate was approximately 0.33 nm/sec under the etch conditions used), and that approximately 8 nm of polymer film in the unwritten areas was also removed in the same amount of time (i.e. translating into an approximately 0.5 nm/sec raw PMMA etch rate. This data suggests that the residue formed at the bottom of the thermally written feature is not simply

PMMA since the residue has a noticeable slower etch rate in the O₂ plasma than the PMMA unwritten regions. This result is reasonable considering the fact that any residue left in the polymer film after such a high temperature writing process is likely to be more carbon rich than the original polymer, which would generally result in a lower etch rate.

The thermal writing followed by the O₂ plasma descum etch can apparently completely remove the PMMA and any organic materials from the substrate surface, as evidenced by the ability to deposit titania into the written features using an ALD process (see Figure 5-2). Without the descum etch or without using the tip to remove the majority of the PMMA film, no titania deposition is observed on the substrate or polymer surfaces. The ALD process in this work was run at 140 °C. Figure 5-2 shows the AFM images of a thermally written square feature after ALD of TiO₂ for 200 cycles. Because the ALD temperature was above the glass transition (T_g) of the PMMA film (T_g ~ 110 °C), some deformation and flow of the polymer at the feature edge can be observed. The AFM topography image of the pattern, after stripping away the PMMA masking layer using a simple acetone wash, shows that there is approximately 2 nm of TiO₂ grown in the square area. Also the phase image of the square after removing the masking layer shows that there is a phase difference between square area and unwritten area. This further indicates the material in the square is different from the material outside the square. The titania film growth rate under the growth conditions used is calculated to be 0.01 nm/cycle, which is slightly lower than values reported for similar ALD processes in the literature [8]. This lower growth rate though is most likely due simply to the fact that

the ALD process temperature used in this work is only 140 °C which is 10 °C below the ALD temperature used in the previous literature.[9]

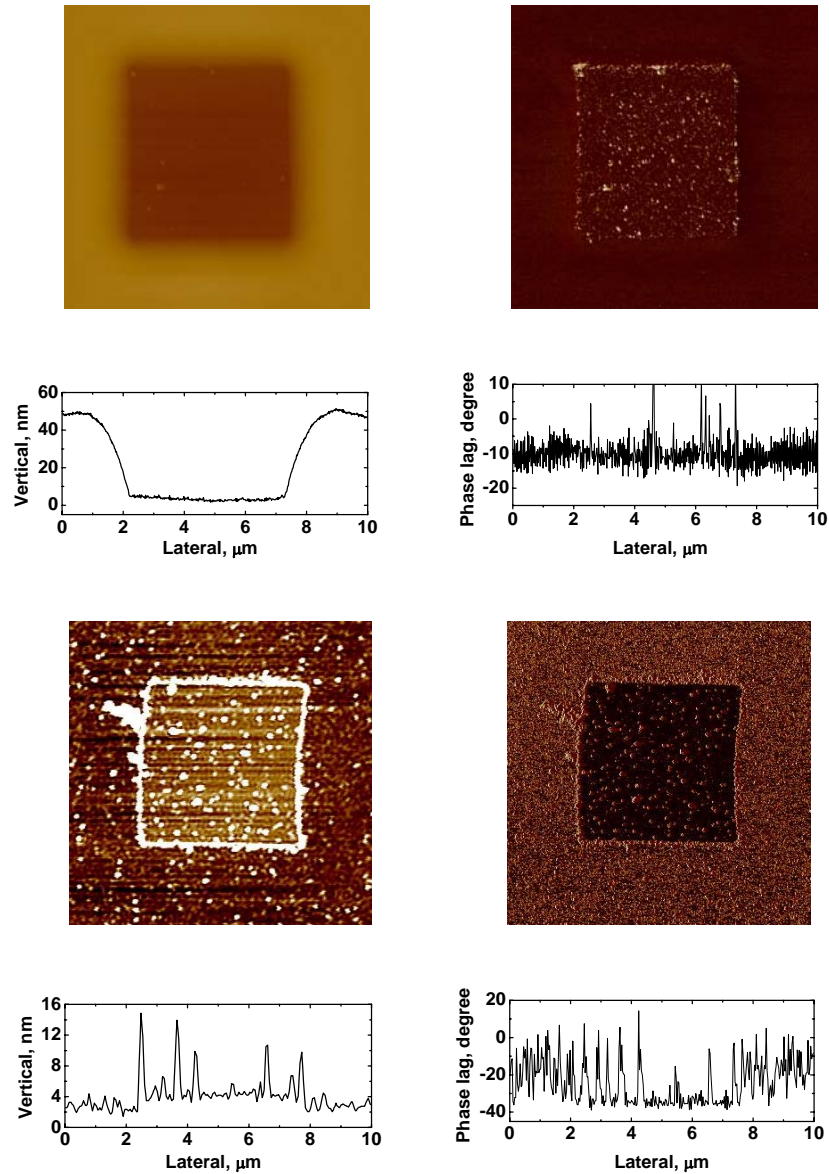


Figure 5-2. Selective ALD TiO₂ pattern in thermal written area. A_1 and A_2 are topography and phase image of the square after ALD thermal written, respectively; B_1 and B_2 are topography and phase image of the square after stripping the PMMA masking layer, respectively

It is also possible that the hydroxyl group density in the thermally written area may not as high as that on a freshly prepared oxide sample surface such as the ones used in the previous ALD literature, and this lower initial ALD reaction site density may lead to a slow initial growth rate before the surface is densely covered with a titania layer.

We can see there are a lot of particles on the surface after washing away the PMMA masking film. This could be due to a number of factors including. First it is possible that either the PMMA masking material, solvents, or simply lab environment used in this work are contaminated with particles and that after deposition of the film from solution and subsequent removal of the film from the wafer using solvent, particle contamination is left behind on the sample surface from one of these sources. Control experiments in which the pure solvents are used to wash a blank substrate and subsequent inspection by AFM would reveal if the solvents are themselves the source of particle contamination. Control experiments could also be conducted in which the PMMA film is applied and then is put through any baking steps used in the normal ALD process that was used to generate the TiO₂ patterns with the exception of no exposure to any reactive ALD precursors. Removal of these control polymer films using the same solvent washing procedures would reveal if the film deposition and removal process itself is responsible for particle deposition. Since particle defects are present in even the nominally open or unmasked regions of the substrate where the ALD titania was deposited on purpose, it is believed that this particle contamination due to the solvents, polymer, or lab environment are a likely cause of the observed defects. Second, it is possible that particles are generated in the ALD chamber itself during ALD cycling or are already present in the chamber, and that such particles can land and deposit randomly on

the substrate during processing but are not removed effectively during subsequent washing steps. If particle generation in the gas phase during ALD deposition is indeed the problem, it would be expected that the number of particles observed on the substrate might scale with the total number of ALD cycles. Therefore experiments in which the length of the ALD process is varied and particle numbers and sizes are measured as a function of ALD cycle number could indicate if this is a likely cause. If the chamber is inherently contaminated, experiments in which a blank silicon substrate is placed in the ALD chamber and the purge gas is allowed to flow through the chamber for an amount of time equivalent to the total ALD cycle time followed by AFM wafer inspection could be performed to determine such a contamination source. Third, it is possible that during ALD deposition some precursor diffuses into the polymer masking film and subsequently acts as a nucleation site for small amounts TiO_2 deposition in the PMMA film. These TiO_2 regions formed in and on the polymer would not in general be soluble in the washing solvent and could settle on the sample surface during the PMMA mask removal. Previous work in our group would suggest that this mechanism is not likely to be a major cause of the observed particles since water and titanium precursor desorption are extremely fast from PMMA masking layers and the diffusivity of the titanium precursor is very slow in PMMA. Previous TiO_2 deposition using lithographically defined PMMA masks did not observe such significant particle deposition in the PMMA masked areas. Experiments could be conducted which utilize longer purge cycle times in the ALD, and thus if it is removal of precursor from the PMMA masking layer that is the critical factor in determining particle deposition on the sample, it would be expected that the particle counts would decrease with increasing purge cycle times. Fourth, it is possible that the

oxygen plasma used to descum the thermally written areas can reactively convert the surface over all of the PMMA masking film to some extent to contain surface hydroxyl and other reactive sites. If such reactive generation of sites on the polymer surface took place in the plasma during descum, subsequent exposure to the titanium precursor during ALD cycling could produce TiO₂ particles randomly on the polymer surface. Again, during washing, these particles could settle onto the sample surface. If such particles are formed on the surface of the polymer film, they are not immediately obvious from the AFM scans of the PMMA mask after ALD (see Figure 5-2A). However, control experiments in which blanket PMMA films that have not been exposed to the thermal writing process should be processed through the descum and ALD process to determine if particle growth and deposition is an inherent problem with this process combination. Fifth, it is possible that the oxygen plasma descum forms pinhole defects in the PMMA masking layer that allow for ALD precursor exposure to the underlying silicon substrate in those regions. Such exposure of the substrate to the reactive ALD precursors would be expected to generate titania regions in those locations which could remain on the wafer after stripping of the PMMA film to appear as particle defects. Control experiments in which either the plasma descum process is not used but the ALD process is performed and the PMMA film is removed could be performed to determine if particles are left on the substrate in the absence of the use of the plasma processing step. An absence of particles in such a case would indicate that plasma induced pinholing could indeed be a source of such particle defect generation. Also, experiments in which thicker PMMA films are used and in which the plasma descum time is varied could be performed, and if plasma induced pinholing is a problem it might be expected that the number of defects

would be reduced as the film thickness is increased or as the plasma process time is decreased.

5.4 Conclusions

In this section, patterning of PMMA thin films using a heated cantilever probe has been demonstrated to produce reasonably high resolution features and these patterned polymer films have been shown to be useful as protective masking layers for area selective atomic layer deposition. Experimental results show that the vast majority of the polymer film can be easily decomposed and removed by the heated probe tip, but that a thin residue remains in the patterned feature that prevents ALD in the written features. It is shown that a simple and quick O₂ plasma descum etch can be used to clean the residue from the written features and thus permit areas selective atomic layer deposition.

5.5 References

- [1] Hua, Yueming; Saxena, Shubham; Henderson, Clifford L.; King, William P. Nanoscale thermal lithography by local polymer decomposition using a heated atomic force microscope cantilever tip. *Journal of Micro/Nanolithography, MEMS, and MOEMS* (2007), 6(2), 023012/1-023012/6
- [2] Sinha, Ashwini; Hess, Dennis W.; Henderson, Clifford L. Area-Selective ALD of Titanium Dioxide Using Lithographically Defined Poly(methyl methacrylate) Films. *Journal of the Electrochemical Society* (2006), 153(5), G465-G469
- [3] Sinha, Ashwini; Hess, Dennis W.; Henderson, Clifford L., Area selective atomic layer deposition of titanium dioxide: effect of precursor chemistry, *Journal of Vacuum Science & Technology, B: Microelectronics and Nanometer Structures--Processing, Measurement, and Phenomena* (2006), 24(6), 2523-2532
- [4] Sinha, Ashwini; Hess, Dennis W.; Henderson, Clifford L., A top surface imaging method using area selective ALD on chemically amplified polymer photoresist films, *Electrochemical and Solid-State Letters* (2006), 9(11), G330-G333

- [5] Markku Leskel and Mikko Ritala, Atomic Layer Deposition Chemistry: Recent Developments and Future Challenges, *Angew. Chem. Int. Ed.* 2003, 42, 5548 – 5554
- [6] Booyong S. Lim, Antti Bahtu, Roy G. Gordon, Atomic layer deposition of transition metals, *nature materials* (2003) 2 :749-754
- [7] Magonov, S. N.; Elings, V.; Whangbo, M.-H., Phase imaging and stiffness in tapping-mode atomic force microscopy, *Surface Science* (1997), 375(2/3), L385-L391
- [8] Ritala, Mikko; Leskela, Markku; Niinisto, Lauri; Haussalo, Pekka. Titanium isopropoxide as a precursor in atomic layer epitaxy of titanium dioxide thin films. *Chemistry of Materials* (1993), 5(8), 1174-81.
- [9] Jaan Aarik, Aleks Aidla, Teet Uustare, Mikko Ritala, Markku Leskela, Titanium isopropoxide as a precursor for atomic layer deposition: characterization of titanium dioxide growth process, *Applied Surface Science* 161 2000 385–395

CHAPTER 6

THERMAL PROBE SURFACE MODIFICATION AND IMAGING

6.1 Introduction and Background

In polymer thermal decomposition based nano-lithography, the feature size also limited by the tip shape. Usually, the cantilever tip is cone shaped with a half angle of about 30° . Even if the tip has a very small radius of curvature, i.e. 15 nm; in the thermal decomposition method when the tip is fully penetrated into the film with a film thickness of 100 nm, the minimum feature dimension on the top surface will be over 115 nm (see Figure 6-1). This characteristic determines the minimum feature size we can make out of this method.

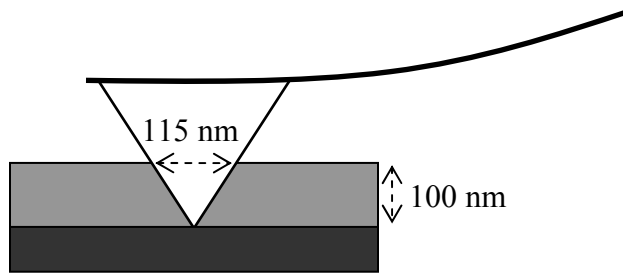


Figure 6-1. Resolution limitation of thermal decomposition method

One way to overcome this limitation is generate some pattern on the surface of the polymer surface, then via some chemical or physical process to transfer the surface pattern into the entire film thickness. One of these kinds of processes is top surface imaging (TSI). Back in 80's in microlithography industry, people use photolithography to generate very shallow patterns on the photoresist surface, and use silylation to enhance the etch resistance of the exposed area; then use plasma etching to transfer the surface pattern into the entire film thickness. [1,2,3,4]

In the case of thermal probe lithography, because the thermal penetration depth is very small, only 2-3 nm depth of material on the surface can be chemically modified.

This amount of material is not enough to make a good etch barrier for dry etch after silylation. So other alternative method should be used to transfer the surface pattern. Atomic layer deposition (ALD) is an additive method which only needs a monolayer of functional group as the seed layer. People have successfully deposited tens of nanometer of TiO_2 on a silicon surface patterned with SAMs. [5] Laterly, Ashwini also showed that TiO_2 can be selectively deposited on photolithography patterned polymer films, which contains hydroxyl group in exposed area. [6] These previous literature reports shows that selective ALD will be a good method for deposition of a etch barrier on a thermal probe generated surface pattern on polymer surface.

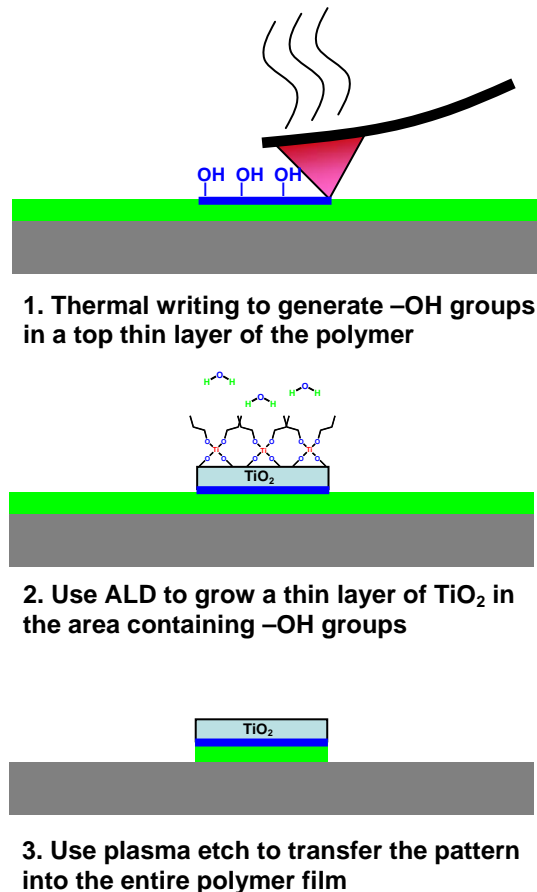


Figure 6-2 Cartoon shows thermal probe surface modification and imaging

TiO₂ is one of the most investigated materials which can be deposited by ALD. [7] In ALD of TiO₂, hydroxyl groups are normally used as the seed for deposition. In order to selectively deposit TiO₂ on the thermally pattern polymer surface, the easiest way is to use the heated cantilever tip write on a polymer surface to thermally generate hydroxyl groups in the thermal written area. Then use ALD to deposit a few nanometers of TiO₂ in thermal written area which contains hydroxyl groups. TiO₂ should have much higher resistance to O₂ plasma than polymers do, so by using an O₂ plasma dry etching, the surface pattern can be transferred into the entire film thickness (see Figure 6-2).

6.2 Material Synthesis and Characterization

The most important characteristic of the material used for this application will be that hydroxyl groups can be thermally generated on the surface. According to previous experience with thermal decomposition, in order to chemically modify the polymer surface with a reasonable speed, the hydroxyl groups should be able to be thermally generated at a temperature below 400 °C. Also in order to keep the generated hydroxyl group on the polymer surface, the polymer backbone should be thermally stable at the thermal writing temperature. Another concern about material is that no hydroxyl group should be generated in the polymer film under ALD conditions, e.g. 150 °C for 5 hours. According the above discussions, the material used for this application should be able to generate hydroxyl groups at a temperature between 200 °C and 400 °C, and the polymer backbone should be still stable at this temperature. After considering different types of polymers, poly (hydroxyl styrene) (PHOST) was finally chosen as the starting material, because of its easy accessibility. In order to make the PHOST meets the requirements for this application, suitable protecting groups should be chosen for the phenol group in the polymer. Figure 6-3 shows the molecular structure of four different protected PHOST polymers that were synthesized in the lab. Their thermal properties were analyzed with TGA.

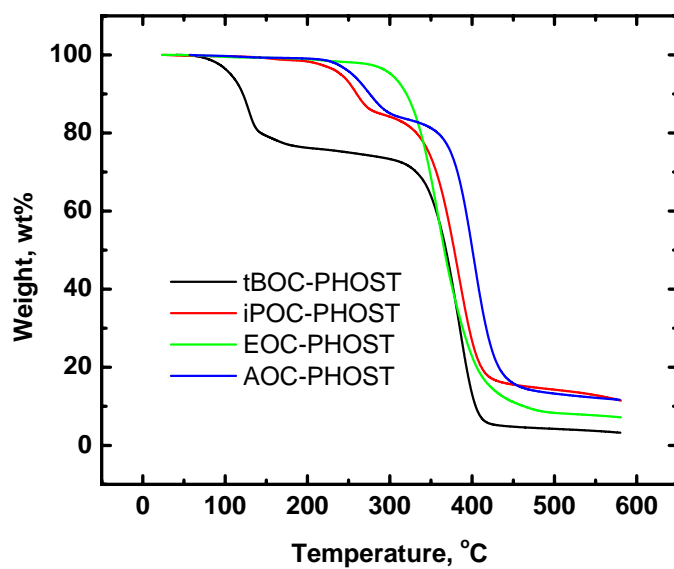
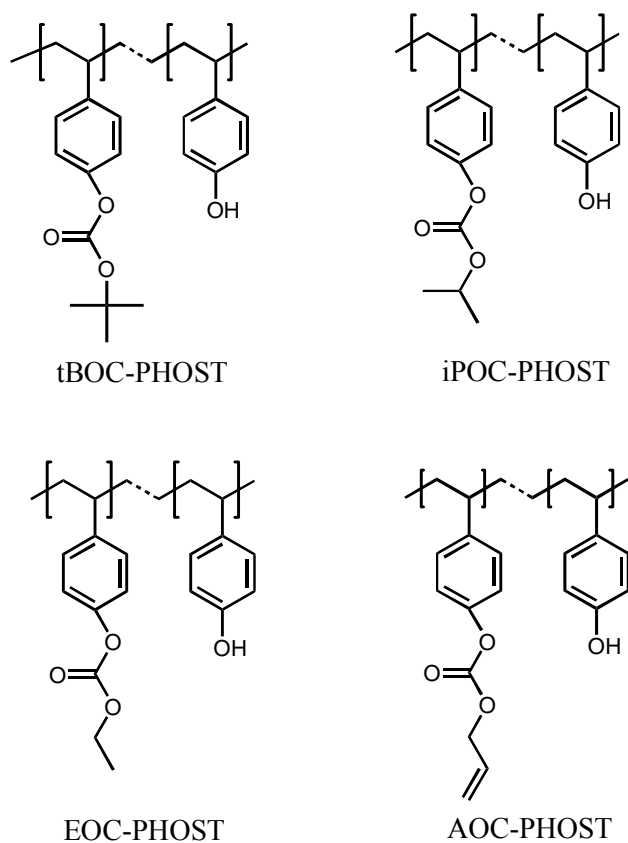


Figure 6-3. Molecular structures of four different protected PHOST polymers and their TGA data

From the TGA traces of these four materials, we can see tBOC-PHOST has two different weight loss temperature regions, and the first weight loss starts at around 120 °C, and the second weight loss starts at around 400 °C. This indicates the tBOC protecting group starts to cleave at a temperature of 120 °C which is below the ALD temperature, and the polymer backbone starts to decompose around 400 °C. So tBOC protecting group doesn't have enough thermal stability for this application. In the TGA trace, EOC-PHOST has only one weight loss temperature around 400 °C. This indicates the EOC protecting group is too thermally stable, and no hydroxyl group can be generated before the polymer backbone decomposition. So EOC-PHOST also doesn't meet the requirements for this application. From the TGA traces, we can see both iPOC-PHOST and AOC-PHOST have two stages of weight loss. The first weight loss starts around 250 °C, which corresponds to the cleavage of the protecting groups; and the second weight loss starts around 400 °C, which corresponds to the polymer backbone decomposition. The AOC-PHOST has slightly higher backbone decomposition temperature than iPOC-PHOST. This may be due to the thermally activated cross-linking of the vinyl groups in the AOC-PHOST.

The TGA analysis is conducted with a temperature of 10 °C/min. During ALD, the material will be heated to 150 °C for about 5 hours. To make sure these materials will not generate hydroxyl groups under ALD conditions, isothermal TGA analysis was conducted for these two materials, and the TGA traces are shown in Figure 6-4 and Figure 6-5. From the isothermal TGAs, we can see that both materials are thermally stable at 150 °C for one hour. The slight weight loss at this temperature for both materials may be due to desorption of the moisture and solvents. When the temperature was raised to 250 °C, both materials start to lose weight quickly, and then the weight keeps almost constant. This indicates the protecting groups can be cleaved at this temperature, but the polymer backbone stays untouched. When the temperature was further raised to 350 °C,

both materials start to loose weight significantly, this corresponds to the polymer backbone decomposition.

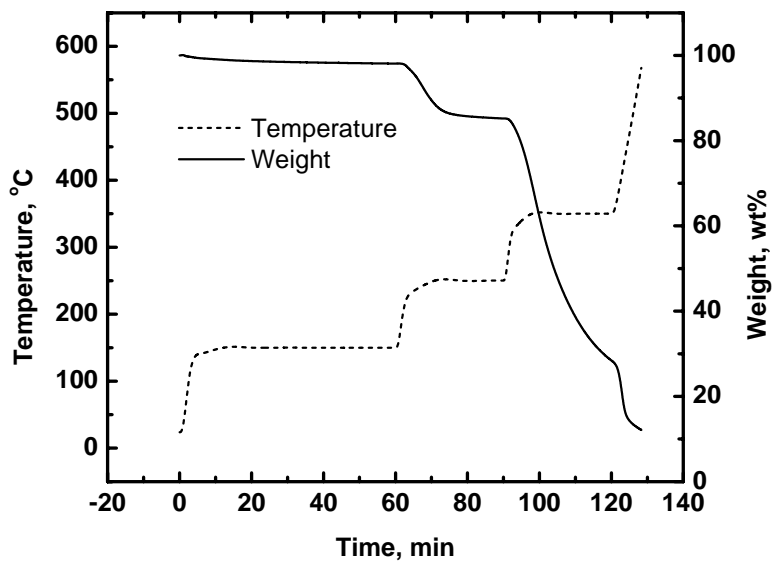


Figure 6-4. Iso-TGA of iPOC-PHOST

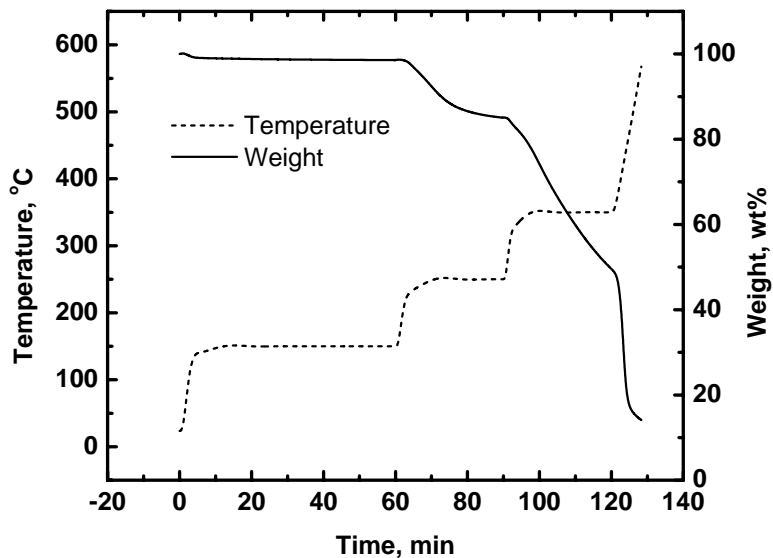


Figure 6-5. Isothermal TGA of AOC-PHOST

The iso-thermal TGA results further confirm that iPOC-PHOST and AOC-PHOST have the right thermal properties for this application.

People have done detailed investigation of the thermal decomposition of carbonate groups. Thermolytic cleavage of carbonate groups is known to proceed by syn-elimination, as generally depicted in Fig. 6-6 [8]

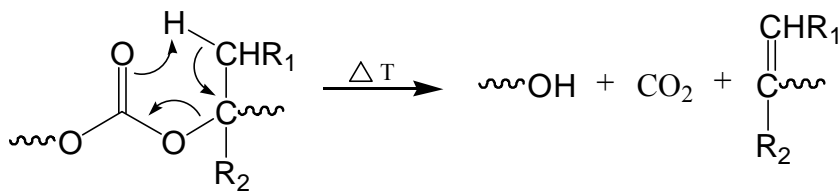


Figure 6-6. Illustration of syn-elimination

Martele [9] used detailed TGA-GC-MS to analyze the decomposition products of various carbonate groups, and the results confirmed the above thermolytic cleavage mechanism. One of the carbonate groups Martele analyzed is iso-butyloxycarbonyl group. According to their report, the main decomposition product is 1-butene, carbon dioxide, and alcohol.

According to these literature results, we believe the decomposition of the iPOC groups undergoes the same mechanism as illustrated in Figure 6-6. And the decomposition products are propylene, carbon dioxide, and PHOST polymer.

The thermolytic cleavage of the AOC group is expected to be somewhat different from the iPOC group. According to Griesbaum's work of pyrolysis of propylene [10], the formed allyl radicals can either lose hydrogen to form allene or add to the double bond of propylene to form oligomers and polymers.

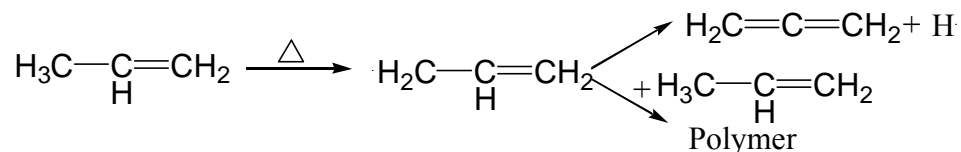


Figure 6-7. Pyrolysis of propylene

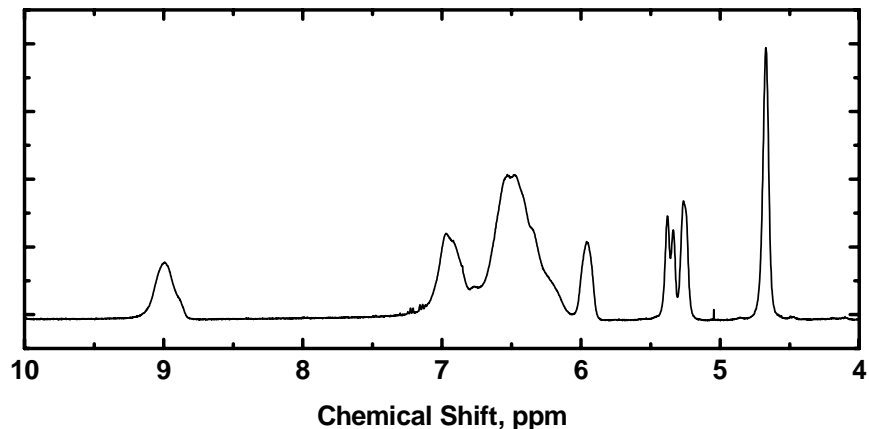


Figure 6-8. ^1H NMR of partial protected AOC-PHOST

In the case of the deprotection of the AOC group, we believe the reaction can also go two different ways after the elimination of carbon dioxide and formation of allyl radical. One way is the allyl radical loses a proton, and forms allene; and the other way is allyl radical attaches to other AOC groups to form longer side groups. In the first case, since the allene and carbon dioxide are volatile, the total weight will be 41%; but in the second case, the weight loss will be less and in the extreme would only be due to the elimination of carbon dioxide (i.e. the weight loss would only be 22% in this extreme case). According to the isothermal TGA data of the AOC-PHOST, the first weight loss, which is due to the deprotection of AOC group, is about 16%. According to the ^1H NMR of this AOC-PHOST, the protection degree of AOC group is about 40%. Complete deprotection of AOC group in this material with formation of allene will give 16.4% of

total weight loss; this value is very close to the weight loss observed in the TGA results. According to this, we believe the deprotection of AOC mainly follows the pathway that leads to formation of allene and carbon dioxide.

Another concern for this application is that the material used in thermal writing should have enough mechanical strength to prevent the tip penetrating into the film, and let the heated tip stays on the polymer surface. According to previously experience in thermal decomposition method, cross-linking is a convenient way to make the polymer have enough mechanical strength even at elevated temperature.

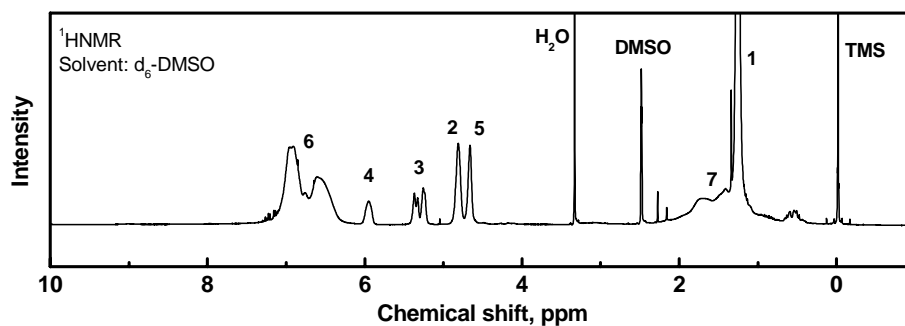
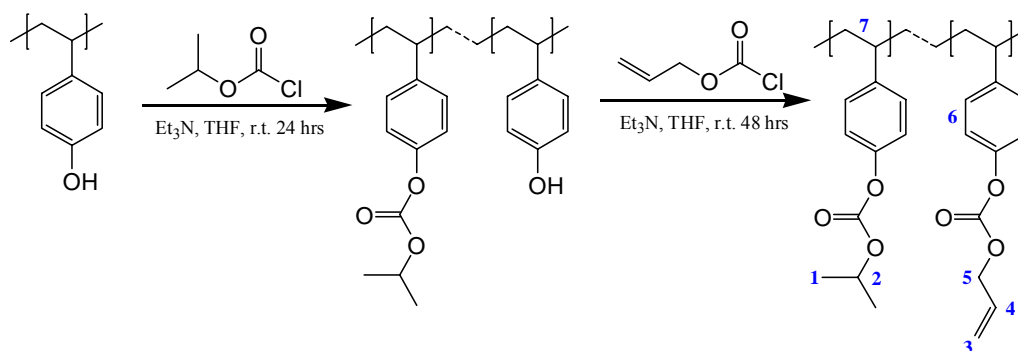


Figure 6-9. Synthetic route of iPOC-AOC-PHOST copolymer and its HNMR spectrum

AOC-PHOST contains vinyl groups, which can be used to make cross-linking between the polymer main chains. In AOC group, the carbon connected to the carbonate

group is a beta-position carbon of the vinyl group. After cross-linked, the beta-position carbon turns into a primary carbon, and this makes the carbonate group similar to EOC-PHOST, and has too high thermal stability for thermal writing. According all these concerns, a co-polymer of iPOC-PHOST and AOC-PHOST will be a perfect material for this application. Figure 6-9 shows the synthetic route for making this iPOC-AOC-PHOST material, and HNMR of this material, as well.

To make the iPOC-AOC-PHOST co-polymer, 3.6 g (30 mmol based on monomer) of poly(hydroxystyrene) (Dupont, Mw=10,000) and 3.0 g triethylamine (30 mmol) was dissolved in 30ml dry THF. The solution was stirred at 0 °C in ice bath for 5 minutes. Then 21 ml (~21mmol) isopropyl chloroformate solution (Sigma-Aldrich, ~1.0 M in toluene) was drop wise added to the polymer solution. The reaction mixture was stirred at 0 °C for 1 hour, then the slowly raise the temperature to room temperature (~25 °C), and further stirring for another 20 hours to complete the iPOC protection reaction. Then a solution of 2.4 g (20 mmol) allyl chloroformate (Sigma-Aldrich) in 30 ml dry THF was drop wise added to the reaction mixture, and the reaction mixture was further stirred at room temperature for another 20 hours. After the reaction is completed, the formed the triethylamine chloride salt (not soluble in THF) was filtered away, and the solvents was removed using rotary evaporator under vacuum. The polymer was re-dissolved in 15 ml acetone, and precipitated in 1000 ml DI water. White polymer powder was obtained from precipitation. The polymer was further dried under high vacuum at 45 °C for 3 hours. Total 4.58 g polymer in white powder was obtained.

Figure 6-9 shows the ¹H-NMR spectrum with peak assignments of the iPOC-AOC-PHOST co-polymer. Since the integration of the peaks in ¹H-NMR is directly proportional to the total number of the each proton, we can easily calculate the percentages of each protecting groups in the polymer from the ¹H-NMR spectrum. For this synthesized co-polymer, the calculated percentages of protecting groups are iPOC is about 70%, and AOC is about 30%. No free hydroxyl group, which should have a single

peak at about 9.0 ppm, can be observed in the spectrum. This means hydroxyl groups in starting PHOST polymer were completely protected.

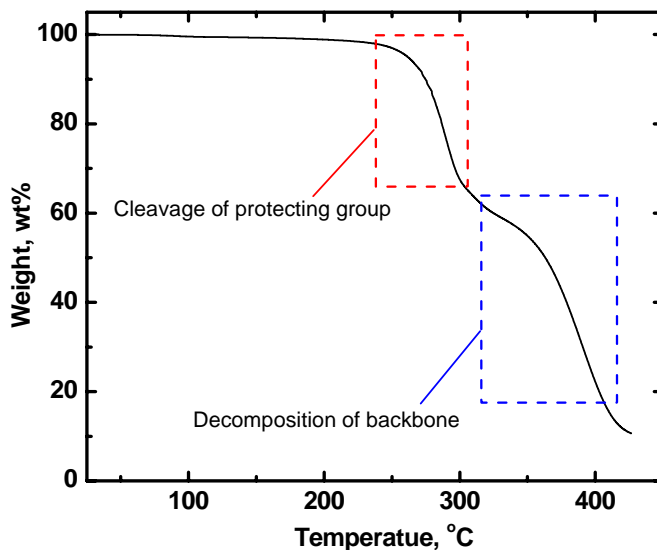


Figure 6-10. TGA trace of iPOC-AOC-PHOST copolymer

The fully protected iPOC-AOC-PHOST co-polymer was further analyzed with TGA at a constant ramping rate (Figure 6-10). The TGA trace clearly shows 2-stage decomposition. The first stage decomposition occurs between 230 °C – 300 °C, and it contributes to about 40wt% of weight loss. And the second stage decomposition occurs after 300 °C. According to previous discussion, the first stage weight loss should belong to cleavage of the protecting groups.

Molecular weight of PHOST repeat unit is $M = 120.15$ g/mol, molecular weight of AOC-PHOST repeat unit is $M = 204.22$ g/mol, and molecular weight of iPOC-PHOST repeat unit is $M = 206.24$ g/mol. The average molecular weight of repeat unit of the copolymer with 30% AOC and 70% iPOC protecting groups should be $M = 205.63$ g/mol. If all the protecting groups (iPOC and AOC) are cleaved during the first stage decomposition, the theoretical weight loss should be $(1-120.15/205.63)*100\text{wt}\% = 41.6$

wt%, which is very consistent with the measured first stage weight loss in experimental TGA.

Polymer thin film samples were prepared by spin coating, followed by UV curing. First, 300 mg of iPOC-AOC-PHOST was dissolved in 2.7 g PGMEA to make a solution for spin coating. 12 mg of Irgacure 651 was also added to the solution as the photo initiator for cross-linking. Before spin coating, the solution was further filtered with 0.2 μm syringe filter to remove particles. Thin polymer films were prepared by spin coating this solution on a fresh cleaned substrate at 2000 rpm for 45 sec.

For cross-linking, the prepared film was flood exposed by 248nm UV light with a intensity of 1.0 mW/cm^2 for 90 min. During curing, the sample was protected under N₂ environment, and the sample was heated to 100 °C.

Figure 6-11 show the FT-IR spectrums of a cured iPOC-AOC-PHOST film after different post processing. In the FT-IR spectrum of the cured sample, the strong absorption at 1750 cm^{-1} belongs to the C=O stretch, the strong absorption at 1250 cm^{-1} belongs to O-C-O stretch, and the medium strong absorption at 1500 cm^{-1} belongs to the benzene ring mode. We can't see any absorption around 3500 cm^{-1} . This indicates that the protecting groups are stable under curing conditions, and no hydroxyl groups were generated in the curing process. After baked at 160 °C in air for 3 hours, the film has the exact same FT-IR spectrum as before baking. This indicates that under this condition, there was no carbonate group in the material cleavage, and no hydroxyl groups were generated. So the material should have enough thermal stability under ALD conditions. But when baked at 250 °C for 45 minutes, the absorption at 1500 cm^{-1} didn't change, but the absorption at 1750 cm^{-1} and 1250 cm^{-1} decreased significantly. This decreasing is due to the cleavage of the iPOC group at 250 °C. According to the iso-thermal TGA of iPOC-PHOST and AOC-PHOST, the deprotection will complete within 20 minutes at 250 °C. But there is still some absorption at 1750 cm^{-1} and 1250 cm^{-1} after 45 minutes baking at 250 °C. This indicates there are still some carbonate groups left, but they are neither

iPOC nor AOC. This is true, because after curing, the original AOC group turns into another carbonate group, which should have higher thermal stability. This also proves that material is cross-linked.

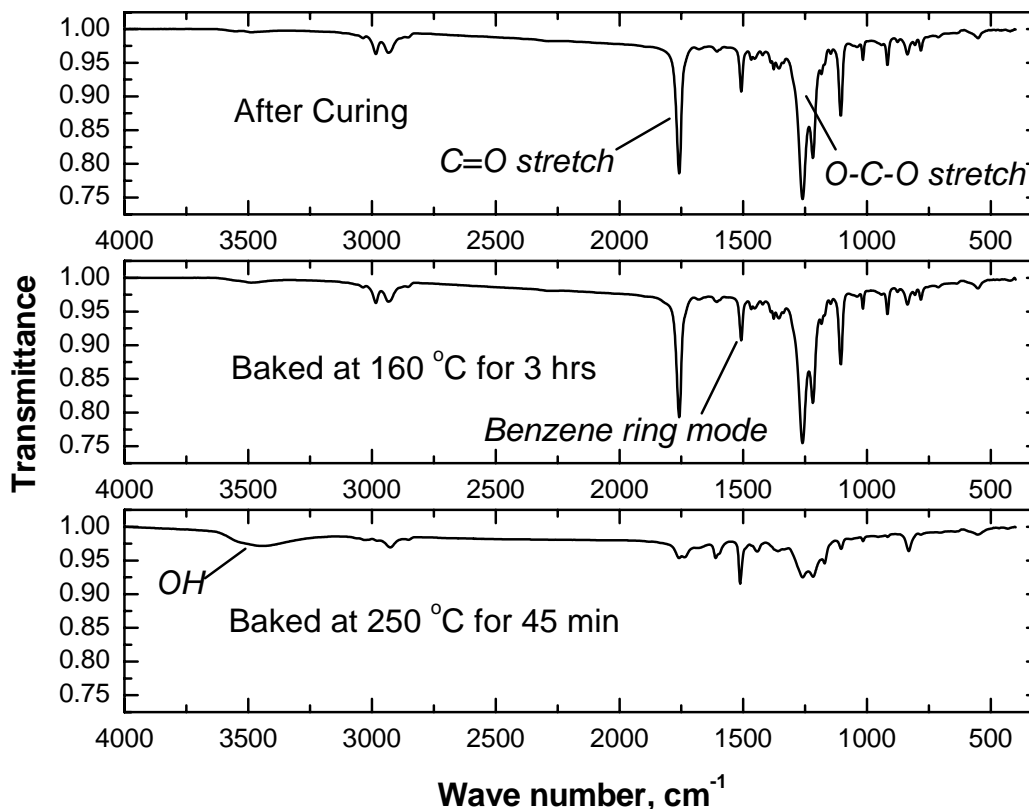


Figure 6-11. FT-IR of cured iPOC-AOC-PHOST copolymer under different conditions

According to FT-IR spectrum, AOC and iPOC should be fairly stable after 248 UV exposure. But is still possible some small amount of hydroxyl group, especially on surface, due to cleavage of protecting groups or UV oxidation.[11] ALD of TiO₂ with Titanium isopropyl oxide and water as the precursors are very sensitive to hydroxyl groups on the substrate surface. So it is very important to eliminate any hydroxyl group on the surface. For this purpose, a silylation process was used after curing to protect that small amount of hydroxyl group on the surface. Figure 6-12 shows a simple setup for a gas phase silylation. Nitrogen gas bubbling in HMDS, then enter into a funnel, which is

upside down covered on a hot plate, and finally vented into environment. A sample for silylation was put between the funnel and the hotplate. The whole setup was placed in fume hood.

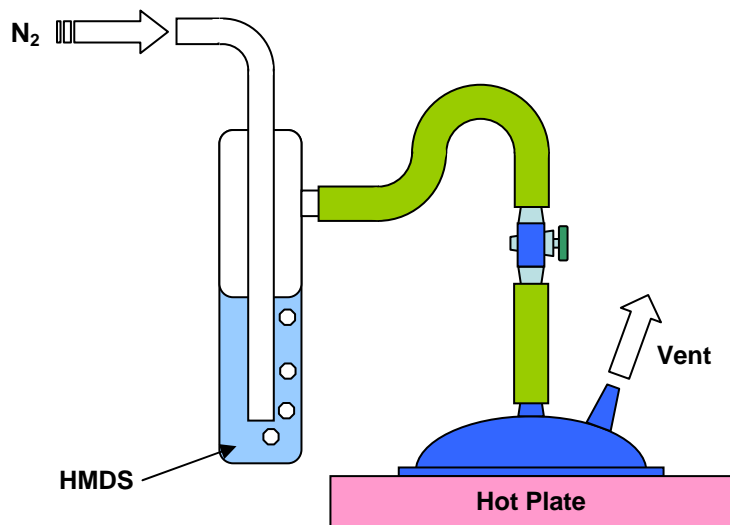


Figure 6-12. Equipment setup for gas-phase HMDS silylation

Table 6-1. Contact angle measurements

Sample	CA/degree	STD/degree
iPOC-AOC1	80.4	0.8
iPOC-AOC2	82.5	0.9
iPOC-AOC3	62.3	2.2
AOC-PHOST	72.1	3.0
PHOST	54.1	1.6

* iPOC-AOC1: UV Cured

* iPOC-AOC2: HMDS treated

* iPOC-AOC3: 250 °C baked

Table 6-1 lists water contact angle measurements of this sample, as well as some reference samples. We can see, after HMDS silylation, the contact angle slightly increased from 80.4° to 82.5°, which indicates that some surface hydroxyl groups were further protected with trimethyl silane group. And after baked at 250 °C, the contact angle decreased significantly down to 62.3°. This is due to the cleavage of the iPOC group and

generation of hydroxyl group. And this contact angle value is between the contact angle of a cured fully protected AOC-PHOST (72.1°) and an un-protected PHOST (54.1°).

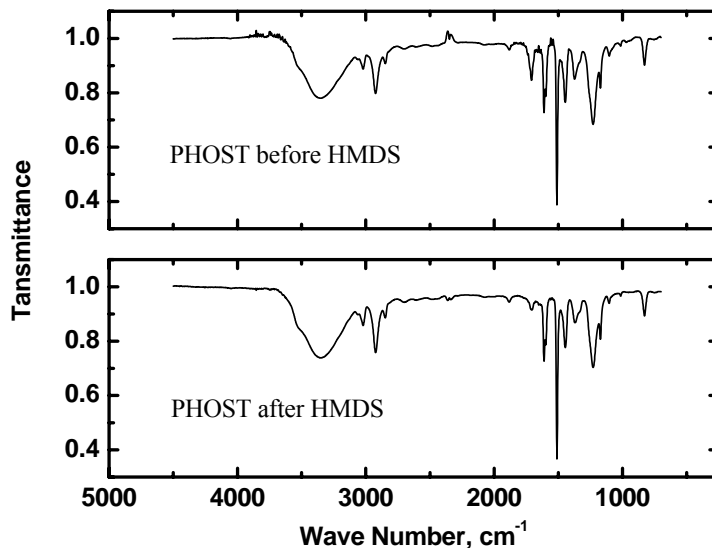


Figure 6-13. FT-IR of PHOST before and after HMDS silylation

FT-IR spectrums of a PHOST film before and after a same silylation process, which was used to protect the surface hydroxyl group of a cured iPOC-AOC-PHOST sample, are shown in Figure 6-13. We can't see any big difference between the PHOST IR spectrums before and after the silylation process. This indicated the silylation reaction only occurs at the surface of the polymer film.

The thermal stability of the silylated PHOST was further investigated using contact angle. Figure 6-14 shows four contact angle measurements of a PHOST film after a series of processes. After silylation, the water contact angle of PHOST increased from 54.1° to 100.5°. And there is no any noticeable decrease in contact angle after the sample was heated at 140 °C with 0% humidity for one hour, followed by another hour heating at 140 °C with 100% humidity. This experiment proves that the silylated hydroxyl group show be stable under ALD conditions.

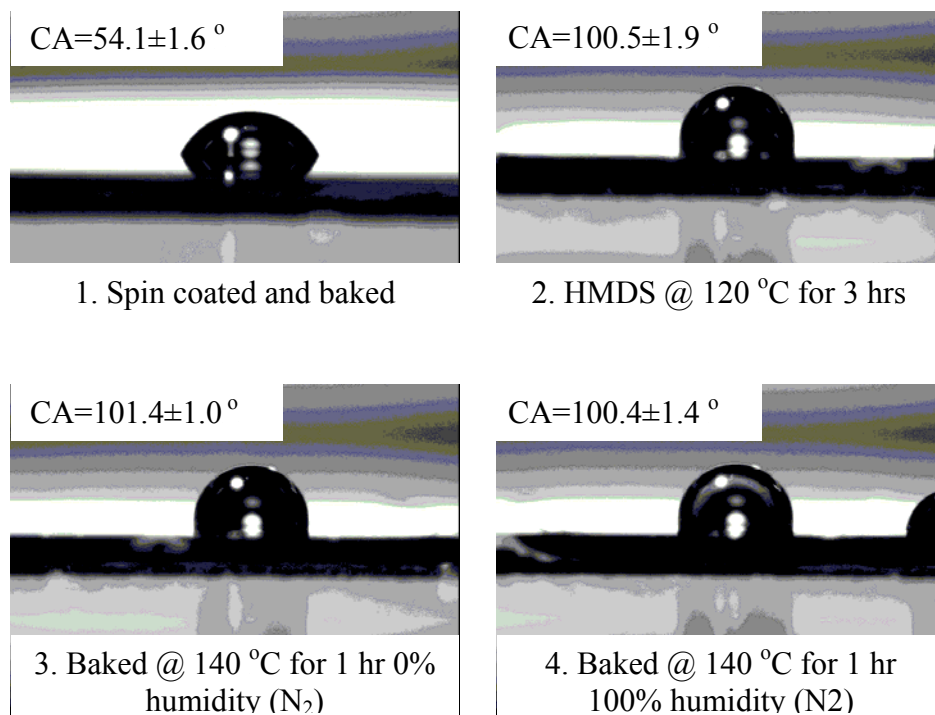


Figure 6-14. Contact angle measurement of PHOST under different conditions

6.3 ALD Top Surface Imaging of ThAFM Pattern

6.3.1 ALD on Bulk Sample (XPS)

The area selective ALD of TiO₂ with Titanium isopropyl oxide and water as the precursors was first tested on bulk samples with XPS.

An iPOC-AOC-PHOST was prepared by spin coating, followed by curing and surface silylation. Then the sample was cut into half. One half of the sample was stay the same, and the other half of the sample was baked at 250 °C for 45 minutes to cleave the iPOC protecting group and generate hydroxyl group. Both of those two halves of the sample were put into an ALD reactor at the same time to deposit TiO₂. The ALD temperature was 140 °C. A typical ALD cycle consisted of: (1) a 2 sec TiIP pulse, (2) a 30 sec N₂ purge, (3) a 2 sec DI water pulse, and (4) a 30 sec N₂ purge, for 100 cycles.

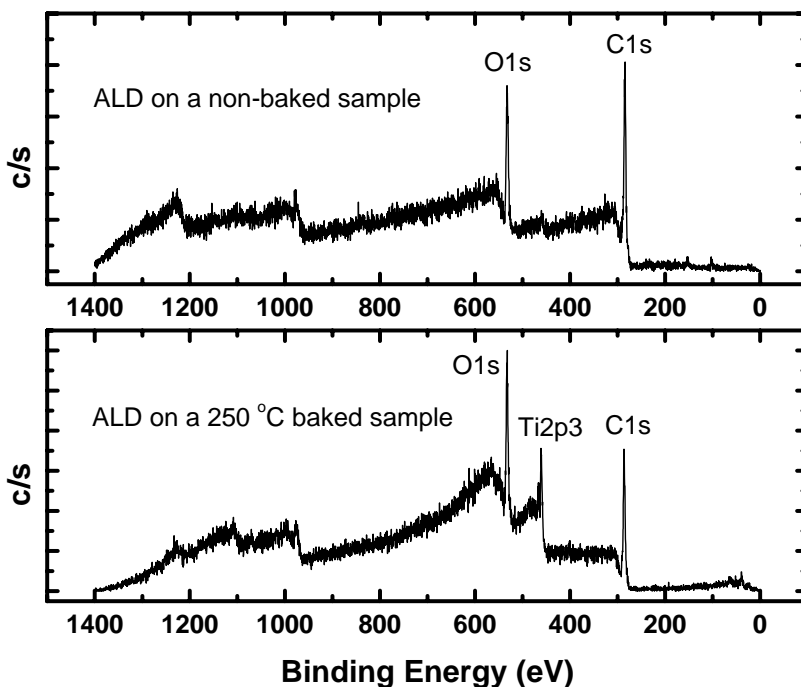


Figure 6-15. XPS spectra of iPOC-AOC-PHOST samples after ALD deposition of TiO_2

Figure 6-15 shows the X-ray photoelectron (XPS) survey scan spectra of those two halves of iPOC-AOC-PHOST samples after ALD deposition of TiO_2 . We can see, for the non-baked half of the sample, we can only see two big peaks which belong to O1s and C1s. There might be a very tiny peak around 460 eV which belongs to Ti2ps. But for the baked half of the sample, we can clearly see three big peaks, which are O1s, C1s, and Ti2p3. The XPS shows that there was TiO_2 deposited on the baked half of the sample, and almost no deposition on the non-baked half of the sample.

High energy resolution scans were also done to calculate the atomic concentration of each element on the surface, and the results are list in Table 6-2.

Table 6-2. Calculated atomic concentration from XPS spectrum

Sample	C	O	Ti
Non-baked	73.1	26.0	0.9
Baked	59.6	32.8	7.6

We can see, slight amount (0.9%) of TiO_2 was deposited on the surface. The mole ratio of carbon and oxygen in the non-baked polymer film after ALD was 73.1:24.2, after subtracting the oxygen belongs to TiO_2 . Theoretical, for a full protected iPOC-AOC-PHOST polymer, the mole ratio of carbon and oxygen in the non-baked should be 4:1. But considering under routine work conditions, where the surface is a mixture of contamination and expected material, the accuracy ranges from 80-90% of the value reported in atom % values, and only the major peaks are used for atomic concentration calculation [12], the measured atomic concentrations are close to the theoretical value.

For the baked sample, XPS show there are 7.6% of Ti atoms on the surface, which is much high than that for non-baked sample. This clearly shows the selectivity of the TiO_2 deposition on these two different sample surfaces.

Theoretically, in a baked iPOC-AOC-PHOST polymer sample the mole ratio of carbon and oxygen is 86.23: 13.77, but the XPS measured concentration is 59.6% and 32.8% for carbon and oxygen, respectively. Then 23.8% of total atoms should be the oxygen in TiO_2 , and there should be 11.9% of Ti atoms in the surface. The calculated Ti concentration from the XPS is 7.6%, which is about 64% of the expected value. But considering the quantitative accuracy for the weaker XPS signals, that have peak intensities 10-20% of the strongest signal, are only 60-80% of the true value, we can see the results are acceptable.

The XPS of the baked sample show there are still a lot of carbon in the surface, which should belong to the polymer part. This suggests that the deposited TiO_2 film is very thin. Assume XPS are measuring 10nm material from the surface, and the measured Ti concentration is only about one fourth of that in pure TiO_2 , considering the higher

density of TiO_2 than polymer, then we probably only have less than 1 nm TiO_2 on the surface, and the deposition rate will be about 0.01nm/cycle. This deposition rate is same as the one measured from selective ALD in Chapter 5.

6.3.2 ALD on Thermal Patterned Sample

Thermal writing was performed on a prepared iPOC-AOC-PHOST sample. Image (1) in Figure 6-15 shows an AFM topograph image of sample surface after thermal writing. The heating temperature used for writing is 625 °C. Scan range is 5x5um with 512 pixel scan resolution and 1 line/sec scan speed. We can see that the surface in the first half micron from the bottom of the square is rougher than that in other region of the square. This is because initially, the AFM tip is hot. But after a couple of lines of scan, some contaminants (polymer or char) may stick to the tip. Because these contaminants are less conductive, and act as a thermal barrier between the hot tip and the polymer on the substrate, the temperature on the polymer surface will be less hot. Then even the tip was still hot, less or no thermal decomposition will happen. Only thermal mechanical pressing was occurring when the tip was scanning the rest of the area.

Image (2) in Figure 6-16 shows an AFM topography image of the sample after 200 cycles of ALD deposition of TiO_2 . From the cross section profile, we can see that most of the indent volume in the first half micron of the square was filled up. But 200 cycles of ALD will only deposit a couple of nanometer of TiO_2 , and it is impossible to fill that much volume. Also rest of the square area almost disappeared after ALD. The explanation of phenomena is that most of the volume loss after thermal writing is due to thermal mechanical pressing, instead of thermal decomposition. Because of the fast quenching, this depression couldn't recover by its self. Because the polymer is heavily cross-linked, this volume depression built some stress in that area. During ALD deposition, the sample was heated to 140 °C for a couple of hours, the volume depression was recovered.

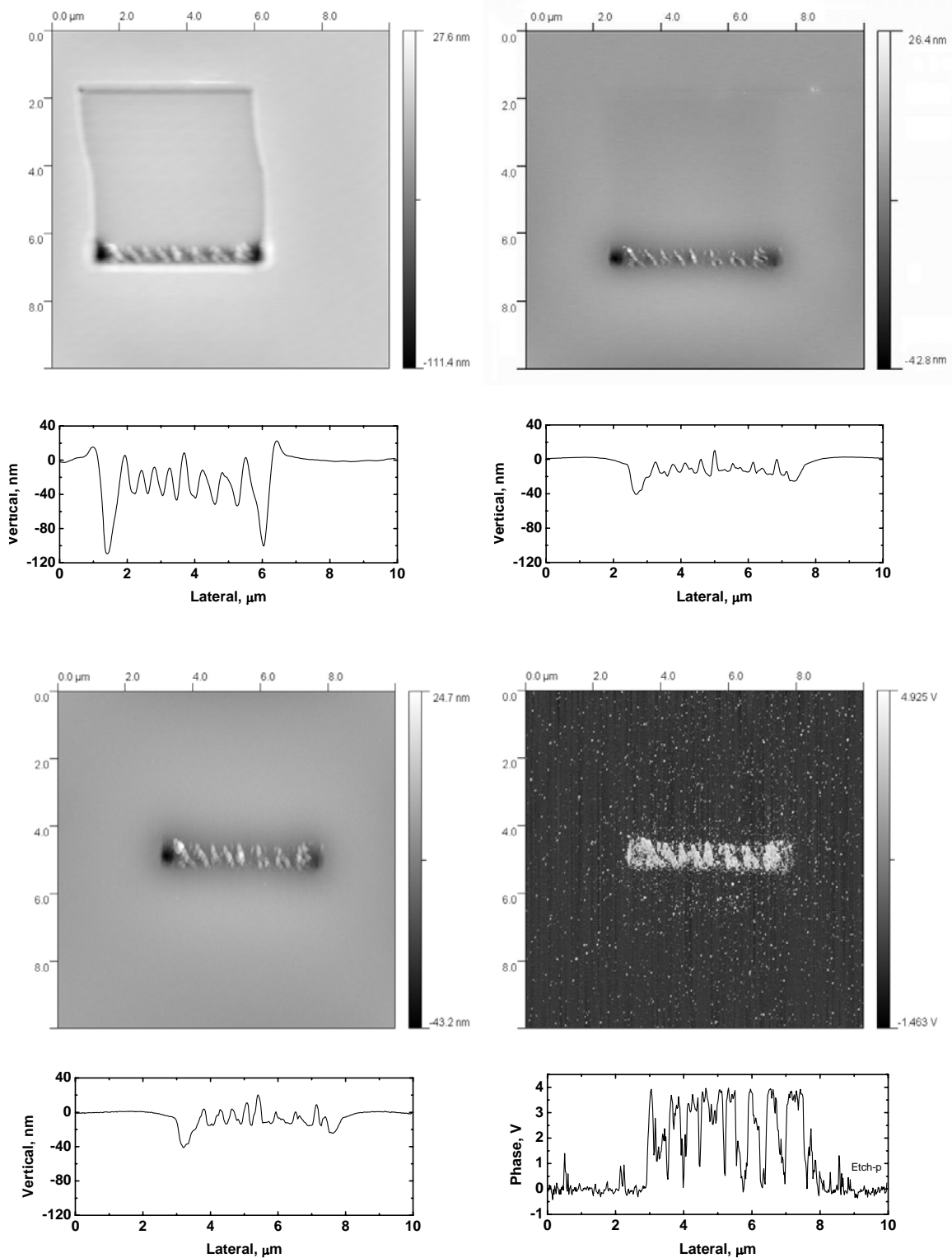


Figure 6-16. AFM topography and phase image of a line pattern after ALD deposition of TiO_2

The sample was then etched with O₂ plasma for 2 minutes. Image (3) in Figure 6-16 shows the AFM topography of the sample after etching. By comparison of the cross section profile before and after plasma etching (Figure 6-17), we can see about 10 nm more material in non-thermal written area are removed than in the thermal written area. Also, from the AFM phase image after etching (image (4)), we can see the material in the first half micron of the square has completely different phase lag than the material other area does. This indicates that they are different materials. In the first half micron area, the material should be ALD deposited TiO₂, and in other area, material should be mainly polymer.

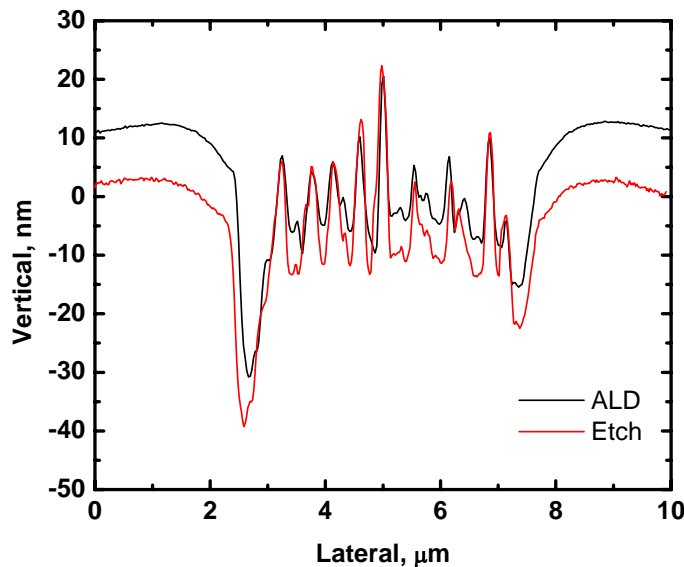


Figure 6-17. Cross section profile before and after plasma etching

We should also notice that, in the other area, the phase image is not complete uniform. There are still small amount of area, where the material has the same phase lag as TiO₂, dispersed as particles in other area. This indicates that small amount of TiO₂ was deposited in the non-thermal written area. This observation is consistent with ALD experiment on bulk sample. In previous, we observed that slightly amount of TiO₂ still

can be deposited on a non-baked sample, although much more TiO₂ can be deposited on a baked sample under same ALD conditions.

6.3.3 Tip Cleaning

From previous section, we notice that tip contamination can be a problem if we want to make a large area feature for ALD process. So a tip cleaning process is presented here to remove the contaminants and keep the heated tip working efficient.

It is possible to clean contaminants with O₂ plasma etching or other chemical methods. But this need to take the cantilever out, and put in a plasma reactor or chemicals. It will take too much time, and almost practical impossible. The cleaning process presented here is using thermal decomposition and oxidation to clean the organic contaminant on the tip. After the heat tip scan on the surface for a while, and contaminated with polymer or decomposition residues, the tip was lifted from the surface, and stay still in the air for a while. Because the tip is very hot (e.g. over 600 °C), the polymer sticking to the tip can be decomposed. Even if there is some decomposition residue remains on the tip, the surrounding air can act as oxidant to cleanly burn off the organic residue.

In Figure 6-18, two thermal writing samples are compared. The sample on the left was written as normal without a cleaning process. This means after the first line is finished, the tip move to next line immediately, and starts scanning. The sample on the right was written with the same conditions as the one on the left, except that between writing each line, the tip was lifted up, and stayed in air for one minute with heating power was on.

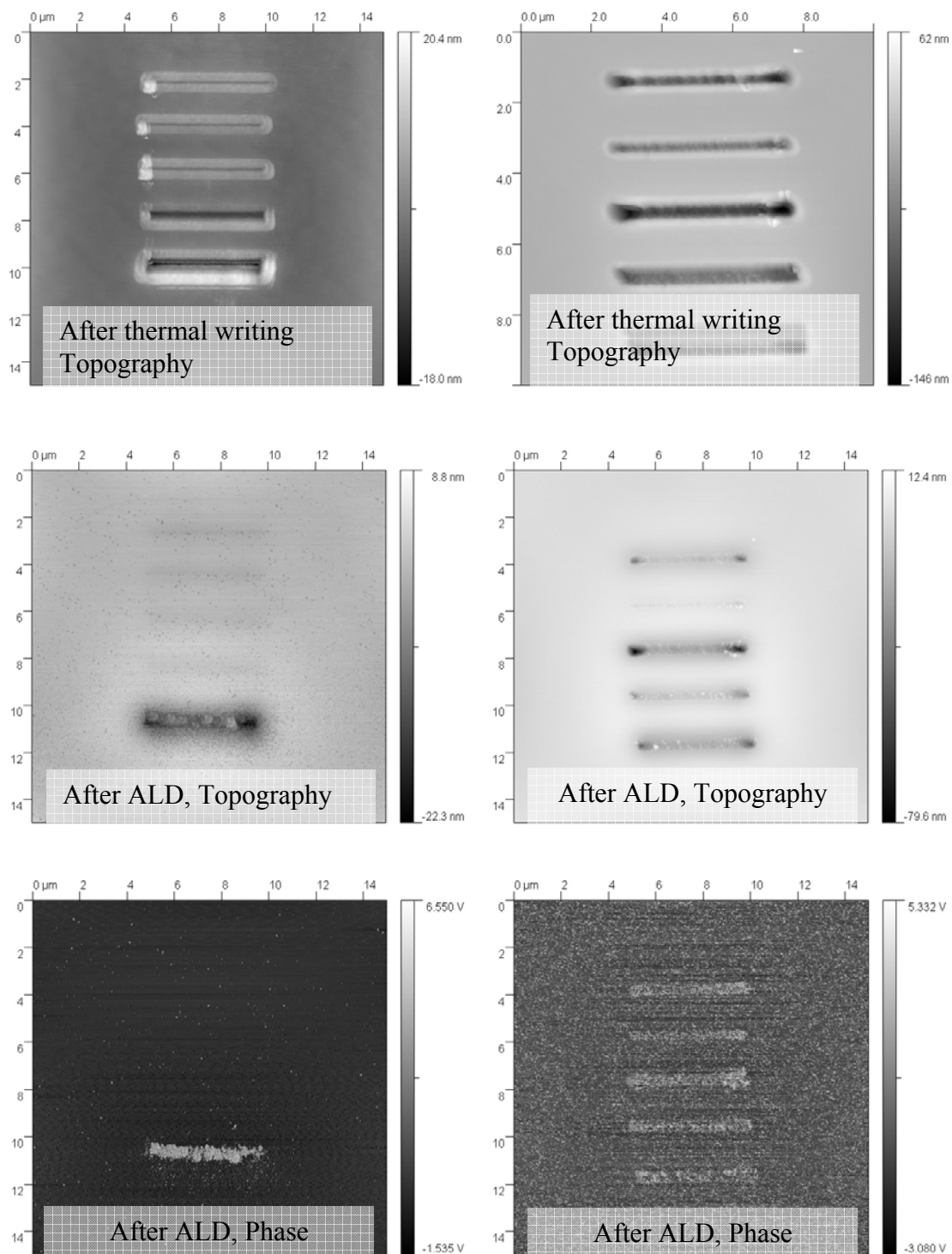


Figure 6-18. AFM topography and phase images on ALD sample: (left) without tip cleaning process; (right) with tip cleaning process

We can see, after ALD process, the sample written without cleaning process between each line, one the first line remains, and the other four lines almost disappeared. From the phase image we can also see, TiO₂ only deposited on the first line. This because when scanning the first line, the tip is initially not contaminated, and the polymer in contact with the tip can be heated to high temperature. But after finishing the first line, the tip was contaminated, so from the second line, the polymer couldn't be heated to high enough temperature any more, and the polymer was only thermal mechanically pressed. In writing the sample on the right, a cleaning process was used between each line to remove the contaminants. Then the polymer was heated to high enough temperature when the tip scanning each line. After ALD, all the line stays, and the phase image shows that TiO₂ deposited on all the five lines in the right sample. This experiment shows that the cleaning process presented here really works.

6.4 Conclusions

We reported a thermal probe based top surface imaging technology. Some new polymer materials were synthesized specifically for this application. Atomic layer deposition (ALD) of TiO₂ was used selectively deposit a thin layer of etch barrier on thermal written areas. Because of the diffusion of the precursor in the polymer, the un-thermal written area can not be completely removed by O₂ plasma etching. The results also show that the heated tip can be contaminated, and tip performance is then reduced. This issue is successfully solved by adding a tip cleaning process between thermal writing each line.

6.5 References

- [1] Somervell, M. H.; Fryer, D. S.; Osborn, B.; Patterson, K.; Byers, J.; Willson, C. G., Study of the fundamental contributions to line edge roughness in a 193 nm,

- top surface imaging system. *Journal of Vacuum Science & Technology, B: Microelectronics and Nanometer Structures* 2000, 18, (5), 2551-2559.
- [2] Coopmans, F.; Roland, B., DESIRE: a new route to submicron optical lithography. *Solid State Technology* 1987, 30, (6), 93-9.
- [3] Mutsaers, C. M. J.; Vollenbroek, F. A.; Nijssen, W. P. M.; Visser, R. J., ImRe, BIM and SUPER using patternwise esterification. *Microelectronic Engineering* 1990, 11, (1-4), 497-502.
- [4] Pierrat, C.; Tedesco, S.; Vinet, F.; Lerme, M.; Dal'Zotto, B., Positive resist image by dry etching: new dry developed positive working system for electron beam and deep ultraviolet lithography. *Journal of Vacuum Science & Technology, B: Microelectronics and Nanometer Structures* 1989, 7, (6), 1782-6.
- [5] Jae P. Lee, Yound J. Jang, and Myung M. Sung, Atomic Layer Deposition of TiO₂ Thin Films on Mixed Self-Assembled Monolayers Studied as a Function of Surface Free Energy, *Advanced functional Materials*, (2003) 13(11): 873-876
- [6] Sinha, Ashwini; Hess, Dennis W.; Henderson, Clifford L., A top surface imaging method using area selective ALD on chemically amplified polymer photoresist films, *Electrochemical and Solid-State Letters* (2006), 9(11), G330-G333
- [7] Mikko Ritala, Markku Leskela, Erja Nykfanen, Pekka Soininen and Lauri Niinisto, Growth of titanium dioxide thin films by atomic layer epitaxy, *Thin Solid Films*, 225 (1993) 288-295
- [8] Charles D. Hurd, Ford H. Blunck, The Pyrolysis of Esters, *Journal of the American Chemical Society* (1938) 60: 2419-2425
- [9] Yves Martele, Veronique Van Speybroeck, Michel Waroquier, Etienne Schacht, Thermodegradable polycarbonates: Effect of substituents on the degradation temperature, *e-Polymers* (2002) 049:1-14
- [10] K. Griesbaum, Progress in the Chemistry of Allene, *Angewandte Chemie, International Edition* (1966) 5(1): 933-946
- [11] Raanby, Bengt. Photodegradation and photo-oxidation of synthetic polymers. *Journal of Analytical and Applied Pyrolysis* (1989) 15: 237-47
- [12] Paparazzo, E. Quantitative x-ray photoelectron spectroscopy analysis of inorganic mixtures. *Journal of Vacuum Science & Technology, A: Vacuum, Surfaces, and Films* (1987), 5(4, Pt. 2), 1226-9.

CHAPTER 7

THERMAL WRITING IN SELF ASSEMBLY MONOLAYERS

(SAMS)

7.1 Introduction and Background

In previous chapters, the author presented successful thermal writing in sacrificial polymers to generate pattern using thermal decomposition. And the generated patterns can be used for patterning other functional material, e.g. TiO₂. Although the author achieved nano scale resolution, the ultimate resolution is limited by the polymer film thickness. To overcome this limitation, the author also presented a thermal probe top surface imaging (TSI) idea for patterning materials. Some positive results were obtained. But the etch selectivity for removing un-patterned polymer is limited by the diffusion of Titanium precursor. In top surface imaging process, ideally we only need a single layer of functional groups subsequent material deposition. According to this idea, self assembly monolayers (SAMs) will be the ideal material for this thermal probe nano-lithography process.

Patterning SAMs will not have the resolution limitations due to the material deformation and tip cone angle. Only the chemical properties of a monolayer of molecules need to be modified. This gives this technology potential for ultra high patterning speeds, which may be the most important issue hindering the real application of this technology. Using patterned SAMs as a seeding layer for patterning of other materials may also have the advantage that there is no need to remove the SAMs for the following processes, which will reduce the number of process steps.

This chapter will be focused on investigating the possibility of patterning SAMs, and the subsequent process to selective deposit material on the patterned SAMs. Two different types of SAMs are investigated: one the aminopropyltriethoxysilane (APTES), and the other one is 3-mercaptopropyltriethoxysilane (MPTES).

7.2 Patterning APTES SAMs

APTES is ready to deposit on a surface cover with hydroxyl groups, and form an amino group terminated SAM on the surface. Amino groups is a basic functional group, it has strong ion interaction with acidic groups, e.g. $-\text{COOH}$ group. At room temperature $-\text{COOH}$ group can bond to $-\text{NH}_2$ group with ion bonding. But this bonding can be easily broken in the presence of other strong base. When heated, amide group can be formed from $-\text{COOH}$ and $-\text{NH}_2$. The amide group is much more stable than the ion bonding between $-\text{COOH}$ and $-\text{NH}_2$. According to these, the author presents here the following idea as shown in Figure 7-1:

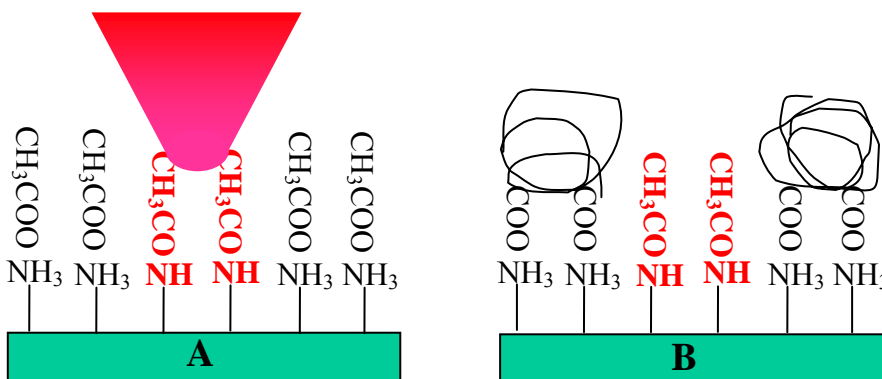


Figure 7-1. (A): Cartoon of thermal writing on APTES/Acetic acid SAM, thermal written area forms imide; (B) Cartoon shows exchange of acetic acid in the non thermal written area with poly(methacrylic acid)

After APTES SAMs are deposited on the surface, another layer of molecules containing $-\text{COOH}$ (e.g. acetic acid) is absorbed on the surface. Then a heated AFM probe is used to thermally activate the reaction to form an amide compound, and permanently bond the small molecule on the surface. Other loose bonded small molecules can be removed when the surface is treated with strong base solution. Then a heterogeneous SAM is formed on the surface, and it can be used to subsequently deposit other useful materials.

7.2.1 Experimental

The APTES SAMs were prepared as following [1]: A silicon wafer with 340nm thermal SiO_2 on the top is cleaned with Piranha solution (H_2SO_4 : H_2O_2 = 3: 1) at 100 °C for one hour, the substrate is rinsed with DI water, N_2 gun blowing dried, and then exposed to O_2 plasma for 20 minutes, and then rinsed with DI water again. This fresh cleaned substrate is immersed in a 5wt% APTES in dry toluene for 16 hours. After that, the sample was thoroughly rinsed with toluene. The as prepared APTES SAM has a water contact angle of 42.5°.

The fresh prepared APTES SAM was then immersed in a 10wt% acetic acid solution in toluene for 30 min to deposit acetic acid on the APTES SAM. Then the sample was thermally patterned using a heated cantilever tip. The cantilever heater temperature is 560 °C. After thermal writing, the sample was washed with 0.1 M $\text{NaOH}/\text{H}_2\text{O}$ solution to remove the un-reacted acetic acid. And then the sample was immersed in 5 wt% poly (methacrylic acid) solution in toluene for 30 minutes to deposit the polymer on the surface.

7.2.2 Results and Discussion

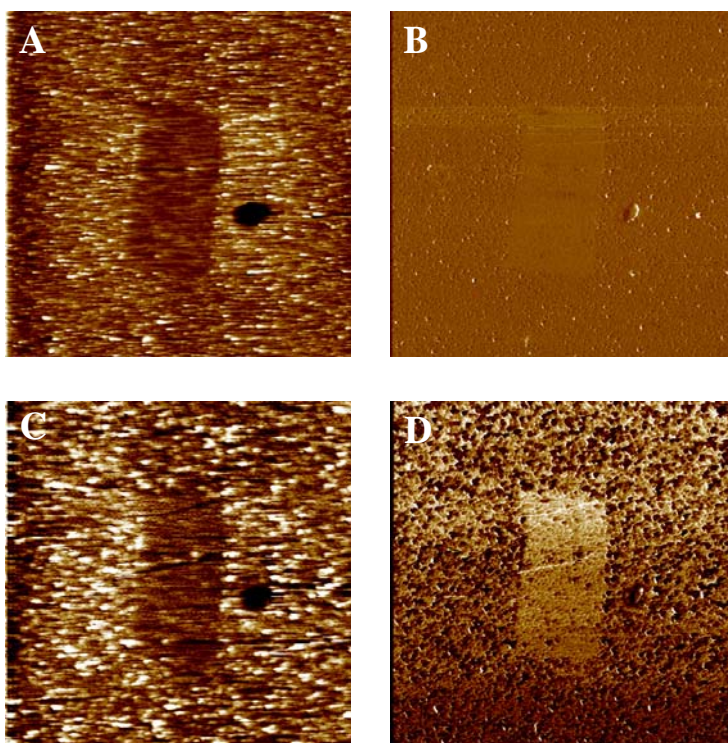


Figure 7-2. (A) AFM topography of thermal written APTES/Acetic acid; (B) AFM friction image of the same pattern; (C) AFM topography of thermal written area after acetic acid/polymer exchange; (D) AFM friction image of the same area

Figure 7-2 shows AFM topography and friction image of the APTES sample. From the image A and B we can see, after thermal writing, some material was removed from the thermal written area. But in the friction image, we can't see big difference between the thermal written area and the un-patterned area. This is because thermal writing only converted the ionic compound of the acid and amine into an amide. The surface functional group didn't change much. So there was no big friction change.

From image C and D in Figure 7-2, we can see after acid/polymer exchange, the un-patterned area became much rougher, and there is a big friction difference between the patterned area and un-patterned area. These results are consistent with the mechanism proposed previously.[2] During acid/polymer exchange, polymers particles are supposed to deposit on the un-patterned area, and this made the surface rougher. Also, not all the acid group in the polymer can be bond to the amino group on the surface. There must be some free acid group left in the polymer. But in the thermal written area, the amide compound is quite stable; it won't be affect by the exchange process. So after acid/polymer exchange process, there're complete functional group in the patterned area and the un-patterned area. In the friction image, these two areas show a big difference of the friction signal. This is consistent with our expectation for the exchange process.

7.3 Thermal Writing on MPTES SAMs

It is well known that thiol (-SH) group has strong bonding force with metal Gold. If we can thermally generate thiol functional groups on a sample surface, then these thiol groups can be used to guide selectively deposition of gold nano particles (AuNPs).[3] For this purpose, a protected MPTES SAM is the ideal choice for this application. Figure 7-3 shows the proposed mechanism for this process.

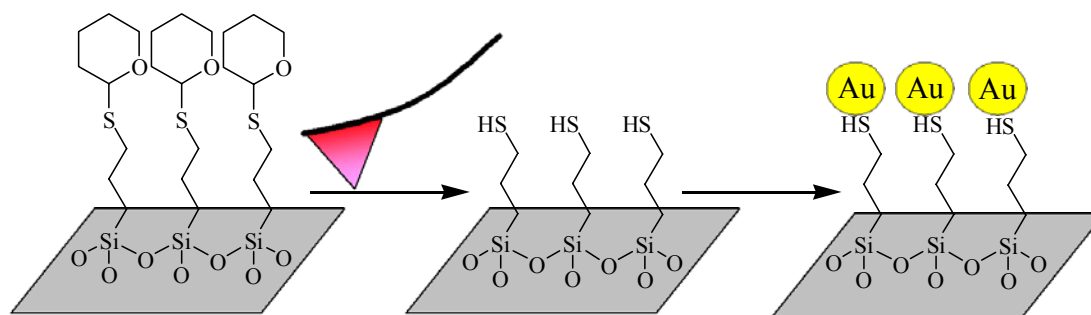


Figure 7-3. Cartoon of thermal writing on THP-MPTES SAMs and deposition gold nano-particles.

7.3.1 Material Synthesis and SAMs Preparation

THP is widely used in photoresist chemistry as a protecting group, and it can be thermally deprotected. In this work, a THP protect MPTES chemical was used.

THP protected 3-mercaptopropyltriethoxysilane (MPTES) is synthesized by one step reaction of 3, 4-Dihydro-2H-pyran with MPTES with acid as the catalyst (Figure 7-4). [4] Pyridinium p-toluenesulfonate (PPTS) was chosen as the catalyst, because it is mild and efficient, and it can be used in complex system with sensitive functional groups.

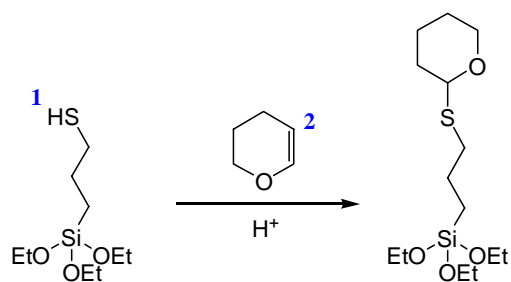


Figure 7-4. synthetic route for make THP-MPTES

7.3.1.1 Synthesis of PPTS

The PPTS used in this work is synthesized by the author by following the procedure reported in literature [5]. 5.7 g of p-toluenesulfonic acid monohydrate was added to 12.1 ml pyridine. The mixture was stirred at room temperature for 20 minutes. Then the excess amount of pyridine was evaporated. 10 ml of Acetone was added to the raw product, and heated to about 60 °C to dissolve the raw product. Then slowly cool it down to let the product re-crystallize. The re-crystallized product was obtained by filtration, and further washed with Acetone. Then the product was vacuum dried at room temperature for 3 hours. Finally, 5.0 g (yield: 66.2%) of dried crystalline product was obtained. The structure of the synthesized PPTS was further checked with $^1\text{H-NMR}$ (Figure 7-3), and the spectrum has a perfect match with the one obtained from Sigma-Aldrich database.

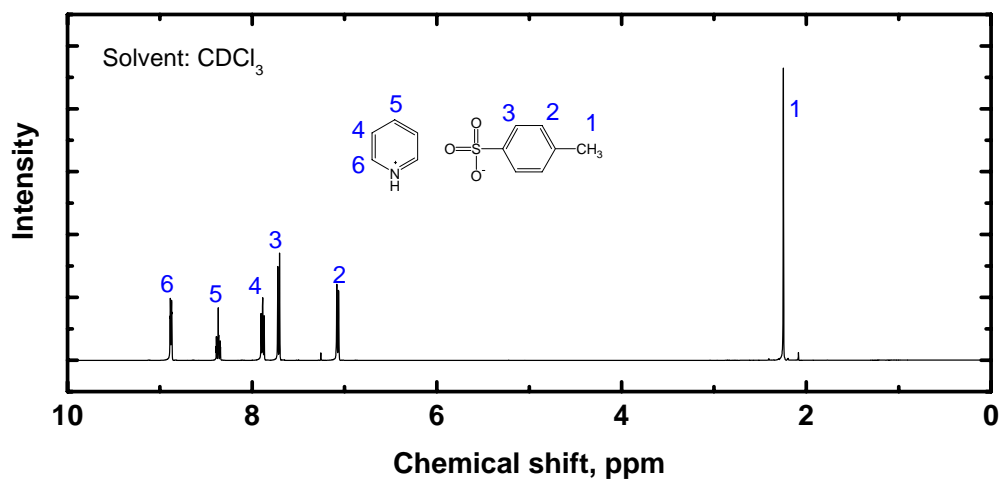


Figure 7-5. $^1\text{H-NMR}$ of synthesized PPTS

7.3.1.2 Synthesis of THP-MPTES

The reaction of 3, 4-Dihydro-2H-pyran with MPTES was first checked with in-situ $^1\text{H-NMR}$ analysis. 50 mg (0.2 mmol) of MPTES, 34 mg (0.3mmol), and 5.0 mg (0.02 mmol) PPTS was dissolved in 1.0 ml CDCl_3 . The solution was put into a NMR tube, and stored at room temperature. $^1\text{H-NMR}$ spectrums were obtained on at different times for the same sample (Figure 7-4). From the spectrums we can see, after 96 hours of reaction, almost all the $-\text{SH}$ peaks disappeared, and a peak belonging to a proton on the double bond in 3, 4-Dihydro-2H-pyran reduced to about 1/3 of its initial value. This indicates that after about 96 hours, most of the $-\text{SH}$ groups were protected with THP groups.

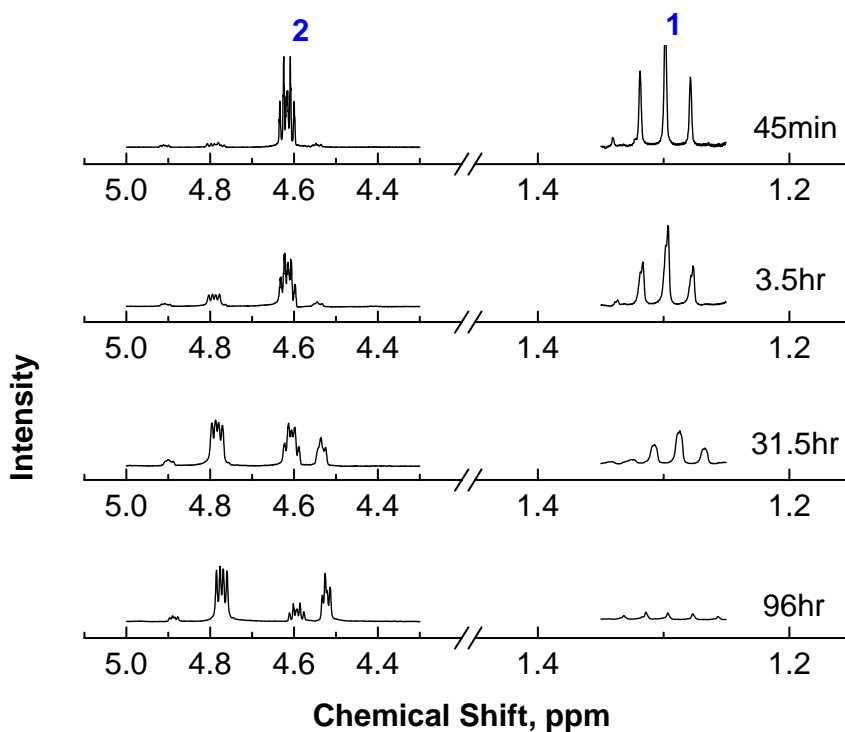


Figure 7-6. $^1\text{H-NMR}$ of the reaction mixture at different time

7.3.1.3 Wafer Cleaning:

A silicon wafer was first immersed in a Piranha solution (3:7 of H₂O₂: H₂SO₄) at 100 °C for 10 minutes. Then the substrate was further cleaned with RCA-2 process (1:1:5 of H₂O₂:NH₄OH:H₂O at 80 °C) for 10 minutes. Then the fresh cleaned substrate was stored in DI water for further use.

7.3.1.4 THP-MPTES SAMs Preparation

To prepare the THP-MPTES SAM, 0.238 g (1.0mmol) MPTES, 0.126 g (1.5mmol) 3, 4-Dihydro-2H-pyran, and 0.025 g (0.1 mmol) PPTS was dissolved in 7.0 mil CH₂Cl₂. The mixture was stirred at room temperature for 96 hours. Then a fresh cleaned silicon substrate was immersed into the solution, kept in the solution for another 3 days for deposit THP-MPTES SAMs. When it's done, the sample was washed with CH₂Cl₂ thoroughly. A MPTES SAM was also prepared to compare with the THP-MPTES SAMs.

7.3.1.5 MPTES SAM Preparation:

2.0% (V/V) MPTES was added to 95:5 ethanol-water to make a solution. Trace amount of acetic acid is added to hydrolyse the MPTES for 5 minutes. Then the fresh cleaned substrate was immersed into the solution for 30 minutes to deposit MPTES SAM on the surface. Then the sample was washed with ethanol, and dried with N₂ blowing.

7.3.2 Results and Discussion

The fresh prepared THP-MPTES SAMs has a water contact angle of about 61.5° (Figure 7-7). The fresh prepared sample was then baked at 280 °C in air for 10 minutes.

The water contact angle of the sample after baked was reduced to 33.6°. This is due to the de-protection of the THP groups, and some –SH were formed.

The THP protected thiol has been investigated to a much lower extent than THP protected alcohols. Since the same method and mechanism used for synthesis of THP-protected alcohol are used for synthesis of THP-protected thiol [4], we can expect that the deprotection mechanism of THP protected thiol should however be similar to that in THP protected alcohols. According to the literature [6,7,8] reported mechanism of the deprotection of THP protected alcohols, we propose the following mechanism for the deprotection THP protected thiol compound:

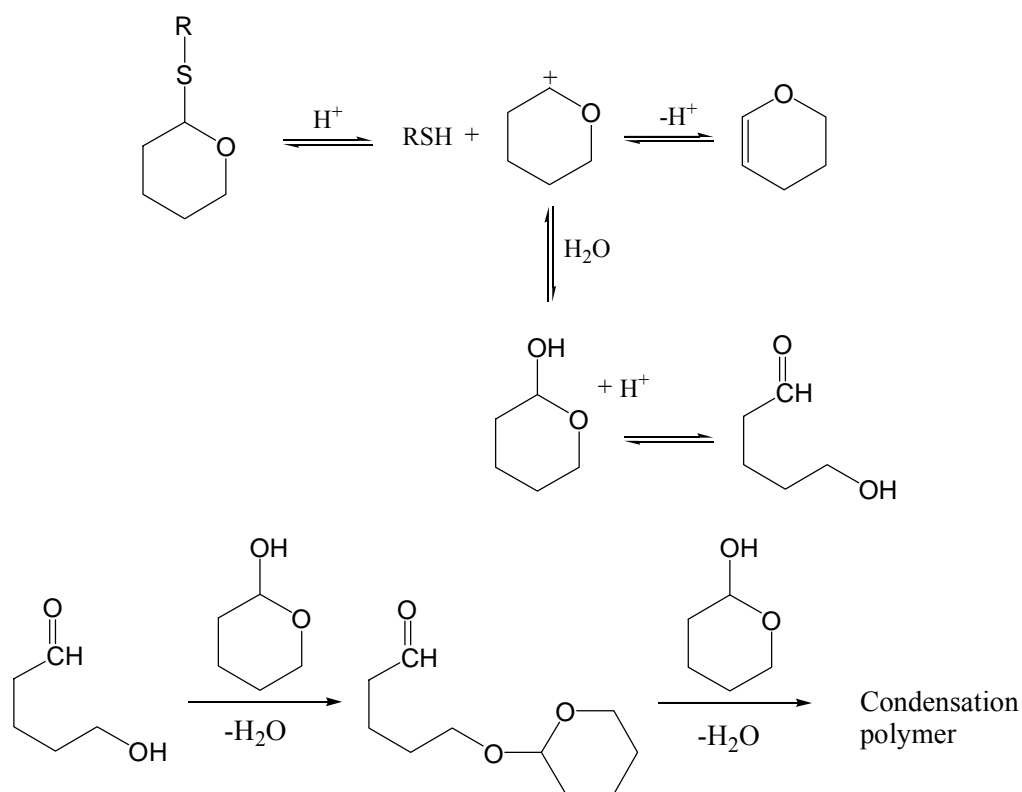


Figure 7-7. Deprotection of THP protected thiol compound

Upon deprotection, thiol groups are generated. The THP moiety from deprotection can form two different products. It can further lose a proton and form 3, 4-Dihydro-2H-pyran. Or if there is water in the environment, it can react with water and form an alcohol product. This product can further form condensation polymer products. Because the experiments were all conducted in a room air environment, and there is always approximately 40% relative humidity in the lab air, we expect that some of the deprotection product may form polymer residue on the sample surface.

But because the –SH groups are not stable in air, especially when it is heated [9], so it is very likely that after baking, some of the –SH groups are further converted to form S-S groups. Then the sample was further immersed into a DL-Dithiothreitol (DTT) water solution for 2 hours to reduce the S-S groups back to –SH groups [10].

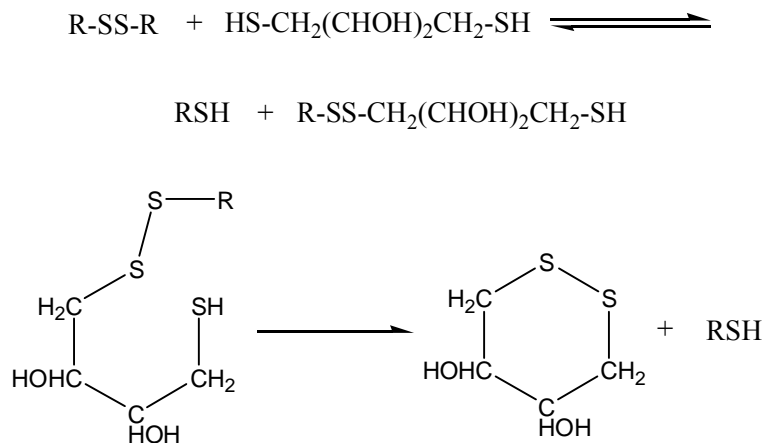


Figure 7-8. Reduction of disulfide compound by DTT

When it is done, the sample was washed with DI water thoroughly, and dried with N₂ blowing. The water contact angle of the sample after DTT treatment was further

reduced to 15.1°. This indicates that some of the S-S groups were reduced back to –SH group.

The water contact angle on the fresh prepared MP TES SAM was measured as 19.5°. The sample was then further baked at 110 °C for 15 minutes. The measured water contact angle of the same sample after baking was 33.0°. These two contact values are very close to the contact angle of the THP-MPTES before and after DTT treatment. This on the other side proved the formation of S-S groups during the de-protection of the THP group in THP-MPTES.

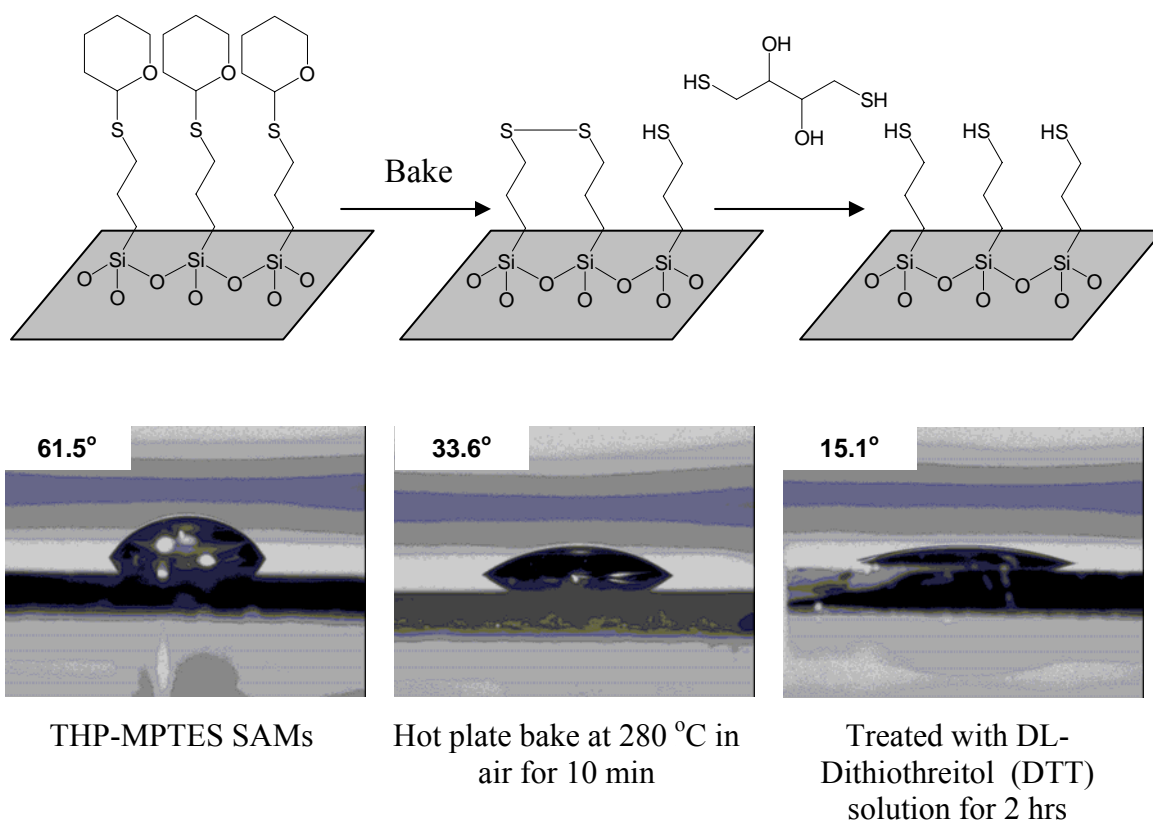


Figure 7-9. Contact angle measurements of THP-MPTES SAMs

XPS was also used to analyze the changes of THP-MPTES SAM after baking, and the results were compared with that of MPTES SAM. Figure 7-10 shows the XPS spectrums of THP-MPTES SAM before and after baking, and a XPS spectrum of MPTES SAM. The surface atomic concentrations of each element were list in Table 7-1.

XPS shows that there were 20.46% carbon atoms on a fresh prepared THP-MPTES SAM surface. After the sample was baked at 280 °C in air for 10 minutes, the carbon atomic concentration decreased to 10.79%. This value is close to the carbon concentration on a MPTES SAM surface, which is 8.67%. In each THP-MPTES molecule with all three ethoxyl groups reacted with surface –SiOH groups should have eight carbon atoms. If the THP protecting group is thermally deprotected, then only three of the eight carbon atoms stay on the surface. So theoretically, if all THP groups were cleaved after baking, the carbon concentration on the THP-MPTES should decreased to 7.7%, which is very close to the measured carbon concentration on the MPTES SAM surface. The a little bit high carbon concentration on the THP-MPTES SAM surface after baking is probably due to the factor that the THP deprotecting is not complete. There are about 24% of the THP was not deprotected. This is a very reasonable result.

All three samples have about the same Si concentration on their surface. This is because the XPS measure about 10 nm depth of the surface, and the SAMs are only one molecular layer. All the SAMs were prepared on a SiO₂ surface. The same Si concentration is consistent with the factor that there was almost constant thicknesses of SiO₂ were measured by XPS.

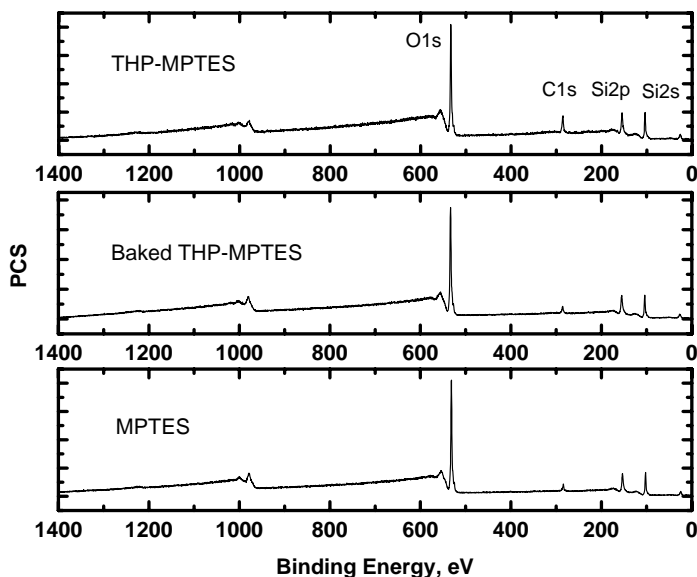


Figure 7-10. XPS analysis of MPTES SAMs

Table 7-1. Atomic concentration of different SAMs

SAMPLE	C1s	O1s	Si2p
THP-MPTES	20.46	51.92	27.62
Baked THP-MPTES	10.79	60.32	28.89
MPTES	8.67	62.49	28.84

AuNPs deposition was first done with three different bulk SAMs samples. One is fresh prepared THP-MPTES SAMs, one is the THP-MPTES SAMs after baking at 280 °C for 10 minutes, and the other one is baked THP-MPTES SAMs with treatment with DTT solution. These three samples were immersed in an AuNPs water solution (obtained from Prof. Mostafa A. El-Sayed's group in Chemistry School at Georgia Institute of Technology) for 8 hours. Then the samples were thoroughly washed with DI water, and N₂ gun blowing dried.

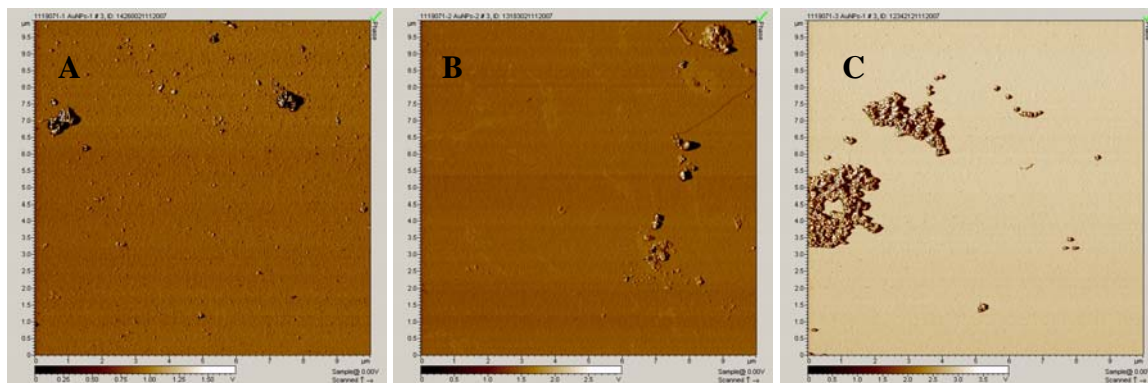


Figure 7-11. AFM phase images of THP-MPTES SAMs after deposition of AuNPs: (A) a fresh THP-MPTES SAM; (B) a THP-MPTES SAM baked at 280 °C for 10 minutes; (C) a baked THP-MPTES SAM treated with DTT/H₂O solution for 2 hours

Figure 7-11 shows three different THP-MPTES SAMs samples after deposition of AuNPs. We can see that, almost no AuNPs can be deposited on a fresh prepared THP-MPTES. Because thiol is not stable in air, especially when it is heated. During baking, the deprotected thiol groups tend to form disulfate compound, which has less bonding strength than thiol does. So there were still no many AuNPs deposited on the baked THP-MPTES. As mentioned before, the disulfate compound can be reduced to thiol compound. And we can see, compared with the first two samples, there were much more AuNPs deposited on the baked and DTT treated MPTES SAM.

All the results above show that, the proposed chemistry should work for this technology. Then the next step is to thermally write on a SAM, and selectively deposit AuNPs on thermally written areas.

Thermal writing was done by using the same equipment as in previous chapters. A 3X3 square array was thermally patterned on the surface. Each square in the array is a 2 μm square with 128 pixel scan resolution; the speed is 1.5 lines/sec. Each square is

written with different temperature, from room temperature to 560 °C. After thermal writing, the sample was treated with DTT/water solution for 3 hours to reduce the disulfate compound back to thiol compound. After thoroughly washed with DI water, the sample was immersed in AuNPs solution for 3 hours to selectively deposit AuNPs in the area containing thiol groups.

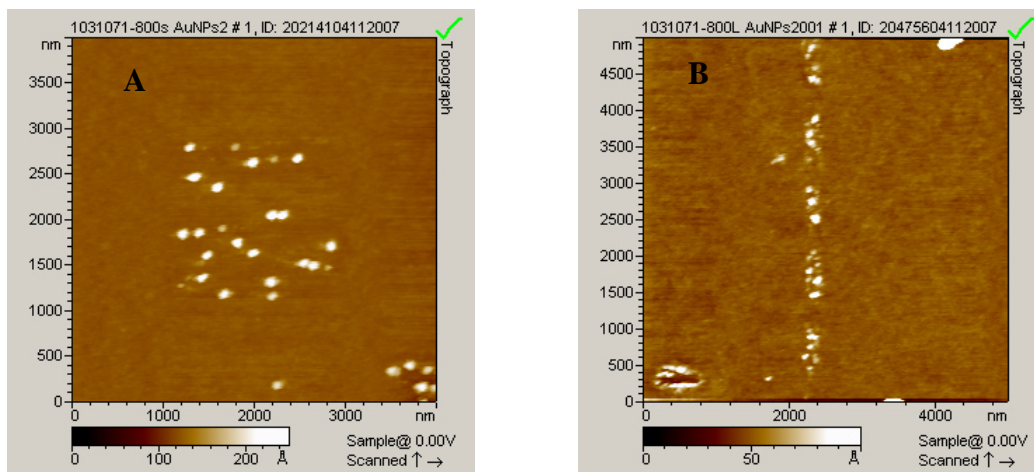


Figure 7-12. Deposited AuNPs on thermal written area of THP-MPTES SAMs

Figure 7-12 shows deposited AuNPs on two different thermal written patterns on THP-MPTES SAMs. Among those 9 squares, the square thermal written with a cantilever heating temperature of about 300 °C has the best AuNPs deposition (image A in Figure 7-12). The AuNPs were not densely packed in the thermal written area. This may be because at that thermal writing condition, only part of the THP group was deprotected. Image (B) in Figure 7-12 also shows deposited AuNPs lines on the thermally patterned THP-MPTES SAM.

The results show that, less or no AuNPs were deposited in the squares thermal written with a higher temperature. This may be because too high temperature can thermo-

mechanically abrade the SAMs. [11] So too high temperature is probably not good for our purpose. But if the temperature is too low, no THP can be deprotected. And the result indicates that temperature around 300 °C is probably the right temperature for thermally deprotecting the THP group without abrading the SAMs.

Among 9 different temperatures (the temperatures were divided almost evenly from room temperature to 560 °C), we observed that at about a 300 °C cantilever heating temperature, we obtained the best AuNPs deposition in the thermal written area after the subsequent AuNP deposition process. Either higher temperature or lower temperature did not give better results. But even for our best result, the AuNPs are not densely packed in the thermal written area. For low coverage, there are two possible reasons cause this. One is at this writing temperature; the THP was not completely deprotected. Another reason is at this temperature, some of the SAMs may also be thermally decomposed due to C-C chain cleavage. For the first reason, we used cantilever heater temperature of 300 °C. But the tip temperature will be about a couple of tens degrees below this temperature. According to XPS analysis, about 75% of the SAMs were deprotected at 280 °C for 10 minutes. So during the thermal writing experiments reported here, the temperature and time is likely to be insufficient to completely deprotect the THP protected SAM and generate the desired –SH groups. And on the other side, at this writing temperature, the SAMs start to be thermally decomposed due to the C-C bond cleavage. Kim [12] investigated the thermal stability of the OTS based SAMs in air. Their experimental results show that, above 220 °C the monolayers primarily decompose through C-C bond cleavage, with a gradual reduction in chain length. For our SAM, any C-C bond cleavage in a propyl chain will eliminate a –SH group from the surface. Our writing temperature

was close to or already above the 220 °C, so we can expect that certain amount of sulfur containing groups were eliminated from the surface due to the C-C bond cleavage in the propyl chain. This makes the –SH group density even low after thermal writing. We believe the combination of these two reasons explains why the AuNPs coverage was so low in the thermal written area.

The above experiment shows that, due to those two opposite effects of writing temperature on the generated –SH group density on the surface, the temperature operation window for this type of SAMs may not be very wide. In the above experiment, we just used a coarse temperature grid to investigate the temperature effect. The best temperature we found in that experiment probably is not the optimal writing temperature for this SAM. In order to find the optimal writing temperature, we suggest the best way is to perform thermal writing on the SAM with a finer temperature grid. Also experiments on blank samples can also be used to help to find out what is the best recipe for thermal writing and AuNPs deposition on this SAMs.

7.4 Conclusions

In this Chapter we reported that self assembly monolayers (SAMs) can be successfully patterned with thermal probe lithography. Two different SAMs (APTES and THP-MPTES) were investigated. We found too high temperature may abrading the SAMs. This issue narrows the temperature operation window for this process.

7.5 References

- [1] Simon A; Cohen-Bouhacina T; Porte M C; Aime J P; Baquey C Study of two grafting methods for obtaining a 3 - aminopropyltriethoxysilane monolayer on silica surface. *Journal of colloid and interface science* (2002), 251(2), 278-83
- [2] Shi, Bing; Lu, Xinchun; Luo, Jianbin; Chen, Darong; Liang, Hong. Frictional properties of molecular thin films. *Surface and Interface Analysis* (2001), 32(1), 283-285
- [3] Fresco, Zachary M.; Frechet, Jean M. J. Selective Surface Activation of a Functional Monolayer for the Fabrication of Nanometer Scale Thiol Patterns and Directed Self-Assembly of Gold Nanoparticles. *Journal of the American Chemical Society* (2005), 127(23), 8302-8303
- [4] Kipnis, Frank; Ornfelt, John. 2 - Substituted tetrahydropyranyl sulfides. *Journal of the American Chemical Society* (1951), 73 822
- [5] Masaaki Miyashita, Akira Yoshikoshi, and Paul A. Grieco, "Pyridinium p-Toluenesulfonate A Mild and Efficient Catalyst for the Tetrahydropyranylation of Alcohols", *J. Org. Chem.*, 1977, 42(23):3772-3774
- [6] Reinhold Schwalm, Horst Binder, Dirk funhoff, A new environmentally Stable Protective Group for Deep UV Resists: Methoxy(tetrahydropyranyl) Ether, *Journal of Applied Polymer Science*, (2000) 78: 208-216
- [7] Toshio Sakamizu, Hiroshi Shiraishi, Hidenori Yamaguchi, Acid-Catalyzed Reactions of Tetrahydropyranyl-Protected Polyvinylphenol in a Novolak-Resin-Based Positive Resist, *Japanese Journal of Applied Physics*, (1992) 31:4288-4293
- [8] Peter G. M. Wuts, Theodora W. Greene, *Greene's Protective Groups in Organic Synthesis* (4th edition) Wiley-Interscience (2007), p59
- [9] Manisha Sathe, Ramarao Ghorpade, and Mahabir Parshad Kaushik, "Oxidation of Thiols to Disulfides Using Silica Chloride as a Heterogeneous Catalyst", *Chemistry Letter*, 2006, 35(9): 1048-1049
- [10] W.W.Cleland, "Dithiothreitol, an New Protective Reagent for SH groups" *Biochemistry*, 1964, 3(4):480-482
- [11] Kim, Hee K.; Lee, Jae P.; Park, Chan R.; Kwak, Hyon T.; Sung, M. M. Thermal Decomposition of Alkylsiloxane Self-Assembled Monolayers in Air. *Journal of Physical Chemistry B* (2003), 107(18), 4348-4351

- [12] Kim, Hee K.; Lee, Jae P.; Park, Chan R.; Kwak, Hyon T.; Sung, M. M. Thermal Decomposition of Alkylsiloxane Self-Assembled Monolayers in Air. *Journal of Physical Chemistry B* (2003), 107(18), 4348-4351

CHAPTER 8

SIMULATION AND MODELING

8.1 Introduction

In thermal writing experiments, there are two major processes are going on; one is heat transport, and the other one is chemical reaction. For the heat transport part, because the dimension of the thermal cantilever tip is so small (less than 100 nm), there is no easy way to direct measure the heat transportation from this kind of heat source. The time scale of heat transportation in the thermal writing is from microsecond to millisecond. This makes the direct measurement of the heat transportation even harder. So the better way to understand the stories behind the experiment results will be simulation and modeling. For the chemical reaction part, most of the chemical reactions involved in the thermal writing experiments are thermal decomposition. TGA is one of the best choices for thermal analysis, so it is frequently used in analysis the kinetics of the thermal decomposition reactions involved in the thermal writing experiments. The thermal decomposition in the thermal writing experiments usually complete within microsecond or millisecond, which is a couple of order of magnitude fast than that in normal TGA analysis. So the simulation and modeling tool is still used for the chemical reaction part of the thermal writing experiments.

This chapter is mainly focused on the simulation and modeling work of heat transport and chemical reaction involved in the thermal writing experiments. FemLab and Matlab are used to accomplish these works. Simulation and modeling results are compared with experimental results where they are available.

8.2 Simulation of Cantilever Heating

A model thermal cantilever is built in FemLab (see Figure 8-1). This model thermal cantilever has the same dimension as a thermal cantilever used in thermal writing experiments. The cantilever heater dimension is 8x16 μm , and the cantilever leg dimension is 10x100 μm . The thickness of cantilever is 1 μm . In the model, the cantilever is tilted by an angle of 10 degree, and the center of the heater is 1 μm above the substrate, which is silicon. The cantilever is surrounded by air. The dimension of the air domain is 200 μm wide, 300 μm long and 50 μm tall. The substrate has the same lateral dimension as the air domain, but the thickness is 5 μm . The air domain and the silicon substrate are continuously connected with each other.

Because the radiation and convection heat transfer are much smaller than thermal conduction, [1] so only thermal conduction is considered in simulation.

The control equation used for the heat transport calculation is:

$$-\nabla \cdot (k\nabla T) = Q \quad (8-1)$$

Where k ($\text{W}/\text{m}^*\text{K}$) is the thermal conductivity of materials in the model, T (K) is temperature, and Q is heat change in the system.

For the material properties part, the silicon substrate has a constant thermal conductivity of 163 $\text{W}/\text{m}^*\text{K}$. The surrounding air has a temperature dependent thermal conductivity of $6e-5*T+0.0088$, where T is temperature with unit of K . The cantilever heater and leg are made of doped silicon. The thermal conductivity used for the cantilever is $136.53-0.1114*T$. The cantilever heater temperature is set at a constant value for one simulation. The total cantilever heating power needed to keep this temperature is calculated by adding all the heat flux at all six faces of the cantilever heater. The initial

temperature of the system is 300K. Boundary condition of the system is that the system has a constant temperature of 300K at all edges of the system, and heat transport is continuous at all interfaces.

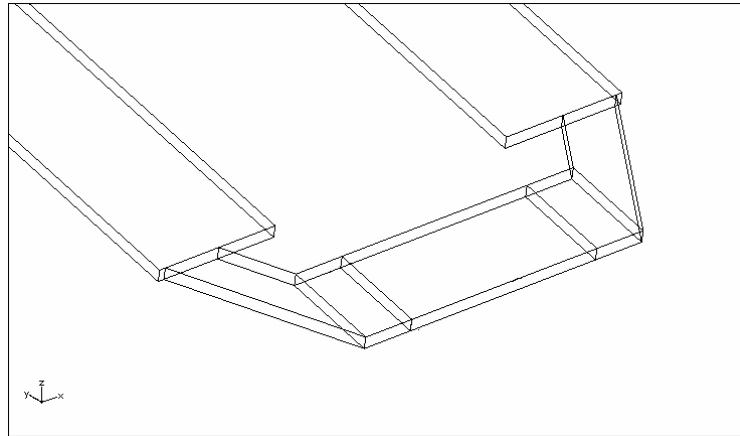


Figure 8-1. FemLab model for a thermal cantilever

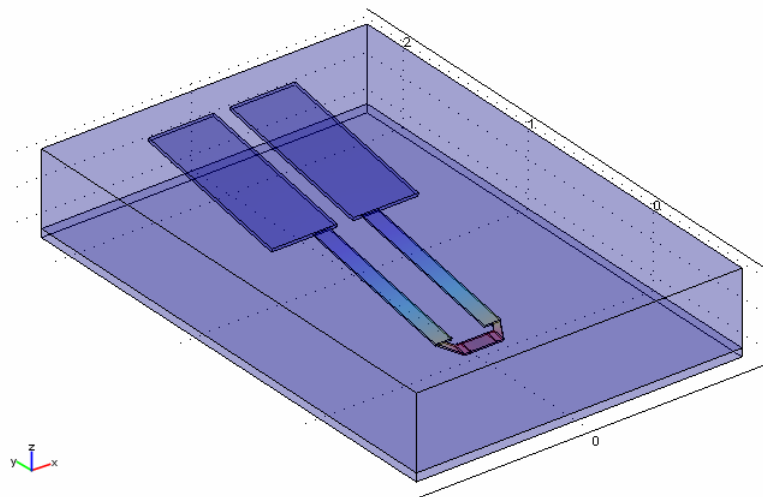


Figure 8-2. FemLab model for a thermal cantilever in a room environment

Figure 8-3 shows the heat dissipation through cantilever legs, through air gap between heater and substrate, and through surrounding air at different temperature. We can see most of the heated generated in the cantilever heater is dissipated through the

cantilever legs. This is expected, because compare to air, cantilever leg, which is made of silicon, has much higher thermal conductivity. The thermal resistance in cantilever legs is much smaller.

One thing need to point out here is that there are more heat dissipated through the air gap between the cantilever heater and the substrate than that through the surrounding air. And obviously, the thermal resistance of the air gap is directly related to the thickness of the gap. This tells us that the heat dissipation will be affected by the distance of the cantilever heater from the substrate. The heat dissipation through legs and other surrounding air should be less affected by the thickness of the gap. And the heat dissipation directly determines the how high temperature can the cantilever be heated with certain heating power, so heater temperature is affected by the thickness of the air gap at constant heating power. The same principle has been used in IBM's millipede project to detect the data bit with the same thermal cantilever [2]. And King [3] gave a very comprehensive analysis of this technology.

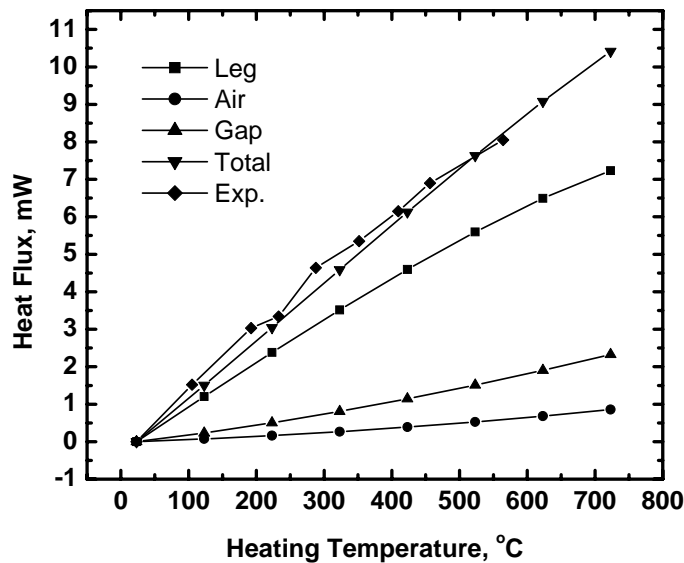


Figure 8-3. Cantilever heat dissipation at different heater temperatures

Some experimental temperature calibration data of a really thermal cantilever with the same dimensions as the one in the simulation model are also included in Figure 8-3. We can see that the experimental data have excellent agreement with the simulation, this prove the validation of the assumptions made in the model, and prove that the conclusions extracted from the simulation results are trustable.

8.3 Heat Transport and Reaction Kinetics in Thermal Decomposition

According to standard TGA data (Figure 3-4), the PC-4 polymer used for thermal writing experiments in Chapter 3 decomposes at about 250 °C. But the line depths vs. heating time data (Figure 4-3) show that PC-4 polymer start to decompose when the cantilever heater temperature is close to 500 °C. This section will try to use heat transport and reaction kinetics during the thermal writing experiment to explain why there is such big temperature difference between the standard TGA results and thermal writing results. Figure 8-4 shows the temperature distribution in a heated cantilever tip which is in contact with a polymer thin film. In this system, the heat is generated in the cantilever heater region, and flows along the cantilever tip down to the substrate, and then dissipates into environment. In this heat transport path, there are three thermal resistances: one is the thermal resistance of the cantilever tip, one is the contact resistance between the tip and the polymer, and the other one is dispersion thermal resistance of the substrate. There are a couple of very good literatures about the analysis of heat transport in the heated cantilever tip. When the dimension decreases below the mean free path of the thermal carrier, which is the phonon in silicon, the thermal conductivity of the material decrease. So the thermal conductivity of the cantilever tip is not just temperature dependent, but also dimension dependent. But even consider the dimension effect, the thermal

conductivity of the cantilever tip still much large compare to the polymer. So small decrease of the thermal conductivity of the cantilever tip will not have significant effect on heat transfer of the entire system [4]. And the dimension effect on the thermal conductivity is really complicated, and there is no easy solution of this issue. To simplify the problem, only the temperature dependence of the conductivity of the tip is considered in this analysis. The dispersion thermal resistance of the substrate is well known. The only left problem is the contact resistance between the tip and the polymer. There is a lot of discussion of the thermal contact resistance in nanoscale [5,6], but it is still a under understood problem. But the thermal contact resistance is a very important issue for this thermal transport problem. So according to literature report [7], the author very roughly estimated that the thermal contact resistance between the silicon tip and the polymer material is about 4 nm of the thermal oxide, which has a thermal conductivity of about 1 W/m.K. To simplify the parameter boundary condition settings in FemLab model, a 4 nm oxide layer with thermal conductivity of 1 W/m.K is put between the cantilever tip and the polymer layer to simulate the thermal contact resistance.

Figure 8-5 shows the temperature profile along the cantilever Z axle. From the temperature profile we can see that there is about 60 degree temperature drop during the first 4 nm distance after the tip. In the FemLab model, this 4 nm distance belongs to the interface between the tip and the polymer, so this 60 degree temperature drop is only due to the thermal contact resistance. Since we didn't consider the dimension dependence of the thermal conductivity of the cantilever, in the simulation results, there is no big temperature along the tip region. According to their experimental results in thermal nano

indentation, researchers in IBM also estimated that temperature in the contact area is about 100 degree below the cantilever heater temperature [8,9].

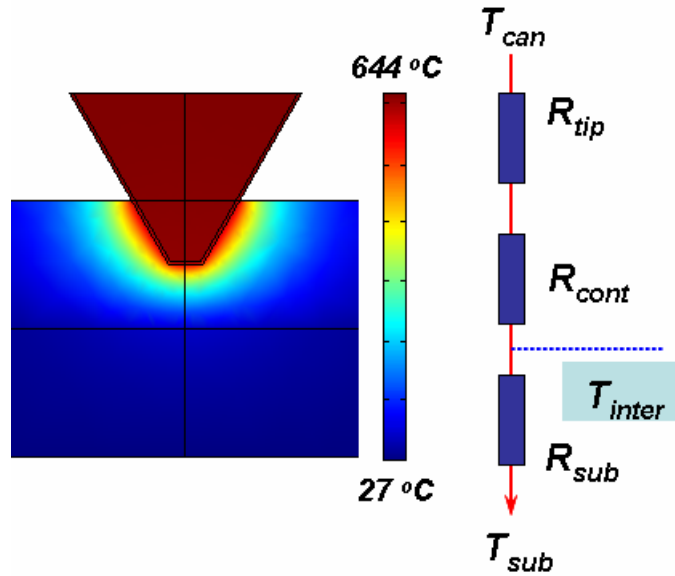


Figure 8-4. Heat transport in AFM thermal writing

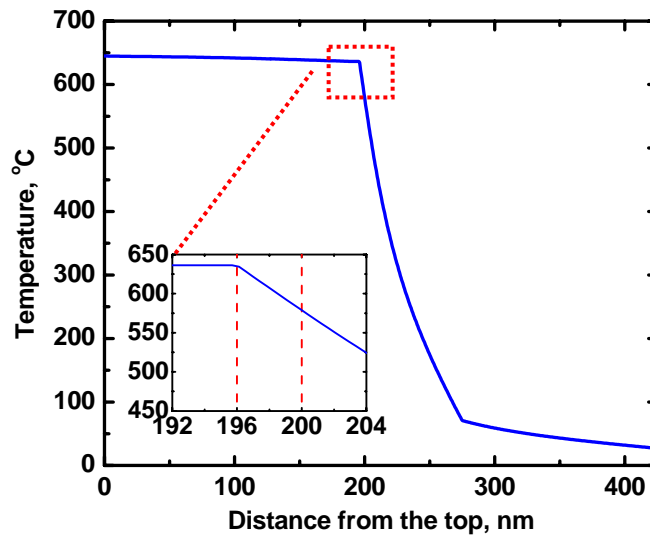


Figure 8-5. Temperature profile along the cantilever central axis.

This simulation results explains why the thermal writing experiment need much higher temperature than the thermal decomposition temperature of the material observed in the standard temperature. But as mentioned before, the temperature difference is about 200 degree. Something else should make some contribution to this too. So next step is to look at the reaction kinetics of thermal decomposition of the PC-4 polymer.

Assume the thermal decomposition of PC-4 polymer follows a first order decomposition kinetics. The rate constant is temperature dependent, and follows Arrhenius equation. By rearranging the kinetics equation, we can obtain a linear relation (see Equation 8-2) between the remaining weight and the temperature for a standard TGA with constant temperature ramping rate.

$$\begin{aligned}
 -\frac{dw}{dt} &= Kw, K = A \exp\left(\frac{-Ea/R}{T}\right) \\
 \Rightarrow -\frac{d \ln w}{dt} &= A \exp\left(\frac{-Ea/R}{T}\right), t = \frac{T - T_o}{C} \\
 \Rightarrow -\frac{d \ln w}{dT} &= \frac{A}{C} \exp\left(\frac{-Ea/R}{T}\right) \quad (8-2) \\
 \Rightarrow -\frac{d \ln w}{dT} &= \exp\left(b - \frac{a}{T}\right), a = -Ea/R, b = \ln\left(\frac{A}{C}\right) \\
 \Rightarrow \ln\left(-\frac{d \ln w}{dT}\right) &= b - \frac{a}{T}
 \end{aligned}$$

Where,

A is the pre-exponential factor, sec-1;

C is heating rate, K · sec-1;

Ea is activation energy, J · mol-1;

R is gas constant, 8.314 J · K-1 · mol-1

Then by fitting a single TGA trace, we can get both the activation energy of the thermal decomposition and the pre-factor for Arrhenius equation.

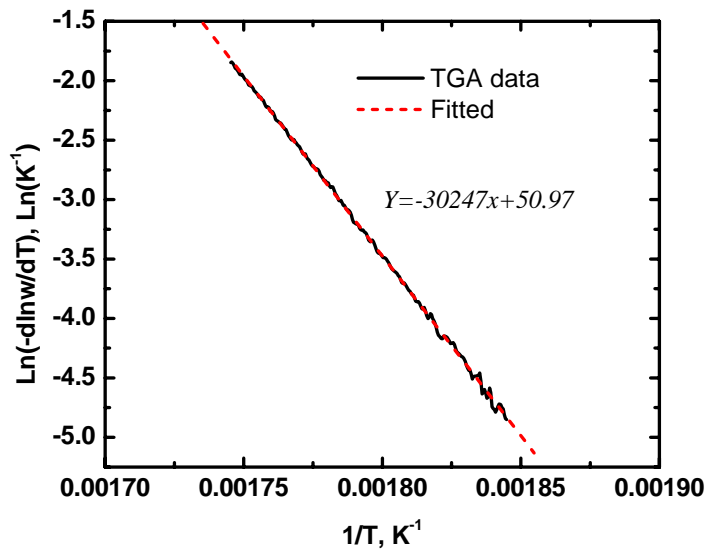


Figure 8-6. Experimental TGA data fitting to extract the kinetics parameters of thermal decomposition of PC-4 polymer

Figure 8-6 shows a plot of $\ln\left(-\frac{d \ln w}{dT}\right)$ vs. $1/T$ of the TGA data in Figure 3-4.

The TGA data in the temperature range from 268 °C to 298 °C are chosen, because most of the weight lost is happened in this temperature range. From the Figure 8-6 we can see the TGA data very well fitted by a linear equation. Then we can very accurately obtain the constant a (the slope) and b (the intersection) in Equation 8-2. Then we can get $Ea = 251 \text{ KJ/mol}$, $\ln(A) = 49.2$

If there are two or more decomposition steps in one TGA trace, as long as the different steps are clearly separated in different temperature ranges, we can use the similar method to extract the activation energy and pre-factor for each decomposition step by fitting the TGA data in different temperature range.

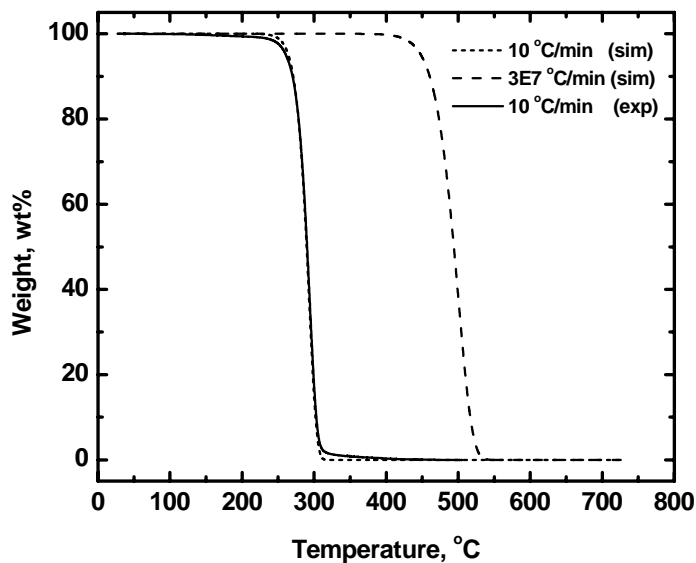


Figure 8-7. Experimental and simulated TGA curves for PC-4 polymer

After we know the activation energy and pre-factor for the decomposition, we can calculate the TGA curves by following Equation 8-2, but in a reverse sequence. Matlab is used in this work to calculate the TGA curves from activation energy and pre-factor (see Appendix C and D). Figure 8-7 shows an experimental TGA curve and a simulated TGA curve with same heating rate (10 °C/min). The simulated TGA curve almost perfectly matches the experimental curve. Only at the beginning and the end of the weight loss, there are slightly deviation between the simulation results and the experiment results. For the deviation at the beginning, it is mainly due to desorption of some volatile compound (solvent or moisture) in the polymer. The deviation at the end of weight loss is mainly due to the decomposition residue.

One big difference between the standard TGA experiment and thermal writing experiment is the heating rate. The heating rate used in experimental TGA in this work is

10 °C/min. But during thermal writing, polymer is heated up to 500 -700 °C in millisecond time scale. A heating rate of 500 °C/ms equals to 3×10^7 °C/min, which is six orders of magnitude faster than standard TGA heating rate. This heating rate is impossible to be achieved in normal TGA. So it is impossible to direct compare the experimental TGA and thermal writing experiment at the same heating rate. But we can obtain the activation energy and pre-factor from standard TGA data, and use these data to calculate the simulated TGA data with the same heating rate as that used in the thermal writing experiments. Figure 8-7 also shows a simulated TGA curve of PC-4 at a heating rate of 3×10^7 °C/min, which is same as the heating rate for thermal writing. The simulated TGA data shows that with a heating rate of 3×10^7 °C/min, we can start to observe the weight loss at about 450 °C, which is 200 °C above the decomposition temperature observed in standard TGA. Plus the about 60 °C temperature drop between the polymer in contact with the heated tip and the cantilever heater, the cantilever heater needs to be 260 °C higher than the decomposition in standard experimental TGA in order to decompose the polymer using heated tip. This simulation results are very close to the thermal writing results, which shows that in order to decompose the PC-4 polymer, the heater temperature needs to be close to or above 500 °C. But the decomposition temperature observed in standard experimental TGA is about 250 °C for this polymer.

Do we can conclude that the decomposition temperature difference between experimental TGA and thermal writing experiment is contributed by two factors: one the temperature drop at the contact area; and the other one is the heating rate difference.

8.4 Modeling of Thermal Writing Process and Experimental Data Fitting

In Chapter 4, the effects of scan speed, which is inverse proportional to decomposition time, and heating temperature on line scan depth are experimentally investigated. Those results are the base for the 3D thermal writing described in Chapter 4. Basically, nano thermal writing is a quasi steady state nano scale polymer thermal decomposition process under a heated cantilever tip. In this section, the author will try to understand this process from the reaction kinetics point of view, and build a process model for this process.

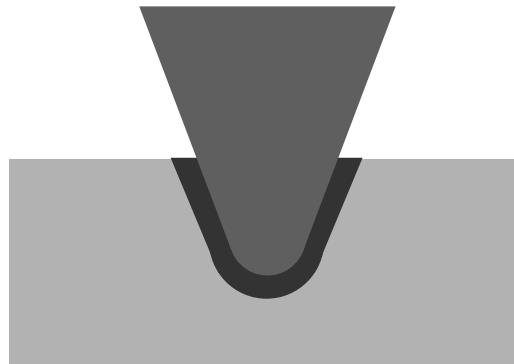


Figure 8-8. A heated cantilever tip in contact with polymer material

In previous section, it is already shown that the decomposition of PC-4 follows the first order reaction kinetics. Assume only the material in a very small region (with a thickness of δ) around the contact area is heated above the decomposition temperature. And the temperature in this region is T . Then according the reaction kinetics, we should have:

$$-\frac{dw}{d\tau} = Kw = K \cdot (S \cdot \delta \cdot \rho) \quad (8-3)$$

Where, S is the contact area

δ is the thickness of heated region

ρ is the density of the polymer

τ is time

Also, according to the mechanical point of view, materials are decomposed in the path of the tip, so we should have:

$$-\frac{dw}{d\tau} = S \cdot v \cdot \rho \quad (8-4)$$

Where, v is the scan speed.

Then we shall have:

$$\begin{aligned} v &= K \cdot \delta, K = A \cdot \exp\left(\frac{-Ea/R}{T}\right) \\ \Rightarrow t &= \frac{1}{v} = \frac{1}{K \cdot \delta} = \exp\left(\frac{a}{T} - b\right) \quad (8-5) \\ a &= Ea/R, b = \ln(A \cdot \delta) \\ \Rightarrow T &= \frac{a}{\ln t + b} \end{aligned}$$

Where t is the decomposition time, which is inverse of scan speed [sec/um].

Ea is activation energy

A is prefactor in Arrhenius equation

R is gas constant

The temperature in the contact region T is different from the heating temperature, and it also depends on the line depth.

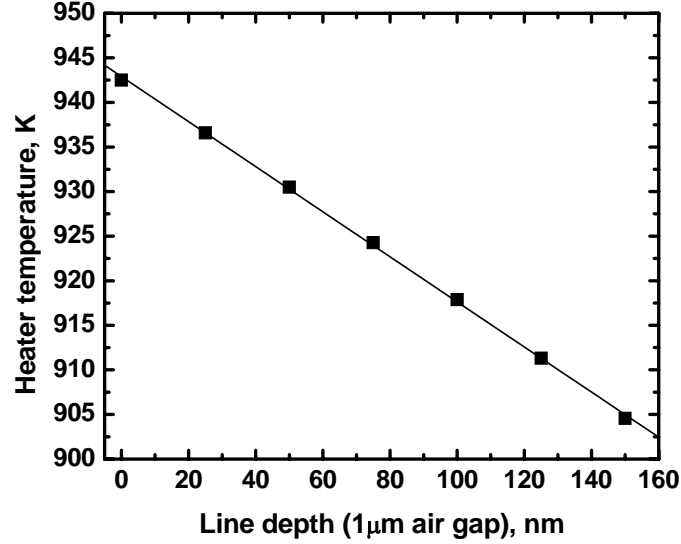


Figure 8-9. Heater temperature vs. line depth for constant heating power

As mentioned in previous discussion, the heat dissipation through the gap between the cantilever heater and the substrate is considerable. The thermal resistance of this gap is linear proportional to the thickness of the gap. Then it is easy to understand that the heater temperature drops linearly as the thickness of the air gap decrease or the line depth increase (see Figure 8-9).

We also know the disperse thermal resistance of the polymer layer is $L/(K*A)$, where L the average length of the polymer between the tip and the substrate, A is the contact area, and K is thermal conductivity of polymer, which is constant in this analysis. As the line goes deeper, L decrease linear and A increase squarely with respect to line depth. So the disperse thermal resistance of the polymer layer decrease cubically with respect to the line depth. The temperature drop in the polymer layer decrease cubically with respect to the line depth.

According to the above discussion, the heat flux in unit contact area should increase linearly with respect to line depth. Because the temperature drop on the interface is linear proportional to the heat flux. This means the temperature drop on the interface increase, and the temperature on the polymer side decrease linearly with respect to line depth.

Because the above three effects of line depth on the temperature is super imposed to each other. Then we can conclude that the temperature of the polymer in the contact region decrease 5th order with respect to the line depth. Because of complexity of the system (tip shape, two different materials, etc.), it is impossible to obtain the analytical solution for the tip temperature. But according to the above qualitative arguments, it is reasonable to have the following relation between the tip temperature and the line depth.

$$T = T_o - (P_1 \cdot x)^{P_2} \quad (8-6)$$

Where x is the line depth, T_o is contact area temperature when line depth is zero, P_1 and P_2 are constants. And we already know $P_2=5$.

Then plug the relation in Equation 8-6 into Equation 8-5. After rearranging the equation, we can obtain the line depth as a function of heating temperature and decomposition time (see Equation 8-7).

$$x = \frac{1}{P_1} \left(T_o - \frac{a}{\ln t + b} \right)^{1/P_2} \quad (8-7)$$

Figure 8-10 shows FemLab simulated the tip temperature versus the line depth for different heating temperature or polymer thermal conductivity. These data points are fitted using Equation 8-6. From the Figure we can see that, the heating temperature and the polymer thermal conductivity affects the T_o parameter in Equation 8-6 significantly.

It is easy to understand that when the heating temperature decreases, the initial tip contact temperature T_0 drop too. And T_0 drops almost same amount as the heating temperature. Also, as the polymer thermal conductivity increase, the polymer temperature in contact with the tip should decrease, because heat can be easily dissipated. Figure 8-10 also indicates that the parameter P1 is independent to the heating temperature or polymer thermal conductivity. For all three data plots, the fitted P1 parameter has almost the same value.

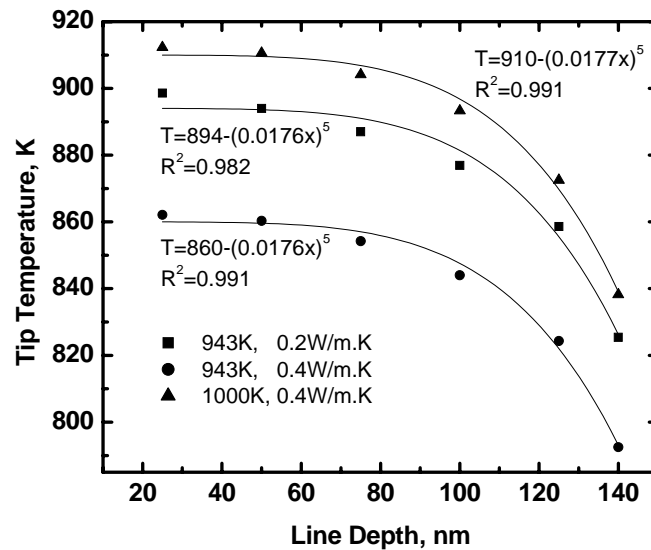


Figure 8-10. Sensitivity analysis of heating temperature and thermal conductivity of polymer

Figure 8-11 shows FemLab simulated the tip temperature versus the line depth for different polymer film thickness. T_0 and P1 parameter were obtained by fitted those data points with Equation 8-6. We can see, film thickness has very little effect on T_0 , but it affects P1 significantly.

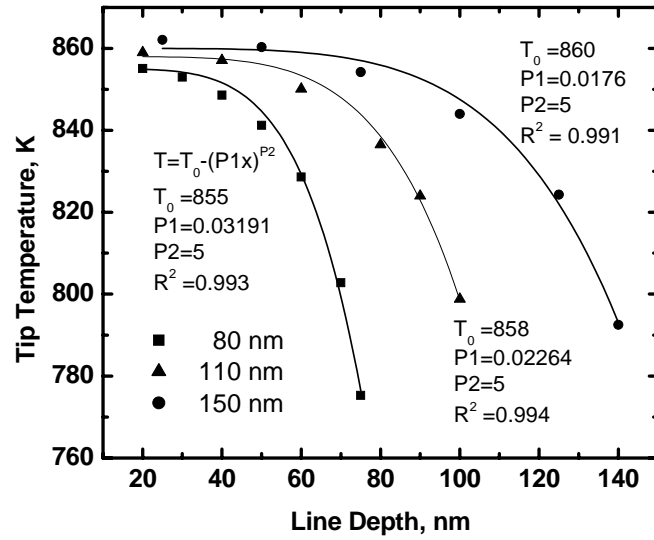


Figure 8-11. Tip temperature vs. line depth for different sample film thicknesses

In Equation 8-7, $b = \ln(A \cdot \delta) = \ln(A) + \ln(\delta)$, where A is the pre-exponential factor, which is a constant for a certain polymer, and δ is the thickness of the heated region. Because we use assume the heated region has same temperature, so δ is a nominal thickness. We assume all the decomposition occurs in this heated region with same decomposition rate. And the total decomposition rate equals to the total decomposition rate in entitle heated polymer film with a position dependent decomposition rate. Equation 8-8 can be used to calculate δ :

$$\delta = \frac{\sum K_T \pi (r_0 - z)^2 dL}{K_{Tip} \pi \times r_0^2} \quad (8-8)$$

Where r_0 is the radius of curvature of cantilever tip; z is the distance of certain position in the polymer film to the tip surface; dL is the thickness of each element in numerical integration; K_{Tip} and K_T are decomposition rate constants at tip surface and in the film, respectively; and can be calculated using Equation 8-9.

$$K_T = A \exp\left(\frac{-E_a}{R \times T}\right) \quad (8-9)$$

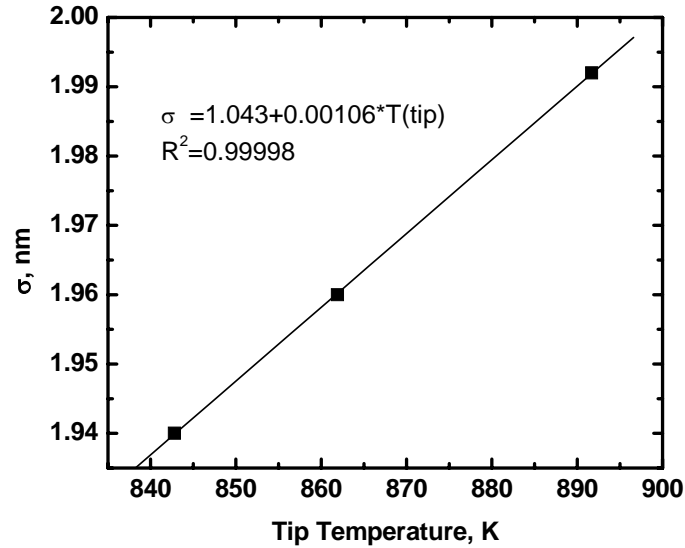


Figure 8-12. Thickness of heated region versus tip temperature

The plot in Figure 8-12 shows the nominal heated region thickness δ for different tip temperature for a film thickness of 150 nm. We can see δ has a weak linear relation with tip temperature. For a 900 K initial tip temperature, the tip temperature decreases by 100 K when it penetrates into the polymer film. δ only changes about 0.1 nm, which is only about 5% of the total thickness of the nominal thickness. According to this, it is a reasonable to assume that if the tip temperature doesn't change significantly, the nominal heated region thickness δ is a constant.

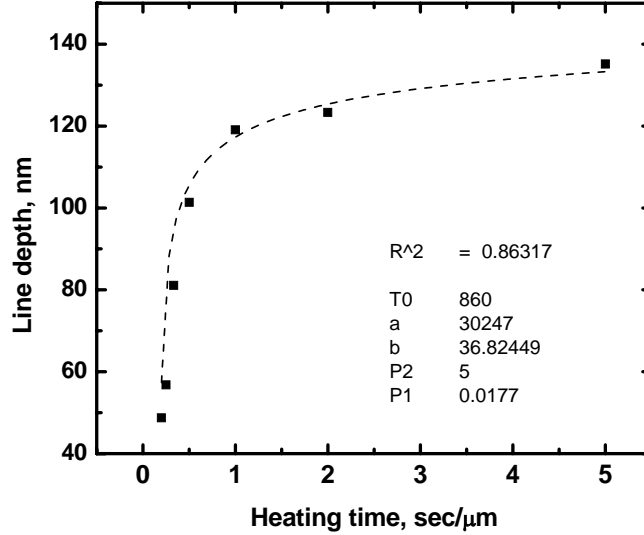


Figure 8-13. Experimental results and modeling results for thermal writing line at 663 °C

All the parameters, except for constant b , in Equation 8-7 are from experiments or simulation results. Then keep all other parameters constant, except for constant b , Equation 8-7 is used to fit the experimental thermal writing data for writing temperature of 663 °C. The results are plotted in Figure 8-13. We can see, the experimental results can be very well fitted by the simple model described in Equation 8-7. But the obtained parameter is a little bit smaller than expected value. This could be due to the obtained pre-exponential factor from TGA data fitting is not very accurate, or the tip temperature is lower than expected because some of the heat is used to vaporize the decomposition products, or due to the cantilever heating temperature calibration is not very accurate, especially when the cantilever resistance is above the peak resistance.

For thermal writing at lower temperatures, the model can not fit the experimental data very well. This is mainly because the decomposition rate is lower, and thermal

mechanical pressing may contribute to some of the line depth. So when writing temperature is lower, it is not just a simple thermal decomposition process; it is actually a combination of thermal decomposition and thermal mechanical pressing. But the model only considers thermal decomposition. At high thermal writing temperature, most of the line depth is contributed by thermal decomposition. So the model fits the data very well.

8.5 Conclusions

In this Chapter, finite element analysis tool (FemLab) was used to analyze thermal cantilever heating and the heat transfer during thermal writing. The simulated results have very good agreement with experimental data. The thermal decomposition process using a heated cantilever tip was detailed analyzed from both heat transfer and reaction kinetics. A basic model was built for this process. And the experimental data can be very well fitted using this model.

8.6 References

- [1] Tanya L. Wright, PhD thesis, "Fabrication and Testing of Heated Atomic Force Microscope Cantilevers", Georgia Institute of Technology, 2005
- [2] Vettiger, P.; Despont, M.; Drechsler, U.; Durig, U.; Haberle, W.; Lutwyche, M. I.; Rothuizen, H. E.; Stutz, R.; Widmer, R.; Binnig, G. K. The " Millipede "-more than one thousand tips for future AFM data storage. IBM Journal of Research and Development (2000), 44(3), 323-340.
- [3] King, William P. Design analysis of heated atomic force microscope cantilevers for nanotopography measurements. Journal of Micromechanics and Microengineering (2005), 15(12), 2441-2448
- [4] Brent A. Nelson, PhD thesis, "Nanoscale Thermal Processing Using A Heated Atomic Force Microscope Tip" Georgia Institute of Technology, 2007

- [5] E. T. Swartz, R. O. Pohl, Thermal Boundary Resistance, *Review of Modern Physics*, 1989, 61(3):605-668
- [6] Prasher, Ravi S.; Phelan, Patrick E.. Microscopic and macroscopic thermal contact resistances of pressed mechanical contacts. *Journal of Applied Physics* (2006), 100(6), 063538/1-063538/8
- [7] Cahill, David G.; Ford, Wayne K.; Goodson, Kenneth E.; Mahan, Gerald D.; Majumdar, Arun; Maris, Humphrey J.; Merlin, Roberto; Phillpot, Simon R. Nanoscale thermal transport. *Journal of Applied Physics* (2003), 93(2), 793-818
- [8] W. P. King, T. W. Kenny, K. E. Goodson, G. L. W. Cross, M. Despont, U. Durig, H. Rothuizen, G. Binnig, and P. Vettiger, "Design of atomic force microscope cantilevers for combined thermomechanical writing and thermal reading in array operation," *J. Microelectromech. Syst.* 11, 765–774 (2002).
- [9] W. P. King and K. E. Goodson, "Thermomechanical formation and thermal detection of polymer nanostructures," in *Heat Transfer and Fluid Flow in Microscale and Nanoscale Structures*, M. Faghri and B. Sunden, Eds., pp. 131–171, WIT Press, Southampton (2002).

CHAPTER 9

SUMMARY AND RECOMMENDATIONS FOR SUTURE WORKS

9.1 Summary

This work presents the novel applications of heated AFM tip in nanolithography. Different strategies were investigated for patterning materials using heated AFM tip. New materials were developed specifically for these new nanolithography methods. Some simulation and modeling work was done to further understand the heat transfer and chemical reactions involved in the thermal writing process.

The selective thermal decomposition of polymer was the first thermal patterning method using heated AFM tip we've investigated. A couple of different sacrificial polymers were used as the writing materials. Among these materials, the cross-linked amorphous polycarbonate (CPC-IV) was the best material for this application. Cross-linking can improve the resistance to thermal flow during thermal writing, which is the most critical issue for this application. Also amorphous is very important for obtaining a uniform polymer thin film with smooth surface. The effect of cross-linking density on the performance of the material was investigated. High cross-linking density is good for getting high resolution. But the material with high cross-linking density needs more energy to be decomposed, and this can slow down the writing speed. Another important advantage of cross-linked polymer versus linear polymer is that the decomposition depth of cross-linked polymer is much easy to be controlled. Base on this property, we've developed a novel 3D thermal writing technology using cross-linked polymer as the writing material. We've also developed a combined method that utilizes the heated cantilever probe to pattern a polymer masking layer that can serve as a template for area

selective atomic layer deposition. As a demonstration, TiO₂ was deposited on silicon surface using thermal probe nanolithography patterned polymer as the masking layer. Detailed process conditions were investigated.

The resolution of selective decomposition method is limited by the film thickness. In order to overcome this limitation, we've also developed another thermal probe nanolithography method, which is thermal probe top surface imaging. In this method, the heated AFM tip was used to generate functional groups on the polymer surface, and then ALD was used to selectively deposit TiO₂ on the surface where contains those functional groups. A new poly (hydroxyl styrene) based copolymer was developed for this method. By choosing the proper protecting group, this material has the right thermal stability for both the thermal writing and the ALD process. We've successfully demonstrated this technology. In this process, we noticed the tip can be contaminated, and the tip performance can degrade over time. So we presented a tip cleaning process to solve this problem.

We also investigated using self assembly monolayers (SAMs) as the thermal writing materials. SAMs are the ideal material for thermal writing, because less material is used, and there is no deformation problem of the substrate. These two are the major advantages of thermal writing on SAMs. We investigated two different SAMs as the writing materials. One is the aminopropyltriethoxysilane (APTES) and the other one is tetrahydropyranyl (THP) protected 3-mercaptopropyltriethoxysilane (MPTES). We demonstrated that the APTES can be patterned using thermal AFM probe, and other materials can be selectively deposited on the patterned APTES SAMs. But our main focus of patterning SAMs is on THP-MPTES. We proposed to use thermal AFM probe to

selectively generate thiol groups from THP-MPTES SAMs, and then use these thiol groups to guide the AuNPs deposition. Detailed analysis was done to prove the chemistry behind this method. AuNPs were successfully deposited on pattern THP-MPTES SAMs.

We've developed a couple of nanolithography method using thermal AFM probes. Some simulation and modeling works were also done to help us further understand these processes. FemLab was used to analyze the heat transfer in the thermal cantilever and between the heated tip and substrate. The simulated results have very good agreement with experimental data. We've also simulated the TGA curve with ultra high heating rate to understand to thermal decomposition using heated AFM tip. Base on kinetics of polymer thermal decomposition, we've built a simple model for the selective thermal decomposition nanolithography. And the experimental results can be very well fitted using this model.

9.2 Recommendations for Future Works

In this work, we've showed some amazing results about thermal probe nanolithography. Some novel lithography methods using scanning thermal probe are developed, new materials were synthesized for these methods. Also some simulation and modeling works were done to further understand these processes. But these works are just the beginning of this new technology. We believe scanning thermal probe nanolithography is a very promising new technology for nanopatterning, there are more research worth to do in this area. According our experience in this work, following recommendations for future works are listed.

9.2.1 New Polymers Por Selective Decomposition (Cyclic Carbonate)

In Chapter 3, we already showed that the cross-linked amorphous sacrificial polymers are the best material for selective thermal decomposition method. In this work, we used methacrylate as the endgroup for cross-linking. The TGA results show that this methacrylate cross-linking unit needs higher temperature than the polymer main chain to be decomposed. Because of this, some decomposition residue may remain in the thermal written area. Although these residues can be easily removed, if we can develop some new cross-linked polymer with the cross-linking unit can be easily decomposed, then the process can be simplified. Since we used polycarbonate as the main chain for the sacrificial polymer, the best cross-linking unit will also be carbonate.

We've put a lot of time and effort try to develop this kind of polymer with carbonate cross-linking unit. Following are two different synthesis routes we've tried (see Figure 9-1).

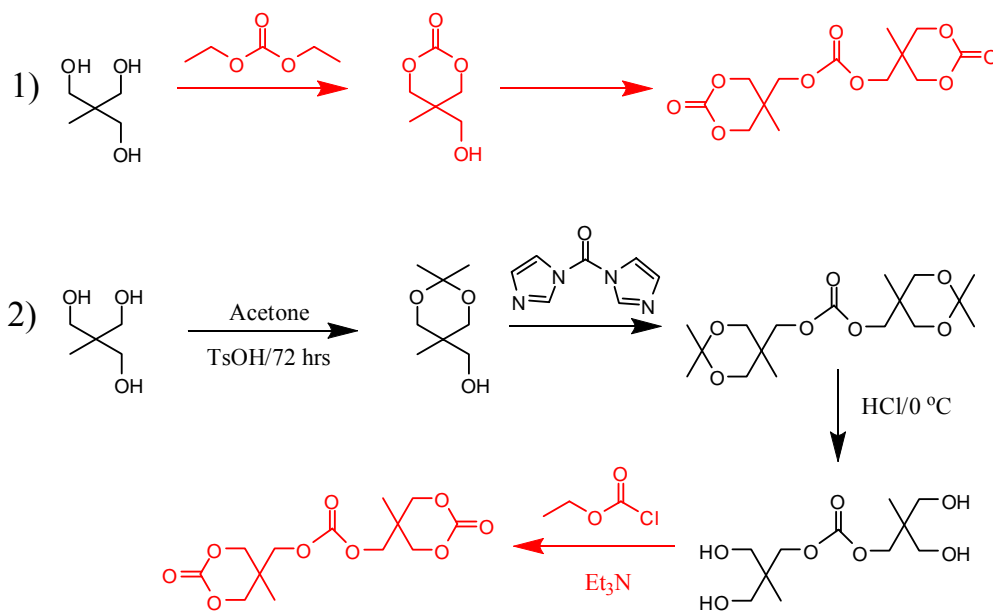


Figure 9-1. Synthetic routes for cyclic carbonate

It is well known that cyclic carbonate can be polymerized by ring-opening polymerization.[1] By putting multiple cyclic carbonate group in one molecule, we can make this molecule cross-linkable [2]. If the linkage between the cyclic carbonate groups is also made of carbonate, then the cross-linked polymer network made from this molecule will be all carbonate. To make this kind of molecule, we first tried to make a hydroxyl group functionalized cyclic carbonate, then link two of this cyclic carbonate together with a carbonate linkage. Because the selectivity is very low, and the cyclic carbonate is very unstable, we couldn't get the purified cyclic for next step. Then we tried another synthetic route. We tried to link two triols with carbonate, and then convert the triol into cyclic carbonate. It was successful to make the linked two triols, but the final step for making the cyclic carbonate still wasn't successful.

There are very few literatures about synthesis of functionalized cyclic carbonate [3], and no commercial available products for purchase. We believe synthesis of this kind of material need high professional organic synthesis skills, which is beyond our capability; it is not the main focus of this work. In spite of this, we still believe that the material we proposed is still worth to try if someone has the capability and skills for synthesis of this kind of material. Also the structure we proposed is just one example, any cross-linked polymer which can be cleanly decomposed at one decomposition step at low temperature will be desirable for this purpose.

9.2.2 Thermal Writing in SAMs For Selective ALD

In this work, we presented a novel thermal probe top surface imaging method in polymers. We obtained some good results, but also had some issue about the diffusion of the ALD precursors in the polymer film. In order to improve this process, the material for the thermal probe top surface imaging will be self assembly monolayers (SAMs). Use heated AFM probe to generate functional group R on a SAM coated surface. Then use these R groups as seed for ALD deposition of other materials.

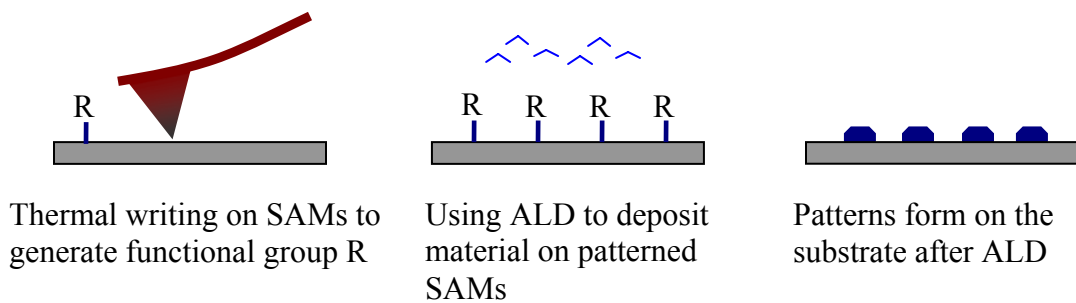


Figure 9-2. Thermal writing in SAMs for selective ALD deposition of other materials

The main advantage of using SAMs for selective ALD is there should be no precursor diffusion problem. We already show TiO_2 can be selectively deposited on surface containing hydroxyl groups. But there are a lot of materials can be deposited using ALD. Metals will be very important material for device fabrication. Deposition of metal is one of the hot topics in ALD research.[4,5] It will be very useful if we can selectively deposit metals on thermal probe patterned SAMs. But the deposition of metal is even harder than TiO_2 , and the selectivity is low. There is a lot of work need to be done in order to make this happen.

9.2.3 Direct Device Fabrication

So we have just demonstrated making simple material patterns. But we believe thermal probe lithography is a very versatile technology. It has more capabilities beyond simple patterning. We think it is possible to directly fabricate devices using thermal AFM probes.



Figure 9-3. Thermal writing in PPV polymer

Figure 9-3 shows a very simple example. Thermal AFM probe was used to thermally activate the poly (p-phenylenevinylene) (PPV) based polymer to change its light-emitting property. The thermal written pattern (“PPV”) can be seen under fluorescence microscope. This is just an example shows that beside thermal decomposition, there are a lot of physical or chemical changes of materials can be activated thermally. These physical or chemical processes may be used to directly fabricate useful devices.

9.3 References

- [1] Toshikazu Takata, Michito Icarashi, Takeshi endo, Synthesis and Cationic Ring-Opening Polymerization of a Cyclic Carbonate, 5-Methylene- 1,3-dioxan-2-one, Journal of Polymer Science: Part A Polymer Chemistry (1991) 29,781-784 (1991)
- [2] Talal F Al-Azemi, Kirpal S. Bisht, Synthesis of novel bis- and tris- (cyclic carbonate)s and their use in preparation of polymer networks, Polymer (2002) 43: 2161-2167
- [3] Karl D. Weilandt, Helmut Keul, Hartwig Hocker, Synthesis and ring-opening polymerization of 2-acetoxymethyl-2-alkyltrimethylene carbonates and of 2-methoxycarbonyl-2-methyltrimethylene carbonate; a comparison with the polymerization of 2,2-dimethyltrimethylene carbonate, Macromol. Chem. Phys. (1996) 197,3851-3868
- [4] Booyong S. Lim, Antti Bahtu, Roy G. Gordon, Atomic layer deposition of transition metals, nature materials (2003) 2 :749-754
- [5] Titta Aaltonen, Mikko Ritala, Yung-Liang Tung, Yun Chi, Kai Arstila, Kristoffer Meinander, Markku Leskela, Atomic layer deposition of noble metals: Exploration of the low limit of the deposition temperature, J. Mater. Res., 19(11), 3353-3358

APPENDIX A

MATLAB CODE FOR AFM TOPOGRAPHY DATA ANALYSIS TO CALCULATE THE INDENT VOLUME AND PILE UP VOLUME.

```
%*****AFM thermal indent analysis*****

l=10; %scan rang, um

r=512; %scan resolution, pixel

dx=1000*l/512; %pixel size, nm

da=dx^2; %pixel size, nm^2

a=textread('12-17.5-200ms.txt'); %read data file

[m,n]=size(a); %get the size of matrix a

MAX=max(a(:)); %find the max

MIN=min(a(:)); %find the min

Vp=0; %initial pileup volum is zero

Vi=0; %initial indent volum is zero

for i=1:1:m

    for j=1:1:n

        if a(i,j)>0; %calculate pileup volume,nm^3

            Vp=Vp+1e9*a(i,j)*da;

        elseif a(i,j)<0;

            Vi=Vi+1e9*a(i,j)*da; %calculate indent volume, nm^3

        end

    end

end
```

```
end
end
end
MIN
MAX
Vi
Vp
Vi2Vp=-Vi/Vp
%dlmwrite('0510071.txt',[MIN,MAX,Vi,Vp,Vi2Vp,888888],'-append')
```

APPENDIX B

MATLAB CODE FOR AUTOMATIC TGA DATA ANALYSIS TO EXTRACT THE KINETIC PARAMETER OF THERMAL DECOMPOSITION

```
%*****Automatic TGA Kinetics Data Fitting Code (Matlab)*****  
  
ns=0; % starting reaction order analysis  
  
dn=0.1; % step size of reaction order analysis  
  
ne=2; % final reaction order for analysis  
  
n=ns:dn:ne; % assign all the reaction order for analysis  
  
[j,k]=size(n); % find the total number of the reaction, and assign it to k  
  
data=xlsread('iPOCTGA2'); % read the data file, subject to change when the data file  
name is different  
  
% the first column of the data file should be temperature in C,  
  
% the 2nd column of the data file should be weight percentage, in wt%  
  
[m,l]=size(data); % find the dimension of the data matrix, and assign them to m and l  
  
TG=[]; % define a work matrix  
  
TG(:,1)=data(:,1)+273.15; % assign the temperature (units is K) to the first column of the  
working matrix
```

```

TG(:,2)=data(:,2); % assign the weight percentate to the second colum of the working
matrix

for (j=1:1:k) % loop for different reaction orders

    for i=1:1:m

        TG(i,3)=1/TG(i,1); % calculate 1/T and asign it to the third colum of the working
matrix

    end

    if n(j)<1

        for i=1:1:m

            TG(i,j+3)=TG(i,2)^(1-n(j)); % calculate the w^(1-n)

        end

        for i=2:1:(m-1)

            TG(i,j+4)=(TG(i+1,j+3)-TG(i-1,j+3))/(TG(i+1,1)-TG(i-1,1)); % calculate the
derivative, dw^(1-n)/dT, for points other than the first and last point

        end

        TG(1,j+4)=(TG(2,j+3)-TG(1,j+3))/(TG(2,1)-TG(1,1)); % calculate the
derivative, dw^(1-n)/dT, for first point

        TG(m,j+4)=(TG(m,j+3)-TG(m-1,j+3))/(TG(m,1)-TG(m-1,1)); % calculate the
derivative, dw^(1-n)/dT, for last point

    end

end

```

```

    TG(i,j+3)=log(-TG(i,j+4)); % calculate  $\ln[-dw^{(1-n)}/dT]$ , and assign it to j+3
    column, and over write the original j+3 column

    end

elseif n(j)==1

    for i=1:1:m

        TG(i,j+3)=log(TG(i,2)); % calculate the  $\ln(w)$ 

    end

    for i=2:1:(m-1)

        TG(i,j+4)=(TG(i+1,j+3)-TG(i-1,j+3))/(TG(i+1,1)-TG(i-1,1)); % calculate the
        derivative,  $d\ln(w)/dT$ , for points other than the first and last point

    end

    TG(1,j+4)=(TG(2,j+3)-TG(1,j+3))/(TG(2,1)-TG(1,1)); % calculate the
    derivative,  $d\ln(w)/dT$ , for first point

    TG(m,j+4)=(TG(m,j+3)-TG(m-1,j+3))/(TG(m,1)-TG(m-1,1)); % calculate the
    derivative,  $d\ln(w)/dT$ , for last point

    for i=1:1:m

        TG(i,j+3)=log(TG(i,j+4)); % calculate  $\ln[d\ln(w)/dT]$ , and assign it to j+3 column,
        and over write the original j+3 column

    end

else

    for i=1:1:m

```

```

    TG(i,j+3)=TG(i,2)^(1-n(j)); % calculate the  $w^{(1-n)}$ 

end

for i=2:1:(m-1)

    TG(i,j+4)=(TG(i+1,j+3)-TG(i-1,j+3))/(TG(i+1,1)-TG(i-1,1)); % calculate the
    derivertive,  $dw^{(1-n)}/dT$ , for points other than the first and last point

end

    TG(1,j+4)=(TG(2,j+3)-TG(1,j+3))/(TG(2,1)-TG(1,1)); % calculate the derivertive,
     $dw^{(1-n)}/dT$ , for first point

    TG(m,j+4)=(TG(m,j+3)-TG(m-1,j+3))/(TG(m,1)-TG(m-1,1)); % calculate the
    derivertive,  $dw^{(1-n)}/dT$ , for last point

for i=1:1:m

    TG(i,j+3)=log(TG(i,j+4)); % calculate  $\ln[dw^{(1-n)}/dT]$ , and assign it to j+3 colum,
    and over write the original j+3 colum

end

end

figure

xlabel('1/T, 1/K');

ylabel('ln[ $dw^{(1-n)}/dT$ ] or ln[ $d\ln w/dT$ ]');

hold on;

for (i=1:1:k)

```

```
if n(i)<1
    plot(TG(:,3),TG(:,i+3),'g','LineWidth',i/5+0.5);
elseif n(i)==1
    plot(TG(:,3),TG(:,i+3),'b','LineWidth',i/5);
else
    plot(TG(:,3),TG(:,i+3),'r','LineWidth',i/5-1.5);
end
end
hold off;
```

APPENDIX C

MATLAB CODE FOR TGA SIMULATION WITH SINGLE STEP DECOMPOSITION

```
%TGA Kinetics
Ea=251000; % Ea is activation energy, J/mol
e=49.2; % e=lnk, k is pre-exponential factor of Arrhenius equation
c=3e7; % c is heating rate, K/min
R=8.314; % R is gas constant, J/(mol.K)
a=Ea/R;
b=e-log(c/60);
T=[]; % temperature, K
dlnw=[]; % dw/dT
lnw=[];
w=[]; % w is the remain weight
wp=[]; % weight percentage
T0=300; % starting temperature, K
Te=1000; % Final temperature, K
dT=0.1; % Temperature increatment, K
n=round((Te-T0)/dT); % Total cycle number
TG=[]; % TGA plot data
for i=1:1:n
```

```

T(i)=T0+i*dT;

dlnw(i)=-exp(b-a/T(i));

end

for i=2:1:n

    lnw(i)=(dlnw(i-1)+dlnw(i))/2;

end

for i=2:1:n

    lnw(i)=lnw(i)+lnw(i-1);

    w(i)=exp(lnw(i));

end

w0=w(2);

for i=2:1:n

    wp(i)=100*w(i)/w(2); % calculate weight percentage

    TG(i-1,1)=T(i)-273; % put temperature values [C] in first column of TG data

    TG(i-1,2)=wp(i); % put weight percentage values in second column of TG data

end

TG(1,3)=c; % put heating rate [K/min] in data file

TG(2,3)=Ea; % put activation energy [KJ/mol] in data file

TG(3,3)=e; % put pre-factor lnK in data file

save TGA TG -ASCII -DOUBLE -TABS

plot(TG(:,1),TG(:,2),'LineWidth',2)

ylim([-5 105])

xlabel('Temperature, C')

```

```
ylabel('Weight, %')
```

APPENDIX D

MATLAB CODE FOR TGA SIMULATION WITH TWO-STEP DECOMPOSITION

%TGA Kinetics

c=5; % c is heating rate, K/min

x=0.4; % weight percentage of protecting group in whole polymer

r=0.075; % weight percentage of residue

Ea1=173579; % Ea is activation energy of protecting group, J/mol

e1=32.5; % e=lnk, k is pre-exponential factor of Arrhenius equation

Ea2=167000; % Ea is activation energy of backbone J/mol

e2=25.7; % e=lnk, k is pre-exponential factor of Arrhenius equation

R=8.314; % R is gas constant, J/(mol.K)

a1=Ea1/R;

b1=e1-log(c/60);

a2=Ea2/R;

b2=e2-log(c/60);

T=[]; % temperature, K

dlnw1=[]; % dw/dT

lnw1=[];

w1=[]; % w is the remain weight

wp1=[]; % weight percentage

```

dlnw2=[]; % dw/dT

lnw2=[];

w2=[]; % w is the remain weight

wp2=[]; % weight percentage

T0=300; % starting temperature, K

Te=1300; % Final temperature, K

dT=0.1; % Temperature increatment, K

n=round((Te-T0)/dT); % Total cycle number

TG=[]; % TGA plot data

for i=1:1:n

    T(i)=T0+i*dT;

    dlnw1(i)=-exp(b1-a1/T(i));

    dlnw2(i)=-exp(b2-a2/T(i));

end

for i=2:1:n

    lnw1(i)=dT*(dlnw1(i-1)+dlnw1(i))/2;

    lnw2(i)=dT*(dlnw2(i-1)+dlnw2(i))/2;

end

for i=2:1:n

    lnw1(i)=lnw1(i)+lnw1(i-1);

    w1(i)=exp(lnw1(i));

    lnw2(i)=lnw2(i)+lnw2(i-1);

    w2(i)=exp(lnw2(i));

```

```

end

for i=2:1:n

    wp1(i)=100*w1(i)/w1(2); % calculate weight percentage
    wp2(i)=100*w2(i)/w2(2); % calculate weight percentage

    TG(i-1,1)=T(i)-273; % put temperature values [C] in first colum of TG data
    TG(i-1,2)=wp1(i); % put weight percentage values in second colum of TG data
    TG(i-1,3)=wp2(i); % put weight percentage values in second colum of TG data
    TG(i-1,4)=x*wp1(i)+(1-x-r)*wp2(i)+100*r;

end

TG(1,5)=c; % put heating rate [K/min] in data file
TG(2,5)=Ea1; % put activation energy [KJ/mol] in data file
TG(3,5)=e1; % put pre-factor lnK in data file
TG(4,5)=Ea2; % put activation energy [KJ/mol] in data file
TG(5,5)=e2; % put pre-factor lnK in data file

save TGA2 TG -ASCII -DOUBLE -TABS

plot(TG(:,1),TG(:,4),'LineWidth',2)

ylim([-5 105])

xlabel('Temperature, C')

ylabel('Weight, %')

```